Technical Report Series on Global Modeling and Data Assimilation, Volume 45

Randal D. Koster, Editor

The MERRA-2 Aerosol Assimilation

C. A. Randles, A. M. da Silva, V. Buchard, A. Darmenov, P. R. Colarco, V. Aquila, H. Bian, E. P. Nowottnick, X. Pan, A. Smirnov, H. Yu, and R. Govindaraju

National Aeronautics and
Space Administration

Goddard Space Flight Center
Greenbelt, Maryland 20771

December 2016

NASA STI Program ... in Profile

Since its founding, NASA has been dedicated to the advancement of aeronautics and space science. The NASA scientific and technical information (STI) program plays a key part in helping NASA maintain this important role.

The NASA STI program operates under the auspices of the Agency Chief Information Officer. It collects, organizes, provides for archiving, and disseminates NASA's STI. The NASA STI program provides access to the NASA Aeronautics and Space Database and its public interface, the NASA Technical Report Server, thus providing one of the largest collections of aeronautical and space science STI in the world. Results are published in both non-NASA channels and by NASA in the NASA STI Report Series, which includes the following report types:

- TECHNICAL PUBLICATION. Reports of completed research or a major significant phase of research that present the results of NASA Programs and include extensive data or theoretical analysis. Includes compilations of significant scientific and technical data and information deemed to be of continuing reference value. NASA counterpart of peer-reviewed formal professional papers but has less stringent limitations on manuscript length and extent of graphic presentations.

- TECHNICAL MEMORANDUM. Scientific and technical findings that are preliminary or of specialized interest, e.g., quick release reports, working papers, and bibliographies that contain minimal annotation. Does not contain extensive analysis.

- CONTRACTOR REPORT. Scientific and technical findings by NASA-sponsored contractors and grantees.

- CONFERENCE PUBLICATION. Collected papers from scientific and technical conferences, symposia, seminars, or other meetings sponsored or co-sponsored by NASA.

- SPECIAL PUBLICATION. Scientific, technical, or historical information from NASA programs, projects, and missions, often concerned with subjects having substantial public interest.

- TECHNICAL TRANSLATION. English-language translations of foreign scientific and technical material pertinent to NASA's mission.

Specialized services also include organizing and publishing research results, distributing specialized research announcements and feeds, providing help desk and personal search support, and enabling data exchange services. For more information about the NASA STI program, see the following:

- Access the NASA STI program home page at http://www.sti.nasa.gov

- E-mail your question via the Internet to help@sti.nasa.gov

- Fax your question to the NASA STI Help Desk at 443-757-5803

- Phone the NASA STI Help Desk at 443-757-5802

- Write to:

  NASA STI Help Desk
  NASA Center for AeroSpace Information
  7115 Standard Drive
  Hanover, MD 21076-1320

Technical Report Series on Global Modeling and Data Assimilation, Volume 45

Randal D. Koster, Editor

The MERRA-2 Aerosol Assimilation

Cynthia A. Randles
GESTAR/Morgan State University

Arlindo M. da Silva
NASA Goddard Space Flight Center

Virginie Buchard
GESTAR/Universities Space Research Association

Anton Darmenov
NASA Goddard Space Flight Center

Peter R. Colarco
NASA Goddard Space Flight Center

Valentina Aquila
GESTAR/Johns Hopkins University

Huisheng Bian
University of Maryland, Baltimore County

Edward P. Nowottnick
GESTAR/Universities Space Research Association
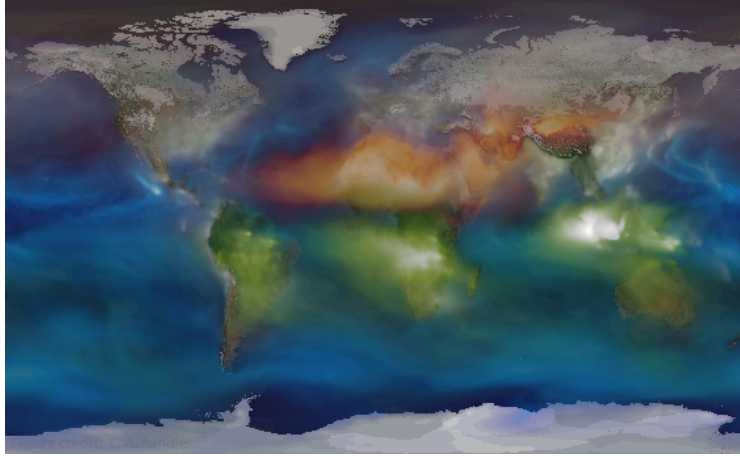
Xiaohua Pan
University of Maryland, College Park

Alexander Smirnov
Science Systems and Applications, Inc.

Hongbin Yu
University of Maryland, College Park

Ravi Govindaraju
Science Systems and Applications, Inc.

December   **2016**

MERRA-2 AOD in September, 1997 during a strong El Niño that exacerbated fires in Indonesia. Colors represent AOD from various aerosol types: dust (orange), carbonaceous (green), sulfate (white), and sea salt (blue).

The MERRA-2 Aerosol Assimilation

C. A. Randles[1,2,3], A. M. da Silva[1,2], V. Buchard[1,2,4], A. Darmenov[1,2], P. R. Colarco[1,5], V. Aquila[1,5,6], H. Bian[1,5,7], E. P. Nowottnick[1,4,5], X. Pan[1,5,8], A. Smirnov[1,9], H. Yu[1,8,10], and R. Govindaraju[1,2,11]

[1]NASA Goddard Space Flight Center (GSFC)
[2]NASA Global Modeling and Assimilation Office (GMAO)
[3]GESTAR/Morgan State University
[4]GESTAR/USRA
[5]NASA Atmospheric Chemistry and Dynamics Lab
[6]GESTAR/Johns Hopkins University
[7]University of Maryland, Baltimore County
[8]University of Maryland, College Park
[9]NASA Biospheric Sciences Laboratory
[10]NASA Climate and Radiation Laboratory
[11]SSAI

March 15, 2017

Abstract

The Modern-Era Retrospective analysis for Research and Applications, Version 2 (MERRA-2) was undertaken by NASA's Global Modeling and Assimilation Office (GMAO) with two primary objectives: to place observations from NASA's Earth Observing System (EOS) satellites into a climate context and to update the Modern-Era Retrospective analysis for Research and Applications (MERRA) system to include the most recent satellite data. Many advancements have been incorporated into MERRA-2, which focuses on the satellite era (1980 – present). Notably, MERRA-2 now includes an online implementation of the Goddard Chemistry, Aerosol, Radiation, and Transport model (GOCART) integrated into the Goddard Earth Observing System Model, Version 5 (GEOS-5) modeling system. GOCART simulates organic carbon, black carbon, sea salt, dust, and sulfate aerosols as well as sulfate aerosol precursors (dimethyl sulfide, sulfur dioxide), carbon monoxide and carbon dioxide. While the original MERRA assimilated only meteorological parameters (winds, temperature, humidity, etc.), using the Goddard Aerosol Assimilation System (GAAS) we now extend MERRA-2 to include assimilation of bias-corrected aerosol optical depth (AOD) from AVHRR and MODIS, MISR AOD over bright surfaces, and AERONET AOD. Details of the evaluation of MERRA-2 aerosols, major findings and recommendations to users of the MERRA-2 aerosol products are documented in this text.

Contents

List of Figures

List of Tables

Chapter 1

Introduction

The Modern-Era Retrospective analysis for Research and Applications, Version 2 is a NASA atmospheric reanalysis for the modern satellite era (1980 - onward) that uses the Goddard Earth Observing System Model, Version 5 atmospheric data assimilation system (ADAS), version 5.12.4. MERRA-2 is a follow-on to the original MERRA project, which was produced by the Global Modeling and Assimilation Office (GMAO) using a 2005 version of the GEOS ADAS. One of the primary motivations for MERRA-2 is that the original MERRA system, described in Rienecker et al. (2008) and Rienecker et al. (2011), required updating to incorporate observations from new satellites launched after NOAA-18 (*i.e.* NOAA-19, Metop-A, Metop-B, and Suomi NPP). In addition to heritage and follow-on instruments, MERRA-2 also incorporates atmospheric measurements from new data sources such as GPS radio occultation and the NASA Aura satellite. Advances in the GEOS-5 system since MERRA have resulted in many additional features to the MERRA-2 system. Compared to MERRA, the MERRA-2 system has reduced spurious trends and jumps related to changes in the observing system, and biases and imbalances in the water cycle are reduced (Reichle and Liu, 2014; Takacs et al., 2015). This reanalysis is viewed as an intermediate product between the original MERRA and a next-generation reanalysis that will couple the land, ocean, and atmosphere. Molod et al. (2012) and Molod et al. (2014) detail the differences between the original MERRA system and MERRA-2. Additional MERRA-2 technical memoranda include further details on the meteorological assimilation and observing system (McCarty, 2016) and the MERRA-2 climatology, including the improved representation of the stratosphere, ozone, and cryospheric processes (Bosilovich et al., 2016).

In a significant step towards an Integrated Earth System Analysis (IESA), MERRA-2 now includes fully modeled and analyzed aerosol fields, with radiative effects that feed back to the atmospheric fields. Previously, GMAO had performed an off-line aerosol reanalysis, known as MERRAero, in which bias-corrected MODIS aerosol optical depth (AOD) from Terra and Aqua was assimilated into the GEOS-5 model driven by meteorology from MERRA for the period 2002 to present (Buchard et al., 2015). Now, for MERRA-2, the aerosol and meteorological assimilations are performed concurrently. Additionally, MERRA-2 incorporates AOD measurements from various NOAA Polar Operational Environmental Satellites (POES), NASA Earth Observing System (EOS) platforms, and NASA ground-based observations. This document provides a description and assessment of the aerosol assimilation in the MERRA-2 system.

The assimilation system uses a cubed-sphere grid of approximately a half-degree resolution. The aerosol assimilation is performed at eight synoptic times a day (0, 3, 6, 9, 12, 15, 18, and 21Z), and output data is interpolated onto a regular grid with resolution $0.625°$ longitude $\times$ $0.5°$ latitude. Archived data streams include three-dimensional profiles of aerosol mass mixing ratio output for synoptic times on the native 72 eta-coordinate levels, and two-dimensional surface-level or column-integrated aerosol diagnostics (e.g. wet deposition rate, surface mass concentration) and properties (e.g. AOD) output hourly or every three hours. Two-dimensional gridded files are also available as monthly and diurnal average files. The MERRA-2 data is available online through the Goddard Earth Sciences (GES) Data and Information Services Center (DISC) (http://disc.sci.gsfc.nasa.gov/mdisc/). Documentation of the data access procedures, file specifications, and related publications can be found at http://gmao.gsfc.nasa.gov/reanalysis/MERRA-2/.

Chapter 2

Aerosol model and emissions

This section describes the online GOCART aerosol module (Section 2.1), aerosol emissions (Section 2.2), and aerosol optical properties (Section 2.3) used in MERRA-2. More information about the GEOS-5 ADAS system used for MERRA-2 can be found in Bosilovich et al. (2016) and McCarty (2016). MERRA-2 related peer-reviewed publications can be found at `http://gmao.gsfc.nasa.gov/reanalysis/MERRA-2/pubs/`.

2.1   GOCART aerosol module

Aerosols in MERRA-2 are simulated with an online version of the the Goddard Chemistry, Aerosol, Radiation, and Transport model (GOCART, Chin et al., 2002; Colarco et al., 2010) and are radiatively active. GOCART treats the sources, sinks, and chemistry of dust, sulfate (SO_4), sea salt, and black (BC) and organic carbon (OC) aerosols. Aerosol species are assumed to be externally mixed. Total mass of sulfate and hydrophobic and hydrophilic modes of carbonaceous aerosols are tracked. For dust and sea salt, the particle size distribution is explicitly resolved across five non-interacting size bins each (Colarco et al., 2010). Both dust and sea salt have wind-speed dependent emissions. Primary sulfate (SO_4) and carbonaceous aerosol species have emissions principally from fossil fuel combustion, biomass burning, and biofuel consumption, with additional biogenic sources of particulate organic matter. Secondary sources of sulfate include chemical oxidation of SO_2 and Di-Methyl Sulfide (DMS), and we include a database of volcanic SO_2 emissions and injection heights. Note that we report organic mass as Particulate Organic Matter (POM) where POM = $1.4 \times$ OC as

Table 2.1: Aerosol and precursor emissions in MERRA-2

Aerosol Type	Source	Temporal Resolution	Spatial Resolution[a,b]
Dust	Wind-driven emissions w/Ginoux et al. (2001) static topographic depression map	Model	$0.3125° \times 0.25°$[c]
Sea Salt	Wind-driven emissions	Model	Model
Volcanic (SO_2)	AeroCom Phase II (HCA0 v2; Diehl et al., 2012)	Daily degassing (1980 – onwards) and daily eruptive (1980 – 2010)	Point-sources
Biogenic terpene	Guenther et al. (1995)	Monthly-mean climatology	$2° \times 2.5°$
Di-Methyl Sulfide (DMS)	Lana et al. (2011)	Monthly-mean climatology	$1° \times 1°$
Biomass Burning (SO_2, SO_4, POM, and BC)	scaled RETROv2 (Duncan et al., 2003) scaled GFEDv3.1 (Randerson et al., 2006) QFED 2.4-r6 (Darmenov and da Silva, 2015)	Monthly-varying (1980 – 1996) Monthly-varying (1997 – 2010) Daily-varying (2010 – onwards)	$0.3125° \times 0.25°$ $0.3125° \times 0.25°$ $0.3125° \times 0.25°$
Anthropogenic SO_2	EDGARv4.2 (Energy + Non-Energy) (European Comission, 2011)	Annually-varying (1980 – 2008)	$0.1° \times 0.1°$
Anthropogenic SO_4, POM, and BC	AeroCom Phase II (HCA0 v1; Diehl et al., 2012)	Annually-varying (1980 – 2006)	$1° \times 1°$
International Ships SO_2	EDGARv4.1 (European Commission, 2010)	Annually-varying (1980 – 2005)	$1° \times 1°$
International Ships SO_4, POM, and BC	AeroCom Phase II (HCA0 v1; Diehl et al., 2012)	Annually-varying (1980 – 2007)	$1° \times 1°$
Aircraft SO_2	AeroCom Phase II (HCA0 v1; Diehl et al., 2012)	Monthly-varying (1980 – 2006)	$1° \times 1.25° \times$ 72-levels

[a] Model = MERRA-2 time-step of 30 minutes with spatial resolution of $0.5°$ latitude $\times$ $0.625°$ longitude.

[b] latitude $\times$ longitude

[c] Resolution is for source map (Ginoux et al., 2001); wind-driven emissions at model time-step and grid.

in Textor et al. (2006), but optical properties are reported for OC. Loss processes for all aerosols include dry deposition, wet removal, and convective scavenging. Aerosol hygroscopic growth is considered in computations of particle fall velocity, deposition velocity, and optical parameters.

Further details on the implementation of GOCART in the GEOS-5 model can be found in Colarco et al. (2010). A major function of the GEOS-5/GOCART system is to perform Observing System Simulation Experiments OSSEs (Buchard et al., 2015; Colarco et al., 2014a; Nowottnick et al., 2015). This system has been used for forecast and post-mission field support for numerous National Aeronautics and Space Administration (NASA) field campaigns such as TC4, ARCTAS, DISCOVER-AQ, and SEAC⁴RS (e.g. Bian et al., 2013; Buchard et al., 2014; Nowottnick et al., 2011; Randles et al., 2016). It has also been used to investigate aerosol-climate interactions (Randles et al., 2013), interactions between aerosols and the Indian monsoon (Kishcha et al., 2014; Pan et al., 2015), feedbacks due to Saharan dust heating (Colarco et al., 2014b), aerosol impacts on tropical cyclones (Reale et al., 2014), and the aerosol impact on snow albedo (Yasunari et al., 2014). Additionally, stratospheric aerosol perturbations and their chemical, radiative, and dynamical impacts in GEOS-5 have been studied in the context of volcanic eruptions (Aquila et al., 2014), geo-engineering (Pitari et al., 2014), and meteor inputs (Gorkavyi et al., 2013).
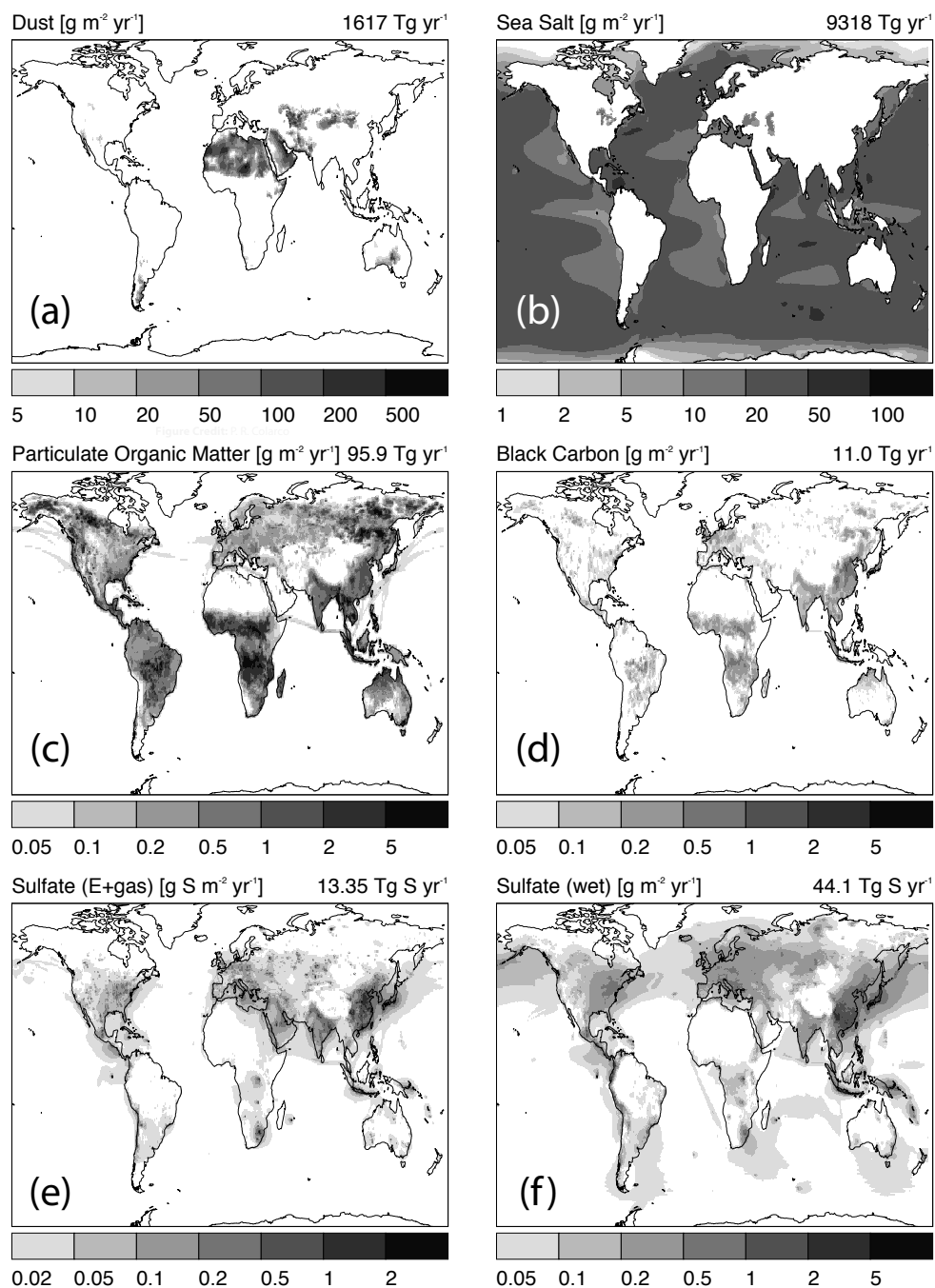
Figure 2.1: Annual average aerosol emissions over the period 2000-2014 from MERRA-2. Emissions are shown for (a) dust, (b) sea salt, (c) POM, (d) black carbon (BC), (e) primary sulfate (SO_4) and sulfate from oxidation of gaseous sulfur dioxide (SO_2), and (f) SO_4 from aqueous production. Note: POM = Particulate Organic Matter = $1.4 \times$ OC as in Textor et al. (2006). Carbonaceous, SO_2, and SO_4 emissions are from all sectors (fossil fuel, biofuel, biomass burning, and biogenic if applicable). The global mean climatological annual emission is given in the top right of each panel.
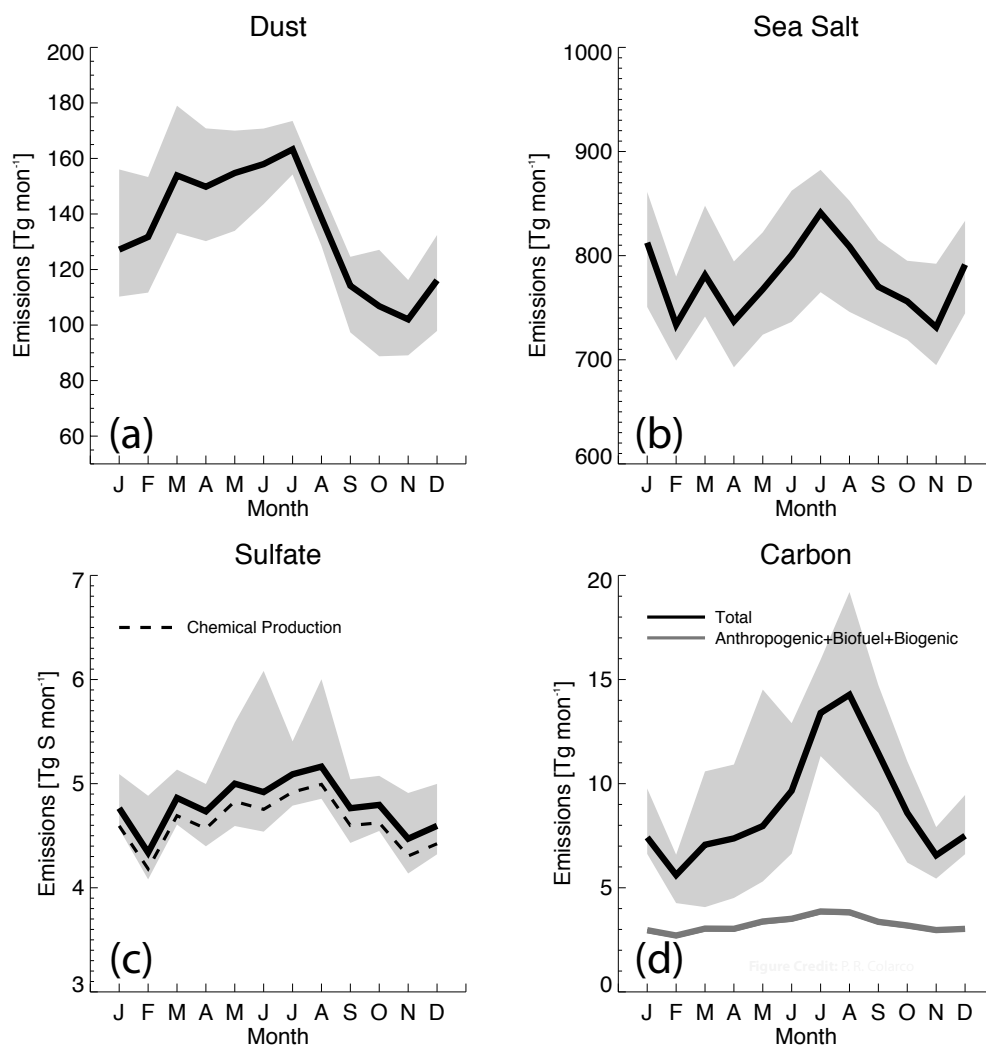
Figure 2.2: Seasonal cycle of aerosol emissions over the period 2000-2014 from MERRA-2 (solid black lines). Shading is the minimum and maximum emission over the period considered. Emissions are shown for (a) dust, (b) sea salt, (c) sulfate (SO_4) and (d) carbonaceous (BC + POM). For sulfate, the dashed line in (c) indicates the contribution from chemical production of SO_4 aerosols (oxidation of SO_2 and aqueous production); the difference between the solid and dotted line is due to primary emissions of SO_4 particles. For carbonaceous aerosols in (d), the contribution from all anthropogenic, biofuel, and biogenic sources is indicated by the grey line, and the black line includes these sources plus biomass burning emissions.

2.2 Emissions

Table 2.1 summarizes the emissions for different aerosol types used by the GOCART aerosol module in MERRA-2. Annually- and monthly-varying emissions are temporally interpolated using linear interpolation, and emissions datasets are conservatively re-gridded to the native model grid. Figure 2.1 shows the spatial distribution of aerosol emissions averaged over the period 2000-2014, and Figure 2.2 shows the seasonal cycle of globally averaged aerosol emissions over the same period. With the exception of sea salt, the global, annual mean emissions of all aerosol types are similar to the multi-model AeroCom Phase I median emissions (Textor et al., 2006). Sea salt emissions are similar to those reported in Colarco et al. (2010).

2.2.1 Natural emissions

With the exception of volcanic sulfur dioxide, natural aerosols (dust and sea salt) are emitted in the lowest model layer. SO_2 emissions from volcanic eruptions are emitted in the upper third of the database-provided volcanic plume height (the difference between the volcano altitude and specified volcanic cloud top altitude; Diehl et al., 2012). Outgassing volcanoes emit at the altitude of the volcano.

Dust. Dust emissions use a map of potential dust source locations based on the observed correlation of dust emitting regions with large-scale topographic depressions (Fig. 2.1a; Ginoux et al., 2001). In MERRA-2 the topographic map is updated and provided at 0.25° spatial resolution (P. Ginoux, personal communication). For each of the five dust size bins, dust emissions depend on the wind speed formulation of Marticorena and Bergametti (1995, their Eq. 6), and the threshold wind-speed for emission also depends on soil moisture. Additional details on dust and sea salt emissions are found in Colarco et al. (2014b). Global dust emissions peak during boreal summer due to Saharan emissions (Fig. 2.2a), with a secondary peak in boreal spring primarily from Asian emissions (e.g. Taklamakan and Gobi deserts).

Sea Salt The parameterization of sea salt aerosol production follows the formulation of size dependent number flux in Gong (2003) but with a wind dependent term equal to $u_*^{2.41}$, where u_* is the friction velocity. Similar to the work of Jaeglé et al. (2011), we apply an independently derived SST correction term which modulates the strength of the emissions. Global average sea

salt emissions are comparable to Colarco et al. (2014b) (Fig. 2.1b); however, emissions in the "Roaring Forties" of the Southern Hemisphere and in the storm tracks of the Northern Hemisphere are reduced. Sea salt emissions show a slight peak in austral winter (Fig. 2.2b).

Volcanic Emissions   Volcanic emissions of SO_2 were compiled for the AEROsol COMparisons between Observations and Models (AeroCom) Phase II project (Diehl et al., 2012) and cover eruptive and degassing volcanos on all days from January 1, 1979 to December 31, 2010 (Fig. 2.3a). Volcanoes included are listed in the Global Volcanism Program's database provided by the Smithsonian Institution (Fig. 2.3d). Subglacial and submarine volcanoes are excluded. Degassing volcanoes from 2010 are repeated in later years but no eruptive volcanoes are included in MERRA-2 after 2010. As noted previously, the database provides volcano elevation and the estimated cloud-top height of the eruption, the difference of which gives the estimated plume height. Eruptive volcanoes emit in the upper third of the column defined by the volcano elevation and the cloud-top height; outgassing volcanoes emit at the volcano elevation. Figure 2.3a shows the global average volcanic SO_2 emissions; major volcanic eruptions (e.g. Pinatubo, El Chichón) are apparent.

Biogenic Emissions   Emissions of terpene from vegetation are oxidized to produce organic carbon particles. In GOCART, this is treated simply following Chin et al. (2002), and a monthly-mean varying climatology of terpene emissions is used (Fig. 2.3b, Guenther et al., 1995). The spatial distribution of terpene emissions is shown in Figure 2.3c. Di-Methyl Sulfide (DMS) emissions from marine algae are based on the monthly varying climatology described in Lana et al. (2011). DMS oxidizes to produce both SO_2 and methane sulfonic acid (MSA). Figures 2.3b and 2.3e show the seasonal cycle and spatial distribution of MSA and SO_2 produced from DMS emissions in MERRA-2.

2.2.2   Biomass burning emissions

Importantly, the time-frequency of biomass burning emissions differed between different periods of MERRA-2. Between 1980 and 2009 emissions were monthly-mean varying, and daily-mean emissions were used after 2010. Owing to the intense vertical mixing associated with fires, we distribute biomass burning emissions uniformly throughout the Planetary Boundary Layer (PBL) in the grid box where the fire emission occurs. A diurnal cycle is imposed online on the daily mean emission values that is more prominent in the tropics and gradually weakens in the higher

8
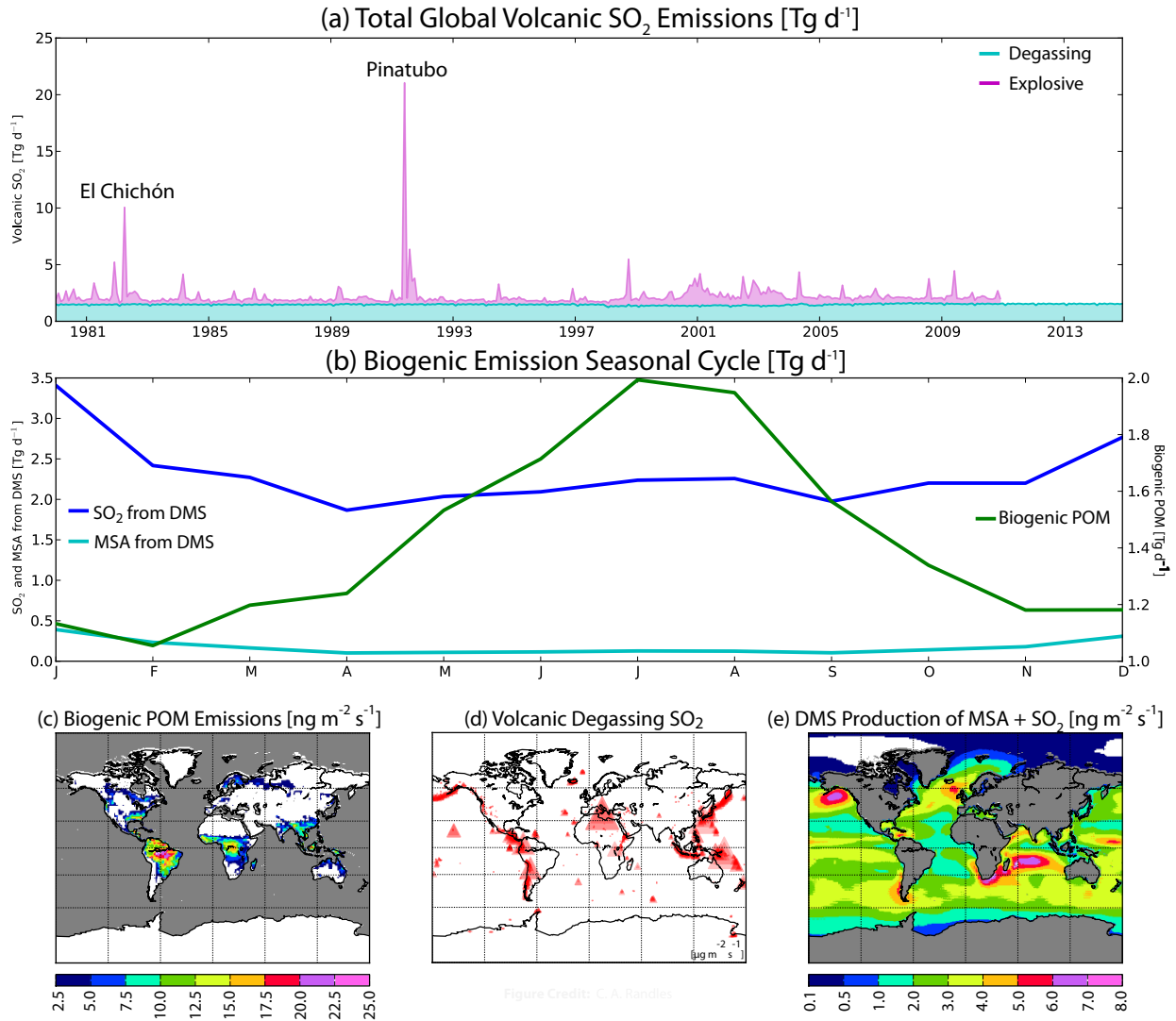
Figure 2.3: Volcanic and biogenic emissions in MERRA-2. (a) Timeseries of degassing and eruptive volcanic SO_2 emissions from Diehl et al. (2012). (b) Repeating seasonal cycle of global average emissions of biogenic POM over land and production of SO_2 and MSA from DMS emissions over the ocean. (c) Annual-mean spatial distribution of biogenic POM emissions. (d) Location and relative magnitude of SO_2 emissions from degassing volcanos (Diehl et al., 2012). (e) Annual-mean spatial distribution of SO_2 and MSA production from oxidation of DMS.

Figure 2.4: Climatology of biomass burning carbonaceous aerosol (POM + BC) emissions in $[\mu g\ m^{-2}\ s^{-1}]$ for June-July-August (left) and December-January-February (right) for the period 1980-2014. Global emissions are highest during JJA and are c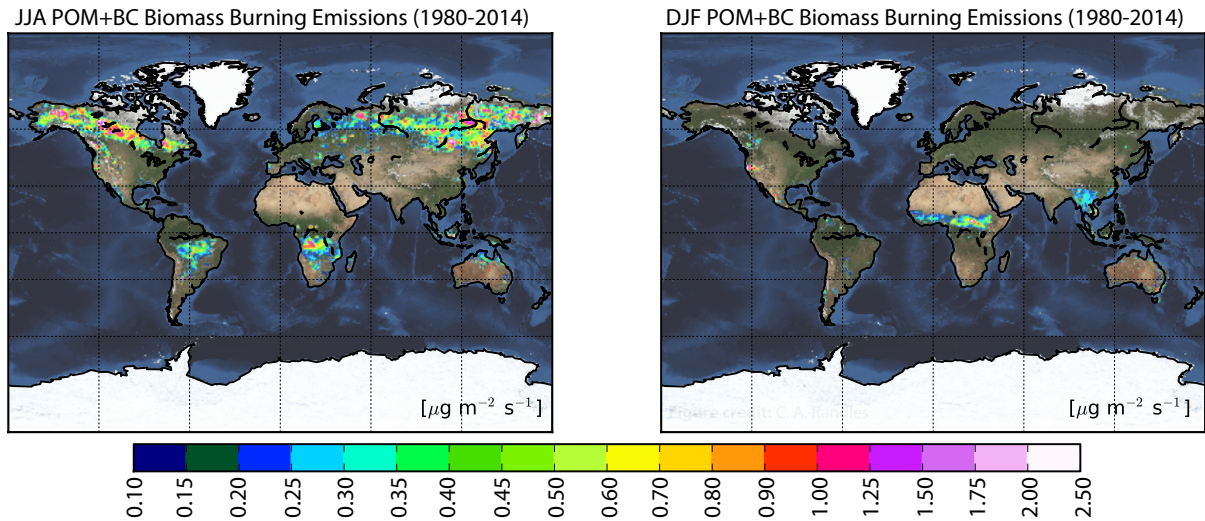oncentrated in boreal forests, the southern African savannah, and the Amazon Basin. In DJF, emissions are prominent over the Sahel and southeast Asia.

latitude extratropical temperate zones. Figure 2.4 shows the climatological seasonal mean spatial distribution of carbonaceous biomass burning aerosol emissions in MERRA-2, and the global mean and regional time series of emissions are shown in Figure 2.5. Spatial and temporal patterns of biomass burning SO_2, CO and CO_2 emissions are similar to the patterns of the carbonaceous aerosol emissions and are not shown here. Below we provide additional details on the biomass burning emissions databases used in MERRA-2.

QFED (Y2010 - onward): After 2010, daily emissions of carbonaceous aerosol (POM and BC), sulfur dioxide (SO_2), carbon monoxide (CO) and carbon dioxide (CO_2) from biomass burning are obtained from the Quick Fire Emissions Dataset (QFED) version 2.4-r6 (Darmenov and da Silva, 2015). QFED is based on the top-down Fire Radiative Power (FRP) approach and draws on the cloud correction method used in the Global Fire Assimilation System (GFAS, Kaiser et al., 2012), but in addition it employs a more sophisticated treatment of emissions from non-observed land areas (Darmenov and da Silva, 2015). FRP and locations of fires are obtained from the MODerate Resolution Imaging Spectroradiometer (MODIS) Level 2 fire products and the MODIS Geolocation products. Data from the Level 2 fire products are gridded at $0.3125° \times 0.25°$ longitude by latitude horizontal resolution and combined to create daily mean emissions at the same resolution.
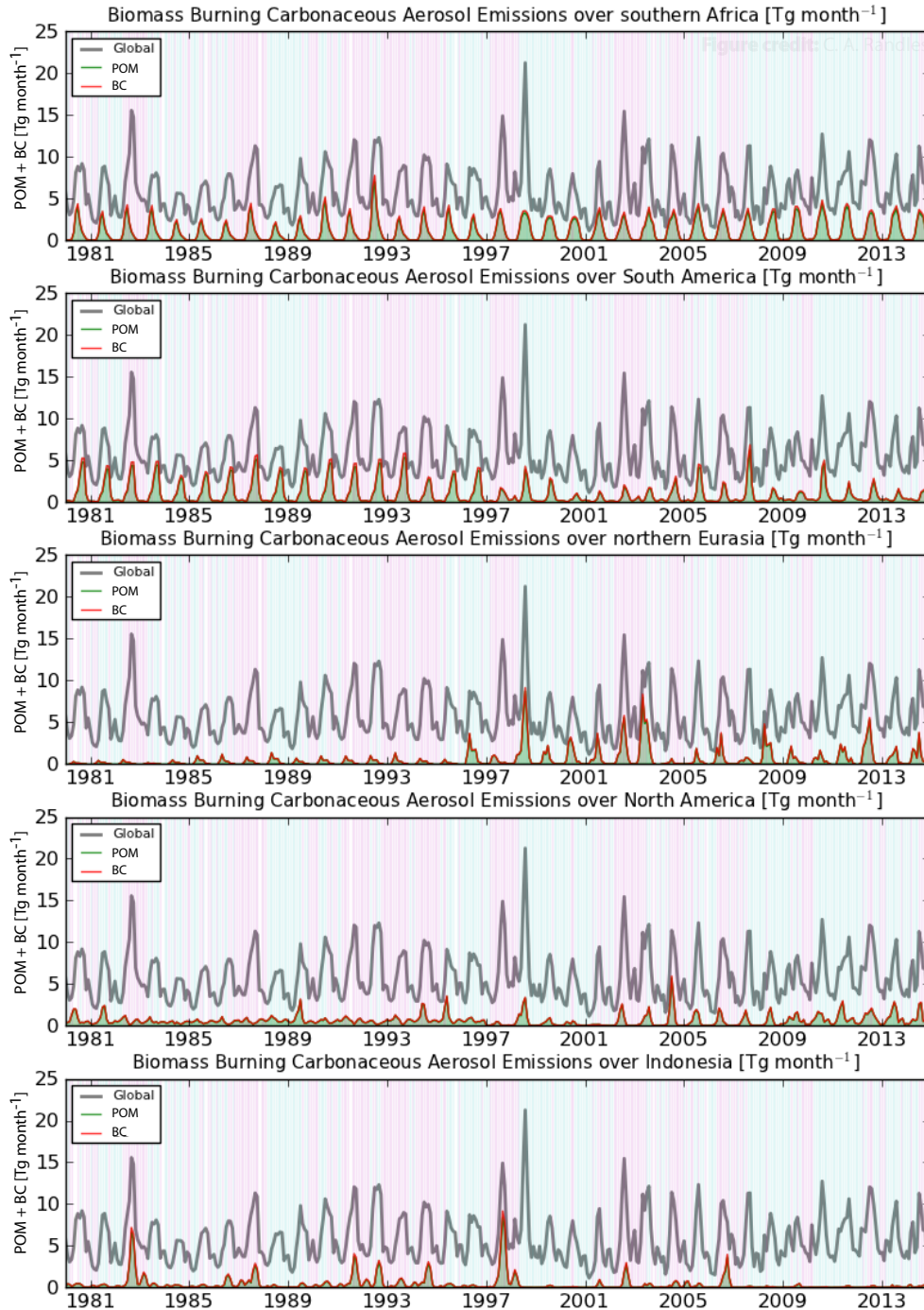
Figure 2.5: Timeseries of carbonaceous aerosol emissions (BC + POM) in Tg month^{-1} from biomass burning sources averaged globally (grey line; same in all panels) and over several major source regions (panels). For the regional emissions, red and green shading indicates the relative contribution of POM and BC to the total carbonaceous aerosol emissions. Blue (pink) shading indicates when the Southern Oscillation Index (SOI) is positive (negative) corresponding to La Niña (El Niño) episodes. SOI is from the NOAA Climate Prediction Center (CPC; http://www.cpc.ncep.noaa.gov).

HFED (Y1980-Y2009): For the period 1980 to 2009, we have compiled an historical, homogenized emissions database (HFED) of monthly mean biomass burning emissions of POM, BC, and sulfur dioxide (SO_2). For the period 1980 to 1996, HFED relies on the RETROv2 emissions from Duncan et al. (2003), which used fire data from AVHRR and ATSR and the Aerosol Index (AI) from the TOMS instrument to estimate the dry mass burned in eight global regions. Between 1997 and 2009, HFED emissions utilize the Global Fire Emissions Database, Version 3.1 (GFED) (Randerson et al., 2006; van der Werf et al., 2006). GFED was compiled using satellite data and the Carnegie-Ames-Stanford Approach (CASA) biogeochemical model. For continuity between the MERRA-2 streams, we bias-corrected the underlying HFED data sources (RETROv2 and GFED), with respect to the Quick Fire Emissions Dataset (QFED). The correction was done using GFEDv3.1 and QFEDv2.4-r6 (Darmenov and da Silva, 2015) for the period 2003-2011. First, we computed monthly, spatially varying fractional contributions of emissions from the tropical forest, extra-tropical forest, savannah and grassland biomes using the QFED climatology. These fractional contributions were then used to stratify the monthly GFED emissions by biome. Next, for each biome, the estimated GFED emissions were used to determine a scaling factor by means of a linear regression between the globally integrated QFED and GFED emissions. The final product, the corrected GFED emissions, was computed as the sum over the biomes of the scaled GFED biome-stratified emissions. Due to the similarities between emissions from RETROv2 and GFEDv3.1, the aforementioned biome-specific scaling factors were applied to RETROv2 in order to correct it in a similar manner.

2.2.3 Anthropogenic emissions

With the exception of aircraft and energy-sector sulfur dioxide, anthropogenic aerosol sources emit into the lowest model layer. Additional details of the anthropogenic emissions are described below. Figure 2.6 shows the time series of anthropogenic aerosol emissions used in MERRA-2 with contributions from the different sectors described below.

Energy and Non-Energy Sulfur: Anthropogenic emissions of SO_2 derive from the Emissions Database for Global Atmospheric Research (EDGAR), version 4.2 database that covers the period 1970 - 2008 (European Comission, 2011). After this period, we repeat 2008 emissions. Energy-sector and non-energy sector emissions of SO_2 are included, with power-plant emissions emitted between 100 and 500 m above the surface (Buchard et al., 2014). Non-energy emissions (from trans-

portation, manufacturing, and residential sectors) are emitted in the lowest model layer. Additional information about EDGAR is found at http://edgar.jrc.ec.europa.eu/.

Anthropogenic Carbonaceous and Primary Sulfate: For anthropogenic carbonaceous (POM and BC) and primary sulfate (SO_4) aerosol emissions, we used the AeroCom Phase II dataset (HCA0 v1) described in Diehl et al. (2012) (see also see also http://aerocom.met.no/emissions.html). For carbonaceous aerosol, this database uses the 1996 gridded inventory from Bond et al. (2004) and yearly global emission trends for 17 regions from Streets et al. (2008) and Streets et al. (2009). Sectors included are residential, biofuel, industry, power, and land and inland waterway transport. These emissions from AeroCom cover the period 1979-2006. After this period, we repeat the 2006 emissions.

International Shipping: SO_4, POM and BC emissions from ocean-going ships were derived from the gridded emission dataset of Eyring et al. (2005) downscaled to $1° \times 1°$ using the EDGAR v4.1 ship SO_2 spatial distribution (Diehl et al., 2012). Annual ship emissions from 1980 to 2007 were computed via linear interpolation between the available years mapped onto the EDGAR v4.1 grid, assuming no change in shipping routes and attributions to the individual species. In MERRA-2, emissions from 2007 are repeated in subsequent years. In contrast, for ship SO_2 we use the emissions available directly from EDGAR v4.1 (European Commission, 2010). Annual emissions of ship SO_2 were available for 1975, 1980, 1985, 1990, 1995, and 2000-2005, and interpolated for the remaining years (2005 emissions are repeated thereafter).

Aircraft: Monthly aircraft emissions of sulfur dioxide derive from the AeroCom Phase II dataset (HCA0 v1) and cover the period 1976-2006; after this time emissions from 2006 are repeated. The AeroCom emissions (Diehl et al., 2012), which we vertically interpolated to the 72-layer GEOS-5 grid, were derived from a 3-dimensional gridded inventory of burned fuel generated within the framework of NASA's Atmospheric Effects of Aviation Program (AEAP). The AEAP inventory covers the years 1976, 1984, 1992, 1999, and 2015 for both scheduled and non-scheduled (military, charter, general aviation) air traffic. While the years 1976, 1984, 1992, and 1999 are based on actual aircraft data, the data for 2015 is based on a projection study, and the non-scheduled data for 1999 was derived via interpolation. The interpolation approach of Diehl et al. (2012) prevented the gradual generation of new flight patterns (*i.e.* new flight patterns are only introduced based on actual air traffic data). We convert fuel to emitted SO_2 using an emission factor of 0.8 g SO_2 per kg fuel.
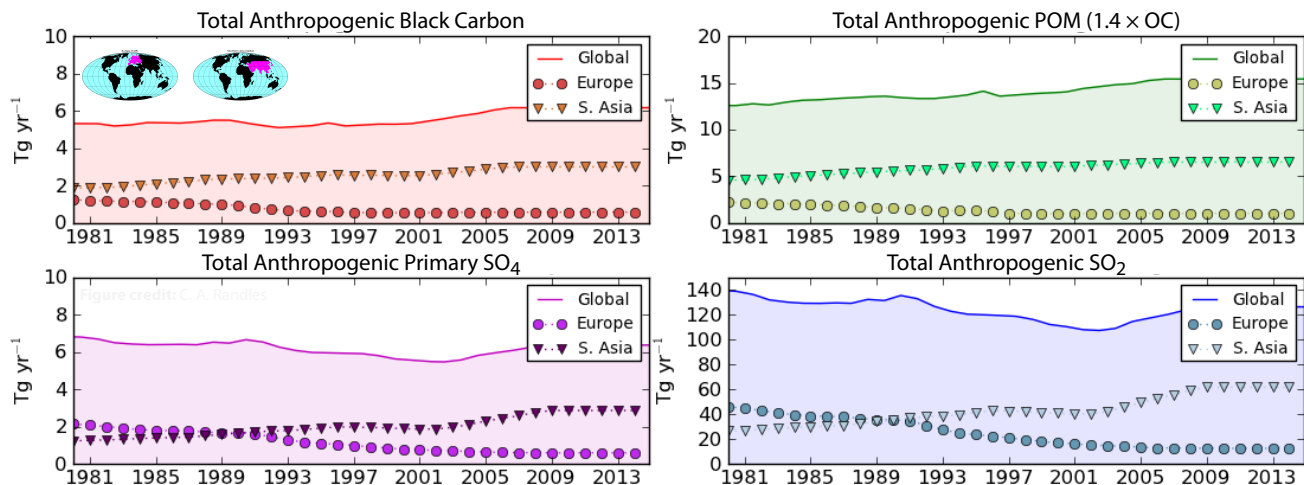
Figure 2.6: Timeseries of anthropogenic emissions from all sources (aircraft, international shipping, land transport, and energy sectors, both fossil and bio-fuels) for (a) black carbon, (b) particulate organic matter (POM = $1.4 \times$ OC), (c) primary SO_4, and (d) SO_2 gas. The solid filled line is the total global emission in Tg yr^{-1}, circles are the emissions totaled over Europe, and triangles are for the southern part of Asia (see inset maps for region definitions). Emission trends over additional regions, as well as emissions broken down by sector, can be found in Diehl et al. (2012).

2.3 Aerosol optical properties

GOCART simulates three-dimensional profiles of aerosol mass mixing ratios which are converted into vertical profiles of optical properties such as extinction, scattering, and absorption. For all aerosols besides dust, optical properties derive from Mie-theory (Wiscombe, 1980), where we have assumed a dry size distribution and spherical particles for carbonaceous and sulfate aerosols (spherical sea salt optics are resolved over the five representative dry size bins). Optical properties are primarily from the commonly used Optical Properties of Aerosols and Clouds (OPAC) data set (Hess et al., 1998). The assumed particle dry sizes for sulfate and carbonaceous aerosols can be found in Chin et al. (2002, Table 2), except the maximum radius is 0.3 μm. For most hydrophyllic aerosols (sulfate and a portion of the carbonaceous species), the impact of increased particle size with increased humidity (hygroscopic growth) is considered following Chin et al. (2002), with refractive indices and growth factors from OPAC. The sea salt sub-bin distribution follows Gong (2003) with growth factors from Gerber (1985) and refractive indices from OPAC. Note that upon emission, 80% of black carbon and 50% of particulate organic matter is considered hydrophobic. We include chemical processing, or aging, following Chin et al. (2002), converting hydrophobic aerosol to hydrophilic assuming an e-folding timescale of 2.5 days (Maria et al., 2004). We have

recently updated our dust optical properties data set to incorporate non-spherical dust properties based on Meng et al. (2010) as described in Colarco et al. (2014b). This update permits, for example, calculation of the aerosol depolarization ratio. Further details and evaluation of the aerosol optical properties are given in Colarco et al. (2010), Randles et al. (2013), Colarco et al. (2014b), and Buchard et al. (2015). In Chapter 4 we present the time-series, climatology and independent verification of MERRA-2 aerosol optical properties and vertical distribution.

Chapter 3

Aerosol assimilation in MERRA-2

We briefly describe the Goddard Aerosol Assimilation System (GAAS). More details can be found in Buchard et al. (2015) and Buchard et al. (2016).

It is important to note that GEOS-5/GOCART carries *speciated aerosol mass* as prognostic tracers. Aerosol optical depth (AOD), a column-integrated property, is derived as:

$$AOD = y = \sum_{z,i} x_i \times b_{ext,i}(RH) \times \partial z \tag{3.1}$$

where x_i is the concentration of 15 species i (dust (5 size bins), sea salt (5 size bins), hydrophobic and hydrophilic black carbon and organic carbon, and sulfate (SO_4)), ∂z is the layer thickness, and $b_{ext,i}(RH)$ is the species-specific extinction coefficient derived from Mie-theory (Section 2.3). The extinction coefficient may, depending on the species, be a function of relative humidity (RH). The assimilation constrains the simulated AOD to first order *given the speciation and vertical distribution* of aerosols simulated by the forecast model (GEOS-5/GOCART). (**N. B**. the use of Local Displacement Ensembles (LDEs) described in Section 3.1.1 can impact the strict validity of this statement). GOCART aerosol optical properties for BC, OC, sea salt, and sulfate as a function of species and relative humidity are presented in Randles et al. (2013, Supplemental Table S1 and Figure S1). Colarco et al. (2014b) details the optical treatment of dust aerosol in MERRA-2.

3.1 Aerosol optical depth (AOD) analysis splitting

The AOD analysis in GEOS-5 is performed by means of analysis splitting. First, every 3 hours a 2-D analysis of AOD is performed using error covariances derived from innovation data using the maximul-likelihood method of Dee and da Silva (1999). The AOD analysis equation can be written as:

$$
\begin{aligned}
\tau^a \equiv \mathrm{H}x^a &= \mathrm{H}(x^f + \delta x^a) \\
&= \tau^f + \delta \tau^a \\
&= \tau^f + \mathrm{H}\mathbf{P}^f\mathrm{H}^T(\mathrm{H}\mathbf{P}^f\mathrm{H}^T + \mathbf{R})^{-1}(\tau^o - \mathrm{H}x^f)
\end{aligned}
\tag{3.2}
$$

AOD is denoted by τ. The superscripts o, f and a indicate observation, forecast, and analysis, respectively. H is the linear observation operator that converts aerosol mass concentration (x) to AOD. The operators $\mathbf{P}^f$ and $\mathbf{R}$ are the background and observation error covariance matrices, respectively. The AOD analysis increments $\delta \tau^a$ are computed using a 2D version of the Physical-space Statistical Analysis System (PSAS, Cohn et al., 1998). For algorithm consistency, this analysis is performed using a natural log-transformed control variable ($\eta = \ln(AOD + 0.01)$; Section 3.1.2).

Once the AOD analysis increments are obtained, the next step is to derive 3D analysis increments for the mixing ratio of each aerosol species, δx_i^a. Previous studies (e.g. Zhang et al., 2008, and references therein) have opted to simply scale the mixing ratio increments as to promote consistency with the analyzed AOD at each gridpoint, a procedure that does not make any use of error covariance information. Here we seek a relationship relating analysis increments of AOD to analysis increments of aerosol species mixing ratio that involve the corresponding error covariance operators. From the mixing ratio analysis equation implicit in Equation 3.2, the vertical structure of δx^a is determined by the operator $\mathbf{P}^f\mathrm{H}^T$. Therefore we seek an operator $\mathbf{Q}$ such that

$$
\delta x^a = \mathbf{P}^f\mathrm{H}^T\mathbf{Q}\delta \tau^a
\tag{3.3}
$$

Imposing the condition $\mathrm{H}\delta x^a = \delta\tau^a$ leads to

$$\mathbf{Q} = (\mathrm{H}\mathbf{P}^f\mathrm{H}^T)^{-1} \tag{3.4}$$

Substituting Equation 3.4 into Equation 3.3 we arrive at:

$$\delta x^a = \mathbf{P}^f\mathrm{H}^T(\mathrm{H}\mathbf{P}^f\mathrm{H}^T)^{-1}\delta\tau^a \tag{3.5}$$

Notice that the observation error covariance matrix $\mathbf{R}$ is not involved in Equation 3.5, and that this expression is invariant to any scaling of the background error covariance operator $\mathbf{P}^f$.

In principle, solving Equation 3.5 requires the 3D error covariance operator, including vertical and horizontal correlations. However, for computational reasons, we solve this equation for each vertical column separately, as the main purpose of this step is to project the horizontal AOD increments into the vertical and across species. As described in Buchard et al. (2015) and Section 3.1.1, we employ a Local Displacement Ensemble (LDE) formulation to solve Equation 3.5.

3.1.1   Local Displacement Ensembles (LDEs)

In order to evaluate Equation 3.5 we employ an ensemble formulation. Let

$$\mathbf{X} = \begin{pmatrix} x_1 & x_2 & ... & x_E \end{pmatrix} \tag{3.6}$$

where $\mathbf{X}$ is a $n_q \times n_E$ matrix (n_q is the number of aerosol concentration tracers times the number of vertical levels and n_E is the number of ensemble perturbations), for a particular column. From Equation 3.2 it follows that

$$\begin{aligned} \mathbf{Y} \equiv \mathrm{H}\mathbf{X} &= \begin{pmatrix} \mathrm{H}x_1 & \mathrm{H}x_2 & ... & \mathrm{H}x_E \end{pmatrix} \\ &= \begin{pmatrix} \tau_1 & \tau_2 & ... & \tau_E \end{pmatrix} \end{aligned} \tag{3.7}$$

Approximating the background error covariance matrix by $\mathbf{P}^f \sim \mathbf{XDX}^T$, where $\mathbf{D}$ is a diagonal matrix allowing for the weight of the ensemble perturbations, Equation 3.5 can be written as the unbiased linear regression equation:

$$\delta x^a = \mathbf{XDY}^T(\mathbf{YDY}^T)^{-1}\delta\tau^a \tag{3.8}$$

At this point we have made no assumption about the nature of the ensemble perturbations. MERRA-2 did not include an ensemble of aerosol forecasts, and a practical approach was developed to produce ensemble perturbations capable of producing realistic speciation and vertical structures for the mixing ratio analysis increments. The underlying assumption of our error covariance modeling exercise is that aerosol forecast errors are due primarily to misplacements of aerosol plumes. Implicit in this assumption is that the AOD analysis (Eq. 3.2) removes any systematic biases. For each gridpoint, ensemble perturbations are formed by computing the difference of background aerosol mixing ratios from this central gridpoint and adjacent gridpoints within a radius R (taken as 1,000 km in MERRA-2). Ensemble perturbations are weighted according to $\exp(-4(\tau^f - \tau^a)^2)$ so that nearby gridpoints that better match the AOD analysis receive higher weights.

3.1.2   Choice of control variable for the 2D AOD Analysis

Since AOD is not a normally distributed variable (e.g. O'Neill et al., 2000), the 2D analysis in Equation 3.2 is performed using the natural log-transformed AOD,

$$\eta = \ln(\tau + \epsilon) \tag{3.9}$$

as the control variable. The parameter $\epsilon = 0.01$ is chosen as to render the distribution closest to a Gaussian using a probability plot technique (Chambers et al., 1983). Notice that for small values of τ the log-transformed variable η is linear in τ and approaches $\ln\tau$ for large AOD. This choice of control variable avoids the classical problem of log-normal distributions for small values of τ and allows for multiplicative rather than additive corrections for large τ (Henze et al., 2009; Saide et al.,

2013). Notice that AOD errors τ' are related to η' errors by

$$\tau' \approx (\tau + \epsilon)\eta' \tag{3.10}$$

Therefore, even when η errors are Gaussian and flow independent, AOD errors are a sum of flow dependent ($\tau\eta'$) and flow independent ($\epsilon\eta'$) components. To preserve linearity, analysis increments $\delta\eta^a$ are converted back to $\delta\tau^a$ before use in Equation 3.8.

3.1.3 AOD background correction and approximate analysis averaging kernel

The MERRA-2 meteorological analysis is performed 6-hourly, while the AOD analysis occurs every 3 hours. For efficiency reasons, the overall analysis cycle in MERRA-2 is controlled by the meteorological assimilation, with two independent AOD analyses being performed within each cycle. Consider the 12Z analysis cycle. The AOD analysis is performed at 9Z and 12Z, using backgrounds that are forecasts from 6Z. The corresponding update of the GEOS-5 aerosol state occurs at 9Z and 12Z. At 12Z the proper background state should be a forecast from 9Z rather than from 6Z as in the (off-line) AOD analysis. Therefore a background correction is in order to account for this mismatch in background states. Denoting the previous AOD analysis and background by $\hat{\tau}^a$ and $\hat{\tau}^f$, respectively, it can be shown that

$$\tau^a = \hat{\tau}^a + (\mathbf{I} - \mathbf{A})\left(\tau^f - \hat{\tau}^f\right) \tag{3.11}$$

where τ^a and τ^f are the proper analysis and forecast at 12Z, and $\mathbf{A} = \mathbf{K}\text{H}$ is the analysis averaging kernel with $\mathbf{K}$ being the usual Kalman gain. For typical satellite swaths, the operator $\mathbf{A}$ evaluates to approximately zero outside the swath leading to simple replacement of background in those regions; elsewhere Equation 3.11 provides a background correction that depends on the details of the analysis.

In practice, a diagonal approximation for the analysis averaging kernel $\mathbf{A}$ is utilized. In such approximation, an additional AOD analysis is performed with all innovations set to 1 while preserving
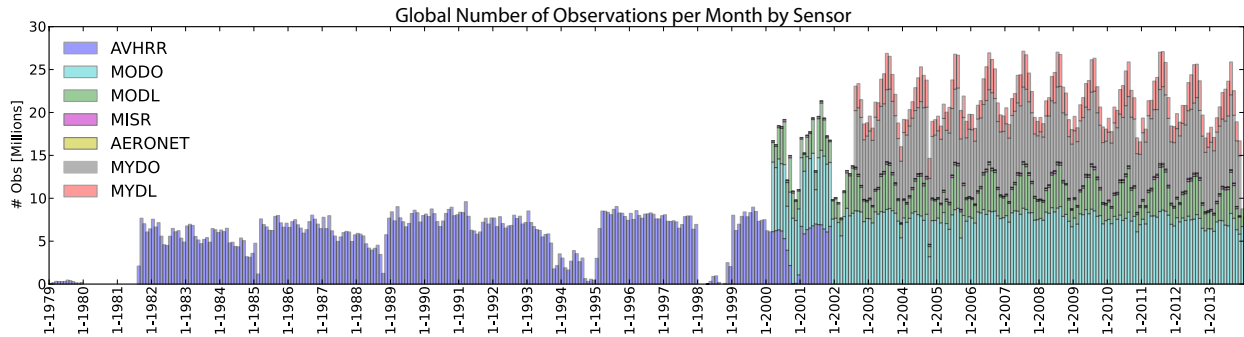
20

Figure 3.1: Total global monthly observations from AVHRR, MODIS Terra over land (MODL) and ocean (MODO), MODIS Aqua over land (MYDL) and ocean (MYDO), MISR over bright surfaces (deserts), and AERONET. Note the data counts for AERONET and MISR are very small compared to MODIS. Stronger cloud contamination in the Southern Hemisphere relative to the Northern Hemisphere imparts a seasonal variation on the data volume for the satellite sensors during the EOS period.

the actual observational coverage. This averaging kernel field is computed as the second step of each AOD analysis and is provided as an additional diagnostic for MERRA-2. Such an algorithm can be derived as a limiting case of a banded approximation for the Kalman gain **K** (derivation not shown).

3.2 Observations and errors

3.2.1 Aerosol observing system

The observing system sensors used by the GAAS are shown in Table 3.1. Here we provide a brief description of each sensor and its AOD retrieval algorithm(s). Additional information can be found in the cited publications. Figure 3.1 shows the total number of monthly global observations used in

Table 3.1: MERRA-2 aerosol optical depth (AOD) Observing System Sensors

Sensor	Temporal Coverage	Description
AVHRR NNR*	1979 - August 2002	PATMOS-x radiances over ocean only (PM orbit)
AERONET	Station Dependent ($\sim$1999 - October 2014)	AOD from land station network
MISR	February 2000 - June 2014	AOD over bright land surfaces only (albedo > 0.15)
MODIS Terra NNR*	March 2000 - present (NRT**)	"Dark Target" C5 land and ocean radiances (AM orbit)
MODIS Aqua NNR*	August 2002 - present (NRT**)	"Dark Target" C5 land and ocean radiances (PM orbit)

N.B.: *NNR refers to Neural Net Retrieval (See Section 3.2.2). **MODIS data is available in Near Real Time (NRT).

the assimilation by sensor. Note that Advanced Very High Resolution Spectroradiometer (AVHRR) observations are only over the ocean, and the seasonal cycle in the MODIS observations is due to the orbital coverage of the satellite combined with higher cloud contamination at high latitudes. Figures 3.2 and 3.3 show the climatological annual mean number of observations and annual mean log-transformed AOD (*i.e.* Eq. 3.9; hereafter referred to as log-space or log-transformed) for each satellite sensor and the ground-based network used in MERRA-2. Note that the log-transform of the AOD is taken to make the AOD distribution more Gaussian, an assumption necessary for most statistical calculations. The offset value $\epsilon = 0.01$ in Eq. 3.9 insures that no negative values are obtained from the log-transform of AOD.

- **Advanced Very High Resolution Spectroradiometer (AVHRR):** A series of 10 AVHRRs have flown on NOAA polar-orbiting satellites for over 25 years. We utilize the 25-year record of AOD retrieved from the inter-calibrated radiances in the AVHRR Pathfinder Atmosphere-Extended (PATMOS-x) data set. The PATMOS-x radiance dataset was recalibrated using radiances from MODIS (Heidinger et al., 2014). **N. B.** The aerosol assimilation does not use the official PATMOS-x AOD product, but rather the Neural Net Retrieval AOD derived from radiances and described in Section 3.2.2.

- **AEROsol RObotic NETwork (AERONET):** AERONET is a global ground-based network of automatic sunphotometers that measure direct sun and sky radiances at several wavelengths (Holben et al., 1998). AOD is obtained from direct sun measurements with an accuracy to within $\pm\, 0.015$. In the assimilation, we used cloud-screened Level 2.0 data (quality assured) (Smirnov, 2000). Because it is not available in NRT, AERONET data assimilation stops on October 29, 2014.

- **MODerate Resolution Imaging Spectroradiometer (MODIS):** The MODIS instruments aboard the Terra and Aqua spacecraft provide approximately two-day coverage of the global multi-spectral aerosol optical depth at 10×10 km^2 resolution (Remer et al., 2008). NASA Earth Observing System (EOS) Terra was launched in December 1999, and the MODIS Terra sensor retrieves AOD at approximately 10:30 local solar time at the equator. NASA EOS Aqua launched in May 2002, and the MODIS Aqua sensor retrieves AOD at approximately 13:30 local solar time at the equator. AOD is retrieved separately over land (Levy et al., 2007, "Dark Target") and ocean (Remer et al., 2005). **N. B.** The aerosol assimilation does not use the official MODIS Collection 5 AOD product, but rather the Neural Net Retrieval AOD derived from Collection 5 MODIS radiances (see Section 3.2.2).

- **Multi-angle Imaging SpectroRadiometer (MISR):** The MISR instrument flying on the Terra spacecraft uses multiple camera views to retrieve multi-spectral aerosol optical properties including aerosol optical depth at 16×16 km^2 spatial resolution with about eight-day global coverage. MISR's multi-angle capability allows for aerosol characterization and retrievals over bright surfaces (Diner et al., 1998; Kahn et al., 2005). **N. B.** To provide observations in regions where MODIS C5 Dark Target does not retrieve AOD, in MERRA-2 we use MISR AOD version 22 retrievals ONLY over bright surfaces (albedo > 0.15) in the aerosol assimilation. Because it is not available in NRT, MISR data assimilation stops on June 30, 2014.

3.2.2   Bias correction: Neural Net Retrievals

Satellite aerosol product assimilation requires careful data quality assurance and bias removal (Zhang et al., 2014). GEOS-5 includes assimilation of bias-corrected AOD observations from AVHRR and the MODIS sensors on both Terra and Aqua satellites. The bias correction algorithm involves cloud screening and homogenization of the observing system by means of a neural net scheme that translates cloud-cleared observed reflectances into AERONET-calibrated AOD (referred to hereafter as the Neural Net Retrieval or NNR). Based on the work of Zhang and Reid (2006) and Lary et al. (2010), we originally developed a back-propagation neural network to correct observational biases in MODIS AOD operational retrievals. Later this system evolved into a neural net type of retrieval using observed reflectances. Note that in addition to the bias correction from the neural net scheme, upon assimilation of the NNR AOD in GAAS, online quality control is performed with the adaptive buddy check of Dee et al. (2001).

To derive 10-km resolution MODIS NNR AOD, over-ocean predictors include Level-2 multi-channel top-of-the-atmosphere (TOA) reflectances, glint, solar and sensor angles, cloud fraction (pixels are discarded when cloud fraction $> 70\%$), and albedo derived using GEOS-5 surface wind speeds. Over land, predictors are the same, except the climatological albedo is included for pixels with surface albedo < 0.15. The target of the NNR algorithm is the log-transformed AERONET AOD. For the AVHRR NNR AOD, the neural net predictors over ocean are the AVHRR Pathfinder Atmosphere-Extended (PATMOS-x) TOA radiances at 630 and 860 nm (Heidinger et al., 2014), total precipitable water (TPW), ocean albedo (wind speed), solar and sensor angles, and the climatological GEOS-5 fractional AOD speciation. The AVHRR NNR targets the MODIS NNR AOD
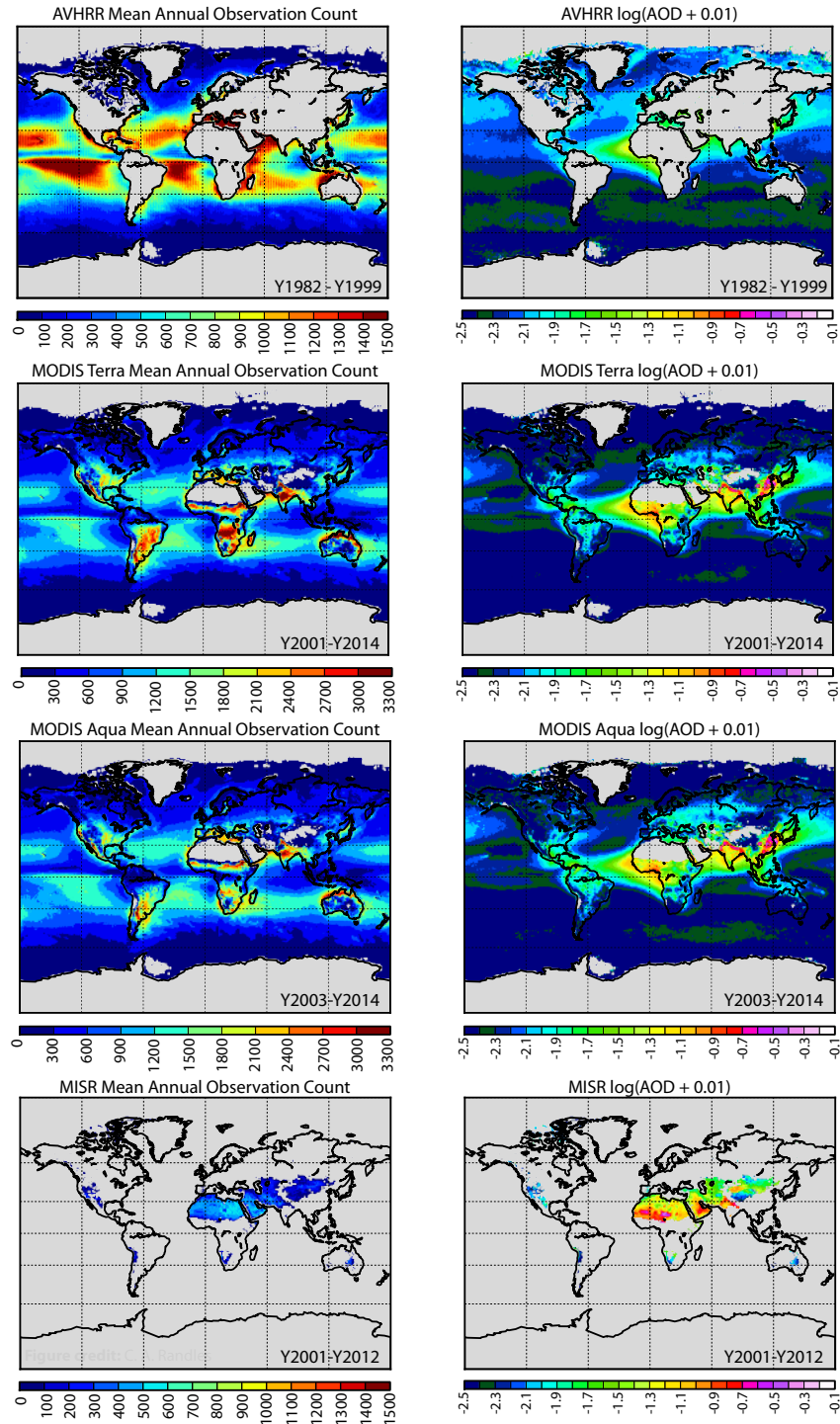
Figure 3.2: Climatological annual-mean number of observations (left) and annual mean $\log(AOD + 0.01)$ (right) included in the assimilation from AVHRR (top row 1982-1999), MODIS Terra (second row; 2001-2014), MODIS Aqua (third row; 2003-2014), and MISR (bottom row; bright surface only; 2001-2012). Grey shading indicates regions with no data. Note the different scales for the observation counts.
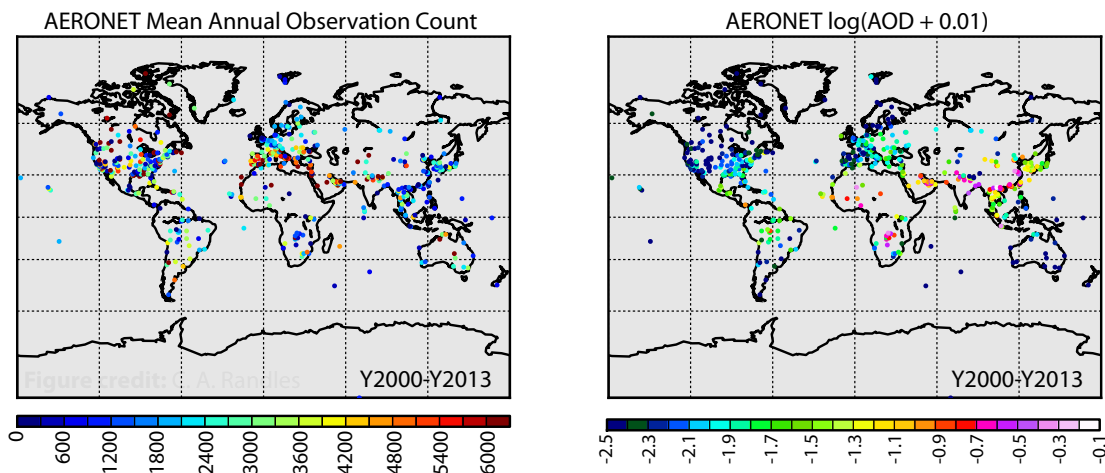
Figure 3.3: Same as Figure 3.2 but for AERONET (2000-2013) observations. Note that not all stations have observations covering the entire period. Grey shading indicates regions with no data.

for consistency of the observing system (Fig. 3.4).

The performance of the MODIS C5 NNR AOD observations were evaluated against other observational datasets in the WRF-Chem data assimilation system (Saide et al., 2013). Post-processing techniques such as the NNR reduce biases relative to independent AERONET observations of AOD compared to assimilation of operational MODIS Level 2 retrievals. Additionally, compared to other AOD bias correction schemes (e.g. Zhang and Reid, 2006), Saide et al. (2013) found that the NASA NNR retrieval produces higher error reductions because of a less restrictive cloud fraction requirement (and thus increased data availability).

Figure 3.5 shows the impact of the Neural Net Retrieval (NNR) bias correction on MODIS Aqua AOD. Clearly, the NNR algorithm greatly reduces the bias in AOD relative to AERONET, where the stations considered were not used in the training of the neural network. Figure 3.6a compares the PATMOS-x AVHRR AOD to AERONET, and Figure 3.6b compares this same AVHRR AOD to our previous aerosol assimilation (MERRAero). The original observations (Fig. 3.6a) show a high bias compared to AERONET. Compared to MERRAero, which included assimilation of MODIS NNR AOD, we primarily see that the AVHRR observations are biased for lower AOD. Breaking down the AVHRR comparison to MERRAero by species (as determined from MERRAero; Fig. 3.7, left column), we can see much of the bias in the total AOD relative to MERRAero (Fig. 3.6a and 3.6b) is due to sea-salt aerosol (Fig. 3.7e). Bias-correction of the PATMOS-x AVHRR AOD (Fig. 3.7, right column) removes the biases both for the total AOD as well as the biases in the
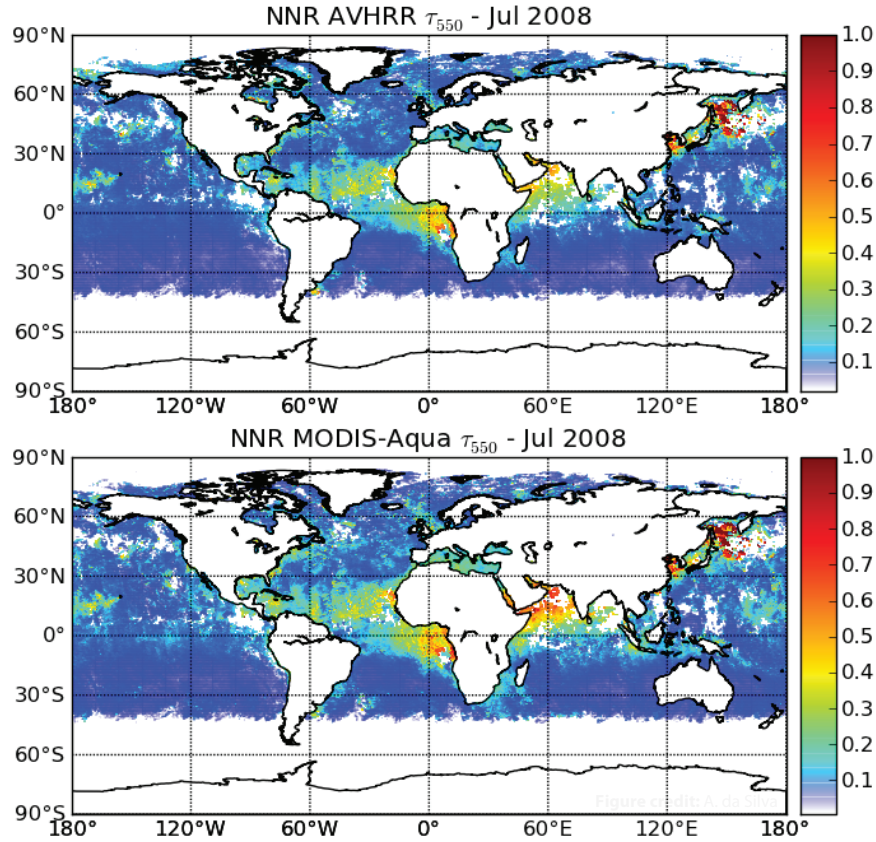
Figure 3.4: Comparison of AVHRR NNR AOD (top) and ocean-only MODIS Aqua NNR AOD (bottom) in July 2008 at 550 nm. Here we see that the the NNR retrieval used for AVHRR provides continuity in the distribution of AOD between these two sensors.

species-specific AOD compared to MODIS NNR AOD.

3.2.3 Observation and background model error

Recall that forecast error (background error covariance matrix $\mathbf{P}^f$) is computed from innovation time-series (observation - forecast difference; $\tau^o - \mathbf{H}x^f$) using the maximum likelihood algorithm of Dee and da Silva (1999) (Section 3.1). An upper limit of the updated forecast model error is the standard deviation of observation minus forecast ($O - F$) shown in Figure 3.8. Note that this upper bound on error is reduced for MODIS Aqua compared to MODIS Terra because the forecast time for the former more recently was impacted by observations. The morning overpass time of Terra means that the forecast was last informed by observations the previous day at the latest. Figure 3.9 compares the background (forecast) AOD and analysis AOD by sensor. This shows that
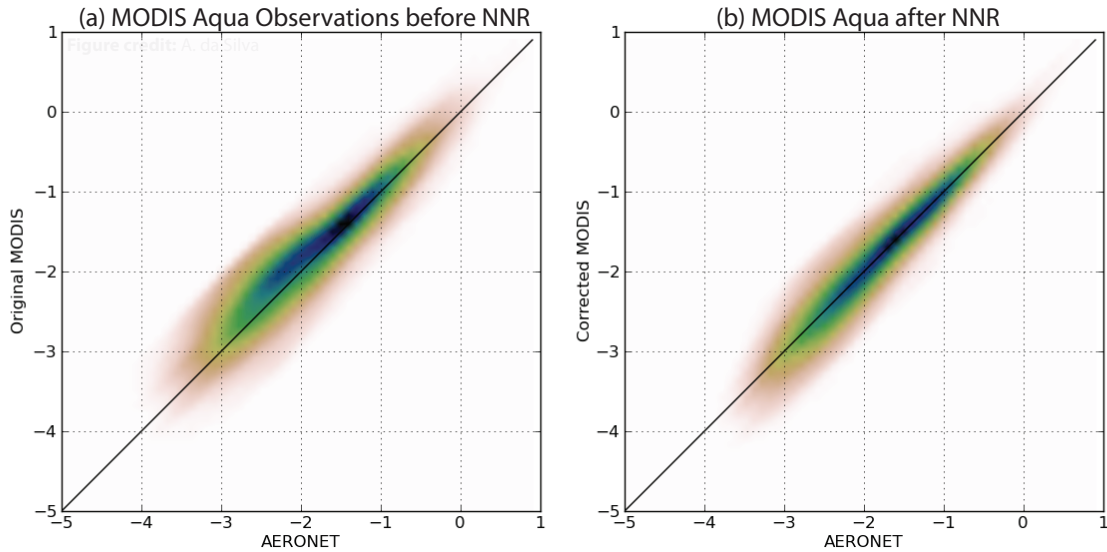
Figure 3.5: Comparison of MODIS Aqua AOD to co-located AERONET observations (a) prior to bias correction and (b) after bias-correction using the neural network retrieval (NNR). Note, here we show $\log(AOD + 0.01)$.
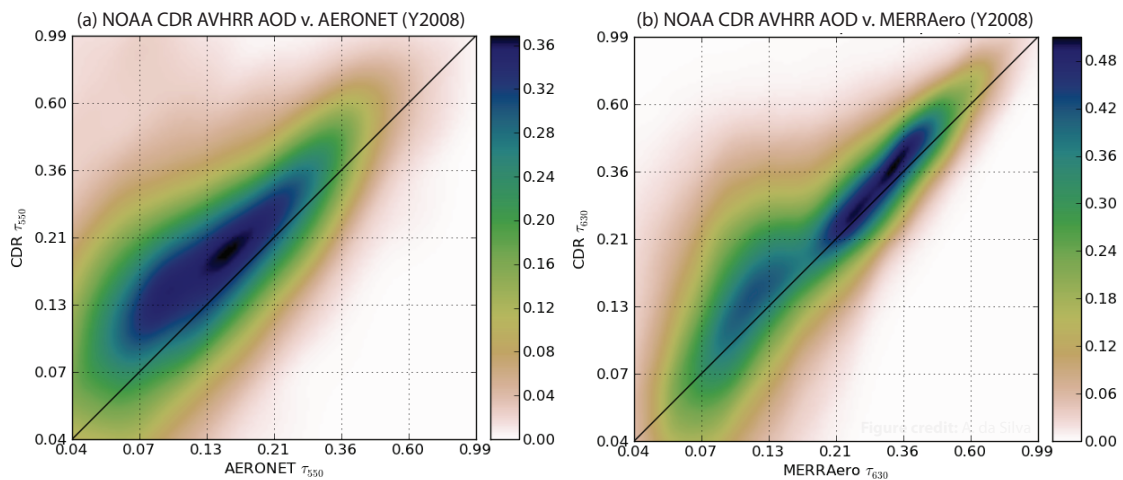
Figure 3.6: Comparison of the NOAA AVHRR Pathfinder Atmosphere-Extended (PATMOS-x) Climate Data Record (CDR) to AERONET (left) and MERRAero (right) at 630 nm. All comparisons are for Y2008.
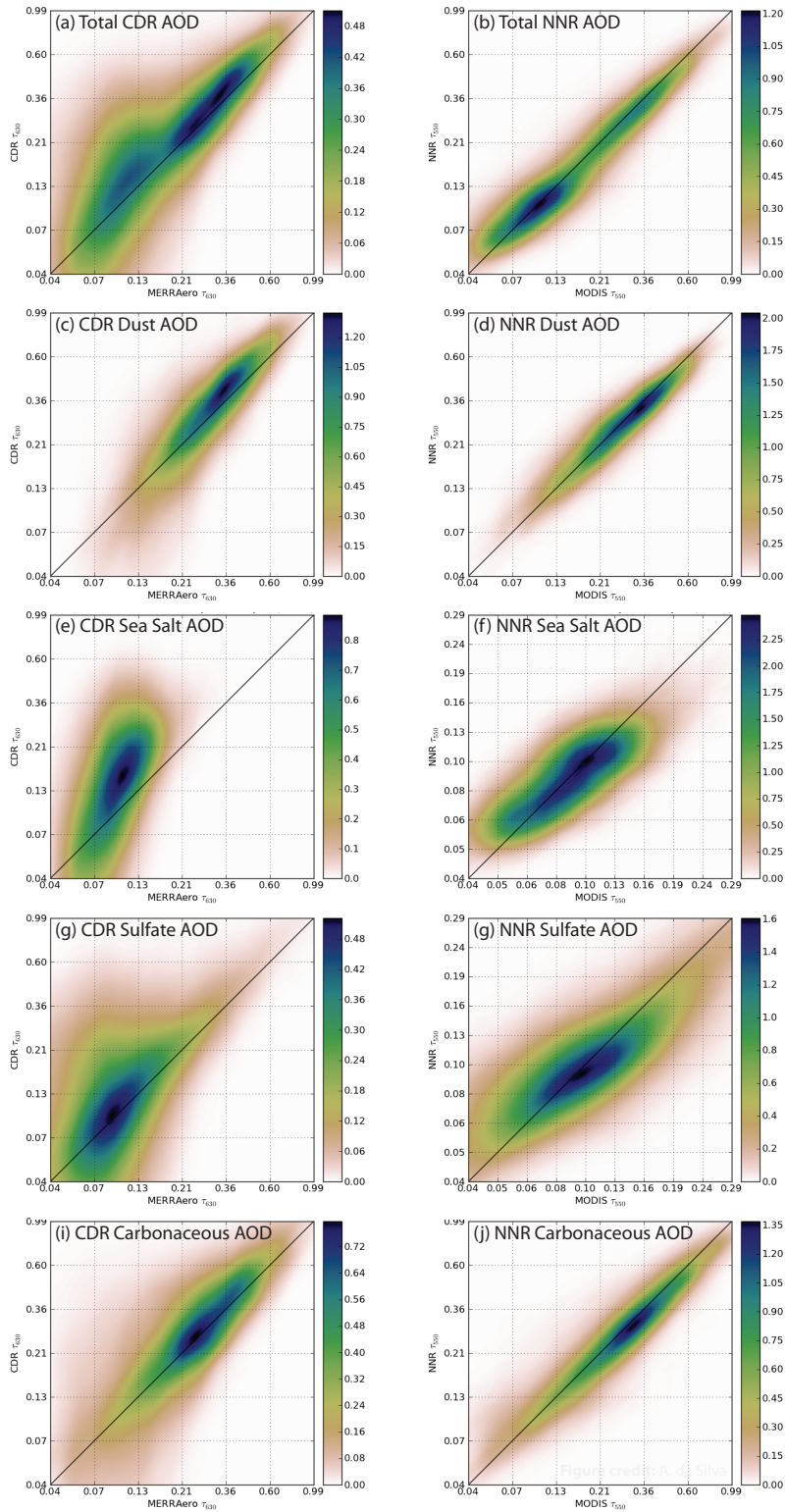
Figure 3.7: Comparison of the AVHRR PATMOS-x AOD to MERRAero (left column) for the total aerosol optical depth (top row) and stratified by aerosol species (remaining rows). A similar comparison is shown in the right column, but now comparing the AVHRR NNR AOD to MODIS NNR observations.

28
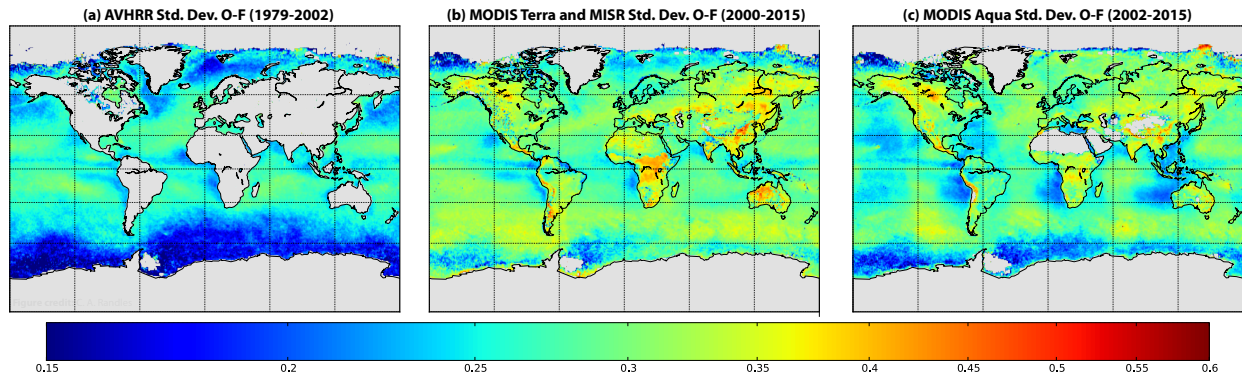
Figure 3.8: Standard deviation of observation minus forecast ($O - F$) for (a) AVHRR, (b) MODIS Terra plus MISR over bright surfaces, and (c) MODIS Aqua. This represents the upper bound of the forecast error in log-transformed AOD space.

on average, the analysis resembles the background (forecast), though there are clear regions where a strong impact of observations can be seen (e.g. over parts of Asia and northern Africa).

3.3 Assimilation innovation statistics ($O - F$ and $O - A$)

Table 3.2 shows for pairwise observations (O) and forecast (F) or assimilation (A) data, the Pearson's correlation coefficient (r), the root mean square of the difference (RMS), the standard deviation of the differences (STDV), and the mean difference (mean $O - F$ or $O - A$). All statistics are calculated in log-space ($\log(AOD + 0.01)$). Probability distribution functions (PDFs) of observation minus forecast ($O - F$) and observation minus analysis ($O - A$) in log-space for each sensor in Table 3.2 are shown in Figure 3.10. PDFs are calculated by fitting a gaussian kernel density estimator (KDE, Scott, 1992; Silverman, 1986) to all co-located (spatial and temporal) observed and modeled (analysis or forecast) AODs in log space covering the years indicated. Note that for AVHRR, here we only consider years after the Pinatubo volcanic eruption (1993 – onward). In Section 4.8 we explain the impacts of this major volcanic eruption on the assimilation and speciated AOD. With the exception of the MISR instrument, the GEOS-5 forecast indicates lower AOD than observed. After the assimilation, the differences between the analysis and observations ared reduced towards zero, though there is more spread in the distribution over land compared to over ocean. The spread in the $O - A$ distributions are due in part to the influence of other sensors. Figure 3.11 summarizes the improved statistics between sensor observations and the analysis as compared to the forecast in the form of Taylor diagrams.
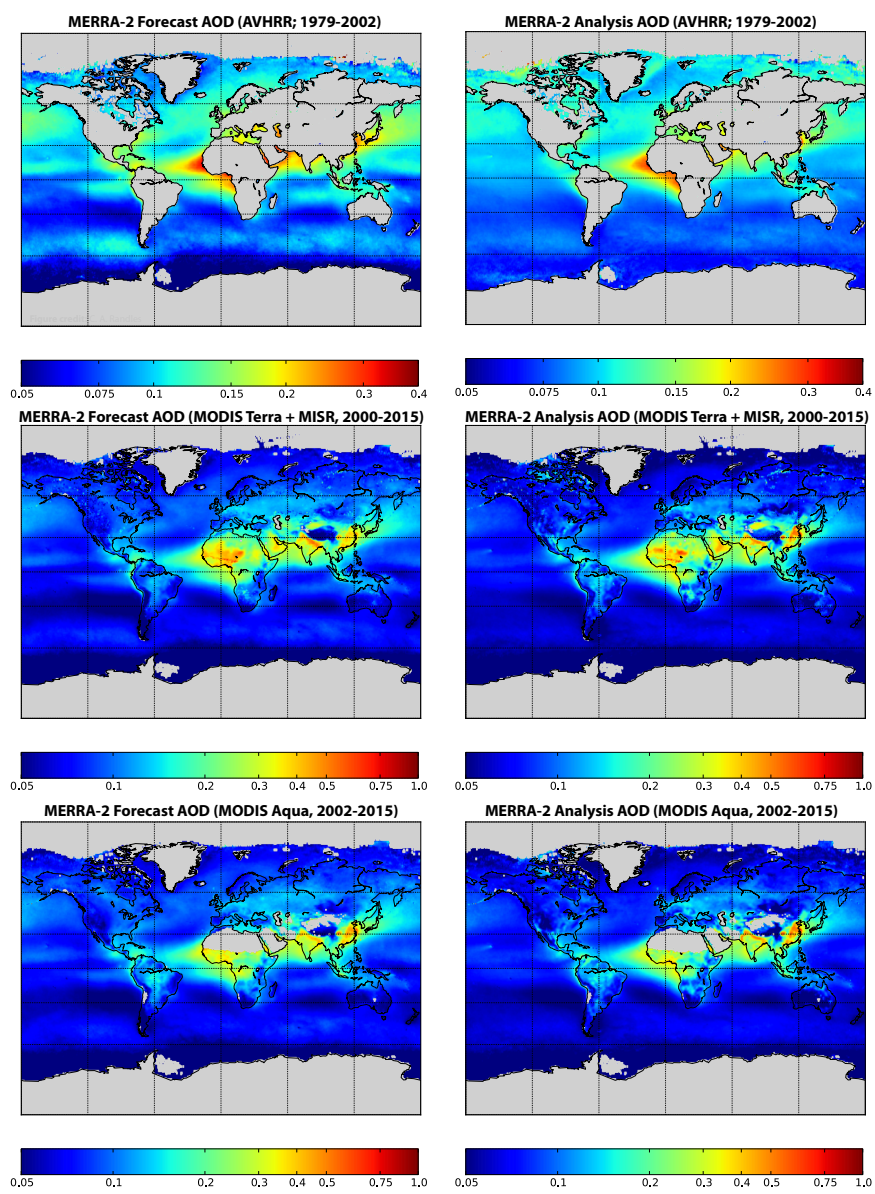
Figure 3.9: Background (left column) and analysis (right column) AOD for AVHRR (top row), MODIS Terra plus MISR over bright surfaces (middle row), and (c) MODIS Aqua (bottom row). Grey regions are regions of no data.

Table 3.2: MERRA-2 statistical relationship between pairwise observations (O) and forecast (F) or assimilation (A) computed in log-transformed space.

Sensor	n	r	STDV	RMS	BIAS
Forecast Statistics (O vs. F or $O - F$ for Bias)					
AVHRR (1993-1999)	62,509,004	0.827	0.317	0.363	-0.177
AERONET (2000-2013)	230,629	0.896	0.370	0.372	-0.038
MISR (2001-2012)	2,269,842	0.822	0.419	0.431	0.100
MODIS Terra Ocean NNR (2001-2014)	92,276,142	0.992	0.321	0.328	-0.081
MODIS Terra Land NNR (2001-2014)	37,129,053	0.876	0.426	0.428	-0.042
MODIS Aqua Ocean NNR (2003-2014)	94,671,744	0.991	0.288	0.303	-0.102
MODIS Aqua Land NNR (2003-2014)	30,808,987	0.878	0.400	0.413	-0.105
Analysis Statistics (O vs. A or $O - A$ for Bias)					
AVHRR (1993-1999)	62,509,004	0.972	0.129	0.129	-0.005
AERONET (2000-2013)	230,629	0.975	0.187	0.188	-0.019
MISR (2001-2012)	2,269,842	0.930	0.239	0.239	0.011
MODIS Terra Ocean NNR (2001-2014)	92,276,142	0.997	0.115	0.115	-0.013
MODIS Terra Land NNR (2001-2014)	37,129,053	0.967	0.220	0.220	-0.010
MODIS Aqua Ocean NNR (2003-2014)	94,671,744	0.996	0.117	0.117	-0.009
MODIS Aqua Land NNR (2003-2014)	30,808,987	0.962	0.239	0.239	-0.006

n = number of co-locations for time period indicated,
r = Pearson's correlation coefficient,
STDV = standard deviation of the differences,
RMS = root mean square of the differences, BIAS = mean $O - F$ or $O - A$
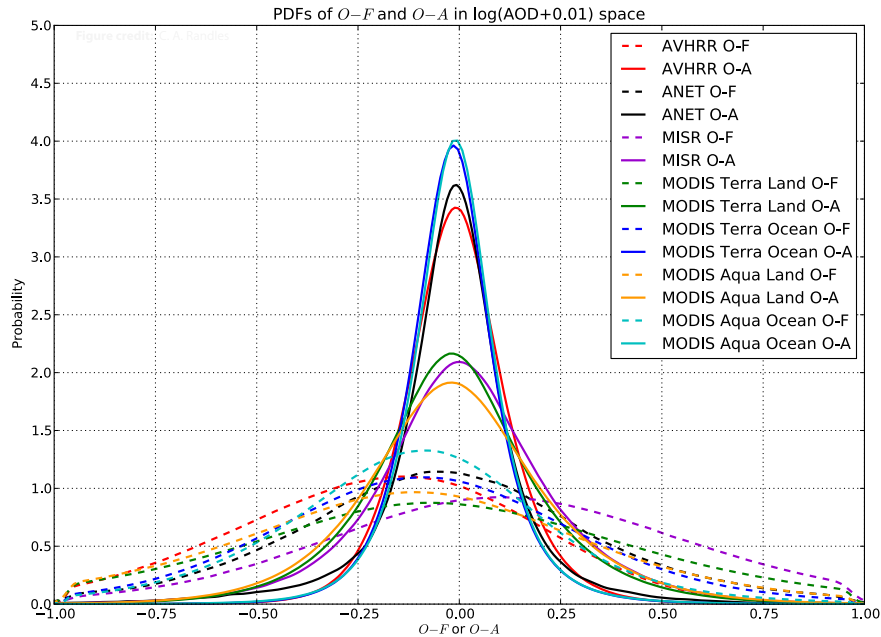
Figure 3.10: Probability distribution functions of all $O - F$ (dashed lines) and $O - A$ (solid lines) for AVHRR, MODIS, MISR, and AERONET (ANET). PDFs are for the time periods listed for each sensor in Table 3.2.
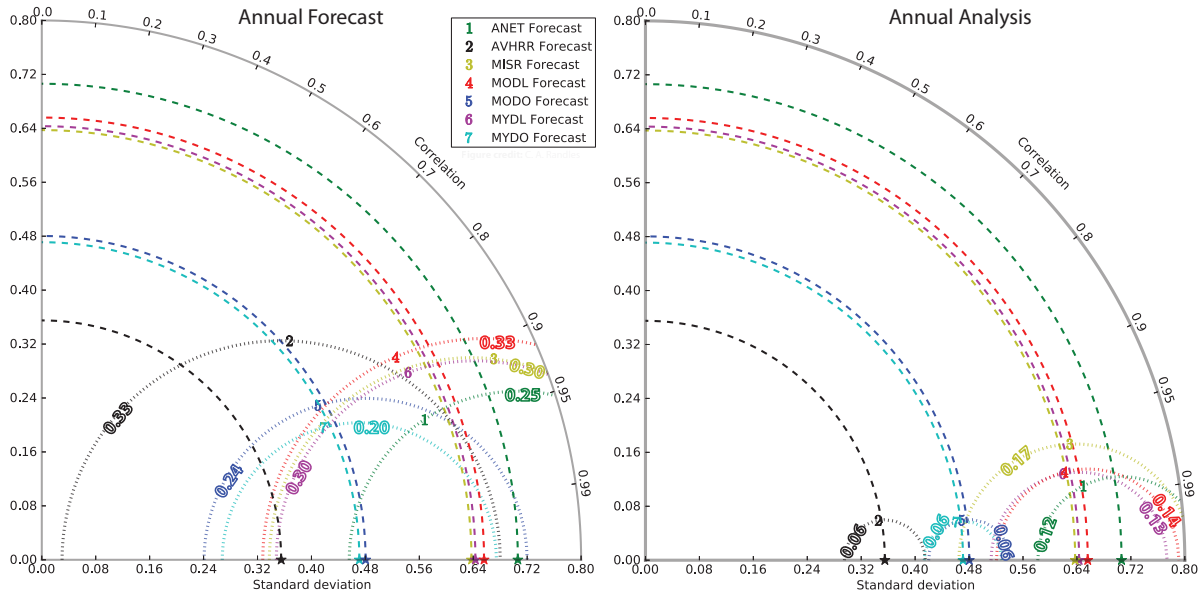
Figure 3.11: Taylor diagram comparing standard deviation (radial distance), Pearson's correlation (angle), and root mean square error (RMSE; dotted circles) between the annual forecast (left panel, colored numbers) or annual analysis (right panel, colored numbers) and the reference sensor (stars for standard deviation). For all sensors, after the analysis the correlation is improved, and RMSE and bias are reduced. Statistics are for the time periods listed for each sensor in Table 3.2.

The climatological mean spatial distribution of $O - F$ for each sensor in Table 3.1 is shown in Figure 3.12. Red shading indicates that the observations are higher than the forecast in logarithmic space, and blue shading indicates the opposite condition. AVHRR and MODIS indicate that the forecast underestimates $\log{(AOD + 0.01)}$ over the ocean in the Southern Hemisphere, at high latitudes, and over biomass burning regions. These biases are reduced greatly in the analysis (not shown), but remain higher over land compared to ocean. Over dusty regions observed by MISR, the forecast underestimates $\log{(AOD + 0.01)}$, with biases largely removed in the analysis (not shown). Biases in the analysis are generally spatially similar to the forecast biases; however, their magnitude is greatly reduced (not shown).
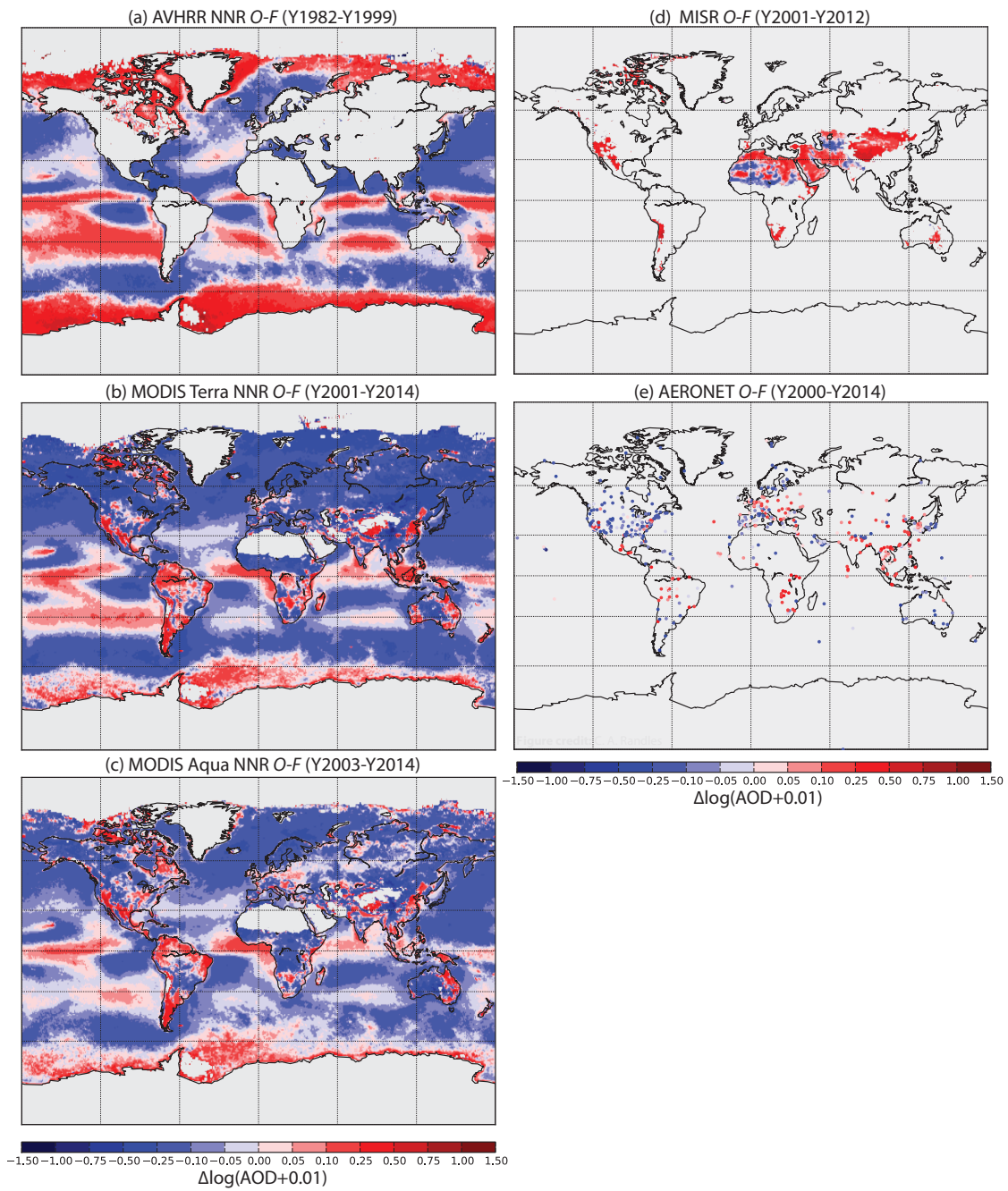
Figure 3.12: Climatological mean $O - F$ in $\log(AOD + 0.01)$ space for (a) AVHRR NNR, (b) MODIS Terra NNR, (c) MODIS Aqua NNR, (d) MISR, and (e) AERONET. *N. B.* Annual means were computed using only the years cited on each panel, and only for years with all months present. Red shading indicates that the observations are higher than the forecast; blue shading indicates the opposite case. Grey regions indicate no observations. Differences are in log-transformed space.

Chapter 4

Evaluation of aerosols in MERRA-2

We present an overview evaluation of the aerosol fields produced by the MERRA-2 GAAS. First, in Section 4.2 we review the climatology of assimilated AOD in MERRA-2 and compare it to our previous aerosol reanalysis, MERRAero (Buchard et al., 2015). We validate MERRA-2 AOD with available independent station and aircraft observations in Section 4.3. Simulated Aerosol Index (AI) and Aerosol Absorption Optical Depth (AAOD) are compared to retrievals from the Ozone Monitoring Instrument (OMI) and MERRAero in Section 4.4. Section 4.5 shows the climatological zonal mean vertical distribution of aerosol species as well as verification of vertical aerosol mass and optical properties compared to satellite and aircraft measurements. Surface mass ($PM_{2.5}$) is evaluated with ground-based networks over the continental United States and East Asia in Section 4.6. We evaluate the performance of dust transport and the simulation of sea salt aerosol (Section 4.7), and the stratospheric aerosol associated with the Pinatubo eruption and consequences of this eruption on the assimilation appear in Section 4.8. The purpose of this evaluation is not to provide an exhaustive assessment of the MERRA-2 aerosol products, but it does point out key features and limitations of the aerosol products. Further validation and evaluation of MERRA-2 aerosols will appear in the peer-reviewed literature (see http://gmao.gsfc.nasa.gov/reanalysis/MERRA-2/pubs/).
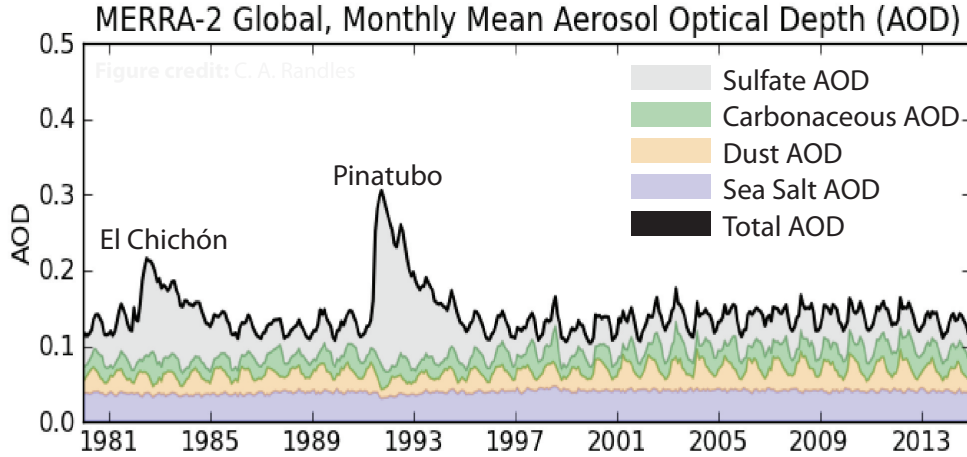
Figure 4.1: Global, area-weighted average monthly-mean 550 nm AOD from MERRA-2 and contributions from various aerosol types. The carbonaceous aerosol AOD is the sum of organic plus black carbon AOD. Timeseries of AOD for various regions over the globe are presented in Appendix B.

4.1 Timeseries of AOD

We begin the evaluation of the MERRA-2 aerosol assimilation by examining the assimilated aerosol property, the aerosol optical depth (AOD). This is the **only** aerosol property **directly** constrained by the Goddard Aerosol Assimilation System (GAAS). The speciation of aerosols, their vertical distribution, the relationship between aerosol mass tracers and AOD (e.g. individual aerosol species extinction, hygroscopic growth, absorption, and asymmetry parameters), are not directly constrained by the assimilation of the two-dimensional, column-integrated AOD. Rather, they are the result of the convolution of the parameterizations and assumptions of the underlying forecast model (GEOS-5/GOCART), the observationally-constrained AOD through the assimilation process (Eq. 3.1), and the Local Displacement Ensemble method (LDE) described in Section 3.1.1.

4.2 Temporal and spatial patterns of AOD

Figure 4.1 presents the globally, area-weighted monthly-mean time series of AOD with contributions from the various aerosol species simulated in GOCART. Despite the use of various emission inventories over time (e.g. biomass burning emissions discussed in Section 2.2) and a changing observing system (Section 3.2), the total AOD timeseries (black line) shows relative stability without obvious spurious jumps or trends. Apparent in the time series are the eruptions of the El Chichón

and Pinatubo volcanoes in 1982 and 1991, respectively. These eruptions injected large amounts of SO_2 gas into the stratosphere, where it was subsequently converted into sulfate (SO_4) aerosol. In Section 4.8 we discuss the impact of these large eruptions on the assimilation in more detail.

Table 4.1 compares the global, area-weighted annual mean MERRA-2 AOD to our previous aerosol assimilation (MERRAero), and the AeroCom Phase II multi-model inter-comparison (Kinne et al., 2006). In general, MERRA-2 and MERRAero AOD are comparable given the differences in the aerosol emissions inventories, driving meteorology (i.e. MERRA-2 vs. MERRA meteorological reanalyses, respectively), and the AOD observing system (e.g. MERRAero assimilates MODIS NNR AOD only). Notably, sea salt AOD is generally higher in MERRA-2 compared to the other estimates, and carbonaceous aerosol AOD is higher than in Kinne et al. (2006). This latter difference is most likely due to the MERRA-2 use of QFED-scaled MODIS FRP-based biomass burning emissions (Darmenov and da Silva, 2015) relative to the GFED emissions used by most AeroCom models. AOD in dusty regions is slightly higher in MERRA-2 compared to MERRAero due to the inclusion of MISR in the MERRA-2 observing system over desert dust source regions.

Appendix B shows the time series of monthly-mean AOD from MERRA-2 and MERRAero for multiple regions around the globe. The MERRA-2 sea salt AOD is higher than in MERRAero, even over land regions (see Section 4.7). This has consequences for the surface mass comparisons discussed in Sections 4.6 and 4.7. Other noticeable regional differences include increased dust AOD in MERRA-2, which now also includes assimilation of MISR AOD over bright desert dust source regions. Finally, there are differences in the carbonaceous AOD during the period 2002 to 2010, where MERRA-2 used monthly-mean QFED emissions and MERRAero used daily QFED emissions. Figure 4.2 shows the boreal summer and wintertime climatological mean AOD from MERRA-2. Appendix C shows similar plots for other seasons, as well as climatological AOD contributions from the various aerosol species. Appendix C also shows the climatological global mean seasonal cycle of AOD for each aerosol type for the pre- and post-EOS periods.

4.3 Validation with independent observations of AOD

The MERRA-2 aerosol assimilation incorporates many of the available global measurements of AOD into the observing system described in Section 3.2. Here we validate the assimilated AOD with available independent observations. While certainly not an exhaustive validation, the comparisons

Table 4.1: Global, annual average 550 nm AOD by species.

Species	MERRA-2[a]	MERRAero[b]	AeroCom Phase II[c]
Dust	0.030 ± 0.010	0.026 ± 0.009	0.032 (0.012 - 0.054)
Sea Salt	0.041 ± 0.002	0.034 ± 0.002	0.030 (0.020 - 0.067)
Black Carbon	0.0056 ± 0.001	0.0060 ± 0.001	0.004 (0.0017 - 0.0088)
Organic Carbon	0.022 ± 0.007	0.025 ± 0.007	0.019 (0.006 - 0.030)
Sulfate	0.040 ± 0.004	0.039 ± 0.004	0.034 (0.015 - 0.051)
Total	0.138 ± 0.013	0.130 ± 0.015	0.127 (0.065 - 0.149)

[a] Global, annual average $\pm$ standard deviation calculated from monthly-mean AOD for the period 2003 – 2013.

[b] Global, annual average $\pm$ standard deviation calculated from monthly-mean AOD for the period 2003 – 2013 (Buchard et al., 2015).

[c] From Kinne et al. (2006) Table 4 for 15 AeroCom II models (median and range) with harmonized emissions for Y2000 (Dentener, 2006).
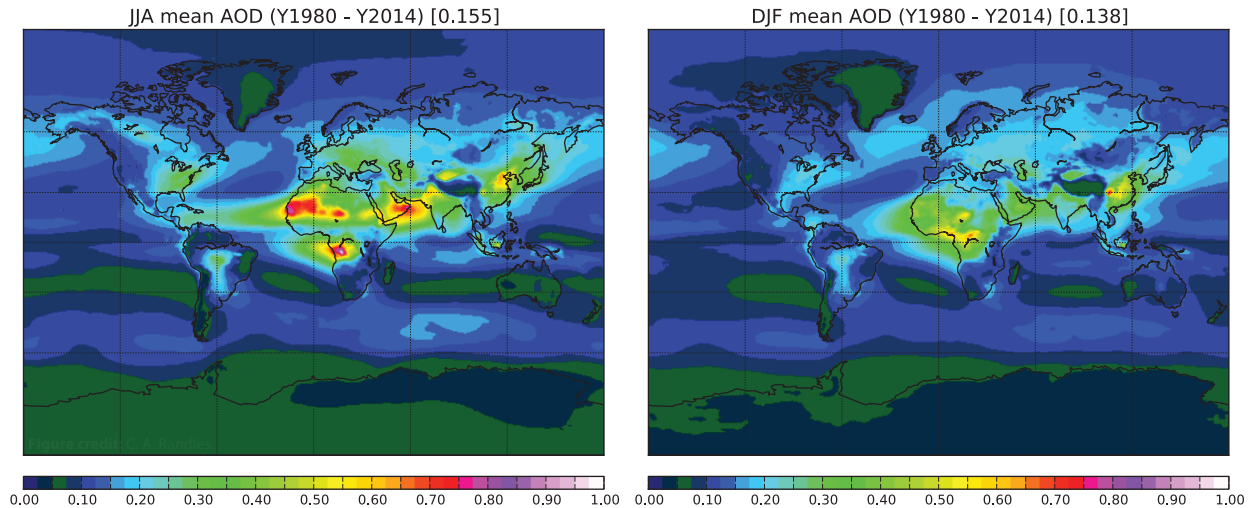
Figure 4.2: Spatial distribution of AOD in June-July-August (left) and December-January-February (right) averaged for the period 1980-2014. Similar figures for other seasons and for individual aerosol components are found in Appendix C.

presented here generally indicate a high degree of correlation and low degree of bias between the assimilation and independent observations.

- **Historical Shipborne Sun Photometers:** We use historical shipborne sun photometer data to validate MERRA-2 AOD prior to the EOS-period. These data, summarized in Smirnov et al. (2002) and partially used by Liu et al. (2004) for AVHRR validation, span the timeframe 1982-1996 and cover the cruises shown in Figure 4.3a. We compare the co-sampled MERRA-2 AOD at the observed wavelength closest to 500 nm (range 499 - 517 nm depending on the cruise). The observed AOD accuracy should be considered $\pm$ 0.02. Observations are reported as morning or afternoon averages. The model is sampled every three hours for a given observation date and then averaged over the periods from 9 am - noon or noon to 3 pm local time for purposes of comparison. Figure 4.3b shows a scatter plot of the AOD comparison, with statistics reported by year and geographical region. The correlation between MERRA-2 and the observations is best near dust-influenced regions (e.g. the Red Sea, Mediterranean, and near North Africa). In the remote Pacific, MERRA-2 AOD is not well-correlated with the observations, but the bias is low. Importantly, the observations indicate that MERRA-2 AOD is biased high after the Pinatubo eruption (1991). We will discuss reasons for this in Section 4.8.

- **MAN:** The Maritime Aerosol Network (MAN), a subsidiary of AERONET, employs Microtops II sun photometers aboard ships of opportunity to measure AOD (`http://aeronet.gsfc.nasa.gov/new_web/maritime_aerosol_network.html`). The photometers used in MAN are calibrated to have an estimated uncertainty in AOD of $\pm$ 0.02 (Smirnov et al., 2009). MAN cruises cover the period 2004-present. These observations have not been assimilated in the MERRA-2 GAAS and therefore serve as independent validation of the assimilated AOD product. Figure 4.4 compares all available MAN observations with co-located MERRA-2 AOD. A high degree of correlation is found between the MERRA-2 and MAN observations, and the bias is generally low, though MERRA-2 does tend to slightly overestimate the lowest observed AOD. (**N.B.** Figure 4.4 is presented on a log-log scale).

- **DIAL/HSRL:** The NASA Langley Research Center (LaRC) DIfferential Absorption Lidar (DIAL) system implements the High Spectral Resolution Lidar (HSRL) technique to retrieve aerosol extinction and AOD at 532 nm (Hair et al., 2008). The instrument also retrieves aerosol backscatter coefficients and is sensitive to polarization at three wavelengths (355, 532, and 1064 nm), measuring both above and below the aircraft (i.e. zenith and nadir).
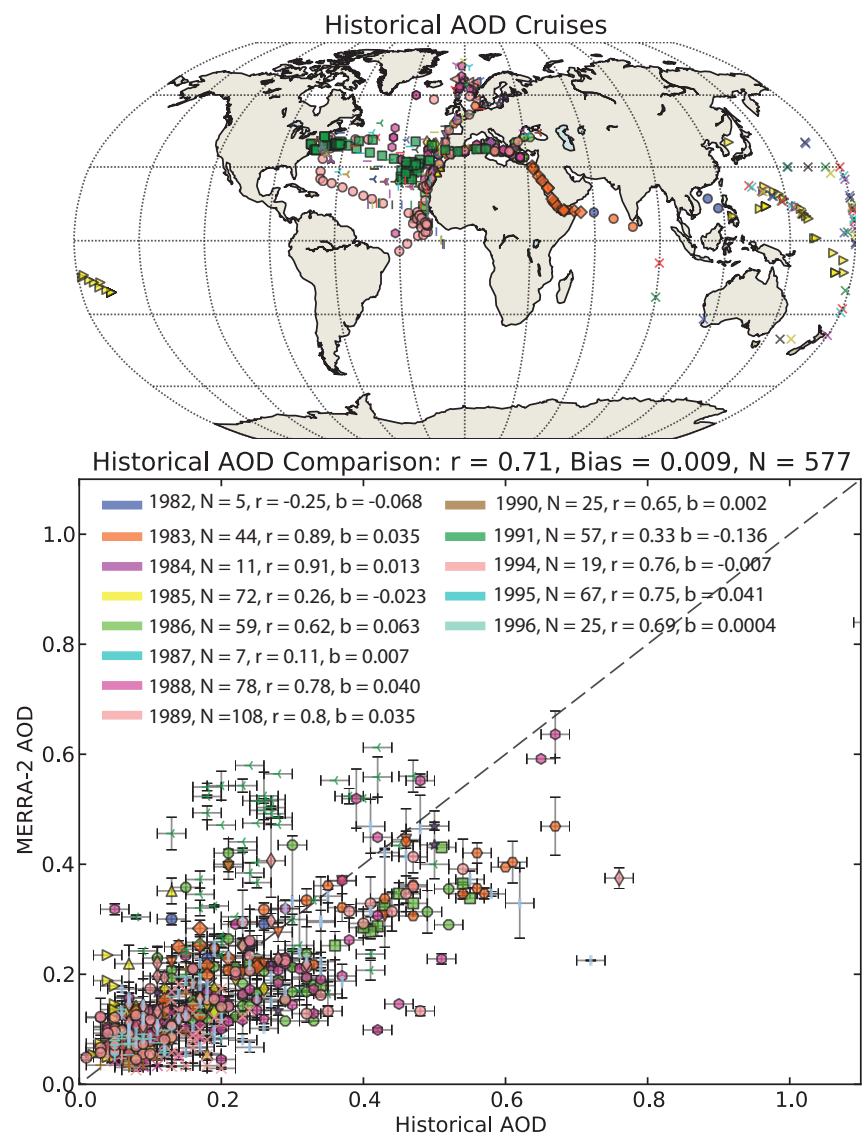
Figure 4.3: Comparison of MERRA-2 and historical shipborne AOD observations. (a) Map showing the location of the ship cruises spanning the period 1982 – 1996. (b) Scatter plot of AOD spanning various years (indicated by different colors) and different cruises (indicated by marker shape). X-axis error bars represent the assumed observed AOD error of 0.02, and y-axis error bars are the standard deviation of the MERRA-2 AOD used to make the morning or afternoon averages.
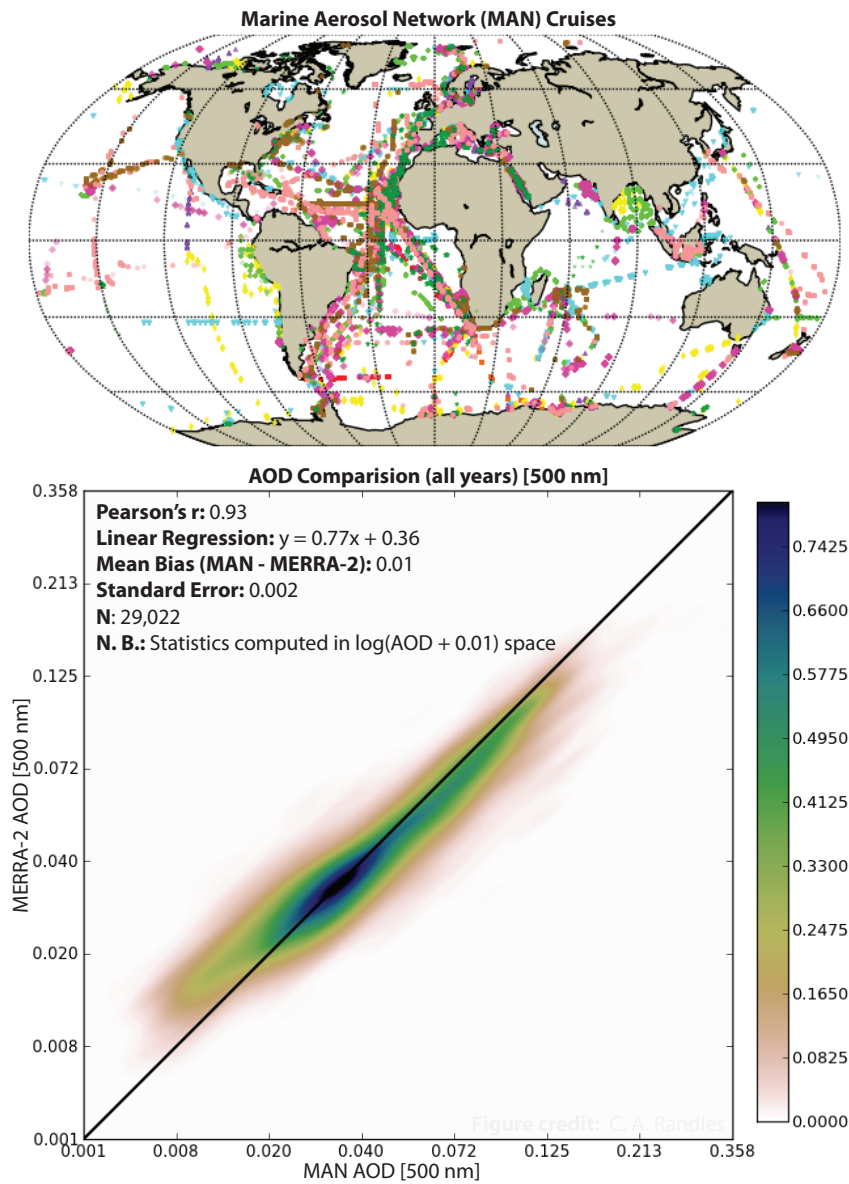
Figure 4.4: (a) Maritime Aerosol Network (MAN) cruises 2004-present, color coded by year. (b) Joint PDF comparison of MAN-observed AOD and MERRA-2 AOD for the same period.
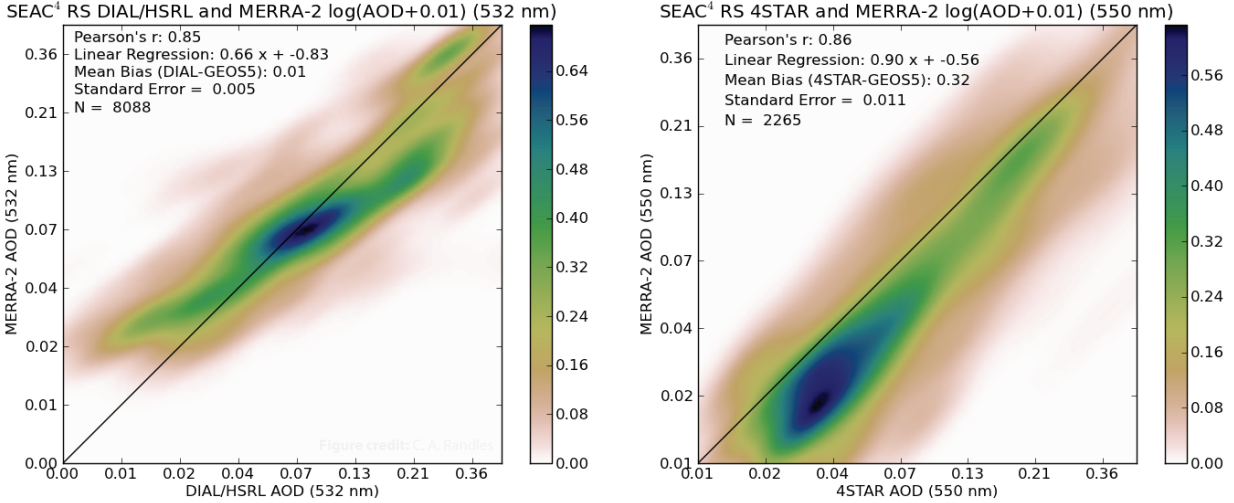
Figure 4.5: Comparisons of AOD observed during the NASA SEAC[4]RS campaign (August - September 2013) and MERRA-2. (a, left) 532 nm AOD observed by the DIAL/HSRL instrument aboard the NASA DC8 for the entire campaign compared to MERRA-2 AOD sampled along the flight paths and over the same portion of the column as reported by the instrument. (b, right) 550 nm AOD observed by the 4STAR instrument aboard the DC8 and MERRA-2 AOD sampled along the flight paths and for the portion of the column above the aircraft altitude. Note that the x -and y-axis labels are in units of AOD but the statistics reported are in log-space.

AOD are derived from nadir aerosol extinction profiles when the aircraft is above 6 km; a 1 km region below the aircraft is omitted from the AOD column as the laser and telescope are not fully aligned in this region. During the NASA Studies of Emissions and Atmospheric Composition, Clouds, and Climate Coupling by Regional Surveys (SEAC[4]RS) campaign from August to September 2013 (http://www.nasa.gov/mission_pages/seac4rs), the DIAL/HSRL system aboard the NASA DC8 aircraft measured AOD over a large portion of the southeastern and western continental United States, including several smoke plumes from large fires (e.g. the Rim Fire). We sample MERRA-2 along the aircraft trajectories for the entire SEAC[4]RS campaign and calculate the AOD over the same portion of the column as the observations. Figure 4.5a shows the performance of the MERRA-2 aerosol relative to these independent observations in logarithmic space. There is a high degree of correlation and low bias between MERRA-2 and AOD measured by the DIAL/HSRL system. Further note that the statistics reported in Figure 4.5a are in logarithmic space; in linear space the Pearson's correlation coefficient and bias (DIAL/HSRL - MERRA-2) are 0.74 and 0.02, respectively.

- **4STAR** The Spectrometer for Sky-Scanning, Sun-Tracking Atmospheric Research (4STAR) instrument combines airborne sun tracking and sky scanning with diffraction spectroscopy for

41

direct-beam hyper-spectral measurement of aerosol optical depth above the aircraft (Duna-
gan et al., 2013). 4STAR's hyper-spectral measurement of the direct solar beam improves
retrievals of gas constituents (e.g. H_2O, O_3, and NO_2, Segal-Rosenheimer et al., 2014) and
therefore improves determination of aerosol properties (e.g. AOD) as residuals of the to-
tal optical depth. 4STAR has been shown to compare well with HSRL-2 (Shinozuka et al.,
2013). During SEAC[4]RS, AOD was reported for 15 channels (355, 380, 452, 501, 520, 532,
550, 606, 675, 781, 865, 1020, 1064, 1236, and 1559 nm). Additionally, during this campaign
ambient temperature varied more widely than in 4STAR's previous deployments, and the
measurements exhibited a systematic high bias in AOD. An empirical correction was applied
to improve the accuracy of reported AOD, but it also disproportionally eliminated AODs
under conditions of low aerosol burden or high altitude. Estimated measurement uncertainty
in AOD was determined to be $\pm$ 0.02 for SEAC[4]RS. In Figure 4.5b we compare the along-
track and above aircraft altitude 550 nm AOD from MERRA-2 and 4STAR for the entire
campaign. The assimilation results and independent observations are again highly correlated,
but MERRA-2 shows a low bias. The assimilation tends to underestimate the above-aircraft
AOD when the aircraft is at higher altitudes (e.g. above 8 km) or in the vicinity of a very
strong biomass burning source (e.g. the Rim Fire; not shown). Recall that the assimilation
does not constrain the vertical distribution of aerosols, and unlike the total column AOD, the
AOD calculated above the aircraft is sensitive to this vertical distribution of aerosols. Again
note that the statistics reported in Figure 4.5 are in logarithmic space; in linear space the
Pearson's correlation coefficient and bias (4STAR - MERRA-2) are 0.78 and 0.03, respectively.

4.4   AI and AAOD

The Ozone Monitoring Instrument (OMI) aboard the NASA EOS Aura spacecraft (July 2002-
present) measures scattered sunlight in the 270 to 500 nm wavelength range with a footprint
ranging from 13 km $\times$ 24 km at nadir to 28 km $\times$ 150 km along the edges. Using the OMAERUV
algorithm, the near-ultra-violet (UV) Aerosol Index (AI) is derived following Torres et al. (2007). AI
is a qualitative parameter useful for detecting the presence of absorbing aerosols in the atmosphere
based on a spectral contrast method in the near-UV region where ozone absorption is very small
(Herman et al., 1997; Torres et al., 1998, 2007). In addition, the OMAERUV algorithm uses OMI-
reflectances at 354 and 388 nm to derive AOD and AAOD at 388 nm using pre-computed top-of-the
atmosphere (TOA) aerosol reflectance look-up tables (LUTs) based on 21 aerosol models. The UV

AI is well-known to be sensitive to aerosol concentration, aerosol optical properties, and aerosol layer height (de Graaf and Stammes, 2005; Herman et al., 1997; Hsu et al., 1999; Torres et al., 1998).

Buchard et al. (2015) developed a radiative transfer interface using the Vector LInearized Discrete Ordinate Radiative Transfer (VLIDORT) radiative transfer code (Spurr, 2006) to simulate the UV AI from GEOS-5 aerosol fields. Simulated UV AI can then be compared to retrievals from the OMI instrument. The simulated AI is computed as:

$$AI = -100 \times \log_{10} \frac{I_{354}^{Model}}{I_{354}^{cRayleigh}(R_{388*}^{Model})} \tag{4.1}$$

where I_{354}^{Model} is the VLIDORT-calculated TOA radiance at 354 nm using MERRA-2 aerosol concentrations; $I_{354}^{cRayleigh}$ is the TOA radiance at 354 nm without aerosols assuming the Lambertian Equivalent Reflectivity (LER) at 388 nm (R_{388*}^{Model}). Additional details on the calculation of AI using the VLIDORT simulator can be found in Buchard et al. (2015).

MERRA-2 includes assimilation of AOD from various ground- and satellite-based sensors. Notably, in constraining the AOD, the assimilation does not directly constrain the AAOD or AI. We therefore can consider a comparison of these aerosol properties to observations as independent validation points for MERRA-2. Figure 4.6 compares the monthly mean OMI UV AI and AAOD to the MERRA-2 AI and AAOD in July 2007. Differences between OMI and MERRA-2 are also shown. As in Buchard et al. (2015), in the comparison we use a research version of the Level 2 OMAERUV aerosol data products (Torres et al., 2013). Globally, MERRA-2 well simulates the AI compared to OMI. Compared to Buchard et al. (2015), there is improved agreement with dust AI over desert regions because MERRA-2 uses the improved dust optics tables developed in that study. The worst agreement between OMI AI and that simulated from MERRA-2 occurs in the biomass burning region of southern Africa. A similar discrepancy was seen in Buchard et al. (2015) and attributed to the assumed spectral dependence of organic carbon near-UV absorption in the model (i.e. the model does not simulate so-called brown carbon that is much more absorbing in the near-UV). The 388 nm AAOD shows good agreement with OMI, and is improved compared to the MERRAero aerosol reanalysis evaluated in Buchard et al. (2015), particularly in parts of Asia such as over the Indo-Gangetic plain in India.
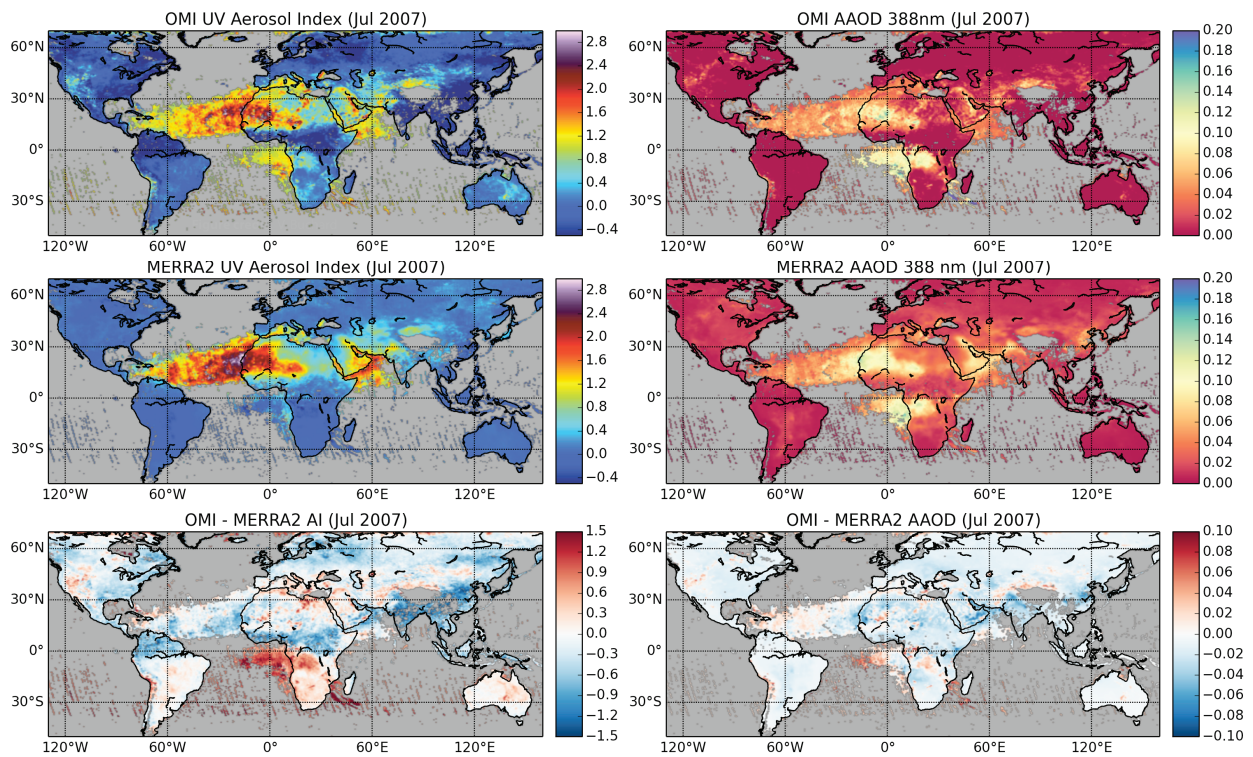
Figure 4.6: Monthly mean UV AI (left column) and AAOD (right column) at 388 nm from OMI (top row) and simulated from MERRA-2 (middle row) in July 2007. Difference plots (OMI - MERRA-2) are on the bottom row. MERRA-2 AI is simulated as described in Buchard et al. (2015).

4.5 Vertical distribution of aerosols

4.5.1 Zonal mean aerosol mass mixing ratios

Figure 4.7 shows the climatological annual, zonal mean distribution of the five different aerosol types. In the following subsections, we validate the vertical distribution of the assimilated aerosols with available vertically-resolved aerosol optical properties and mass. Again, this comparison is not exhaustive but does illustrate where the MERRA-2 aerosol assimilation performs well and where it may have deficiencies.

4.5.2 Comparisons to CALIPSO observations

Since 2006, the Cloud Aerosol Lidar with Orthogonal Polarization (CALIOP) instrument aboard the NASA A-Train CALIPSO satellite (Winker et al., 2007,0) has provided important global information about aerosol vertical structure. Here we evaluate the vertical structure of attenuated backscatter from MERRA-2 sampled along the CALIOP path. As in Buchard et al. (2016), we use CALIPSO version 3.01 Level 1B attenuated backscatter. This product has been cloud-cleared using the Level 2 vertical feature mask and then averaged to a uniform resolution of 20 km horizontally and 60 m vertically. There are at most 120 full resolution samples (i.e. single shot ∼3 km horizontal × 30 m vertical resolution) averaged per lidar range bin. Note that the attenuated backscatter coefficient here includes the Rayleigh contribution. While CALIOP derived extinction profiles are available, these retrievals rely on assumptions about the extinction-to-backscatter ratio which may or may not be consistent with the aerosol optical properties assumed in MERRA-2. The computation of the aerosol-only contribution is straightforward in MERRA-2, but removal of the Rayleigh contribution from the CALIOP attenuated backscatter data often can lead to error sources (Buchard et al., 2016). For these reasons, we restrict our analysis to the total (aerosol plus molecular) attenuated backscatter coefficient.

Figure 4.8 compares day and night profiles from CALIOP and MERRA-2 averaged over the dust transport region from northern Africa to the North Atlantic, biomass burning regions of southern Africa and the Amazon, and over the continental United States. Generally, MERRA-2 well represents the CALIOP attenuated backscatter profiles over these important aerosol source regions, though the near-surface attenuated backscatter is underestimated in northern and southern Africa.
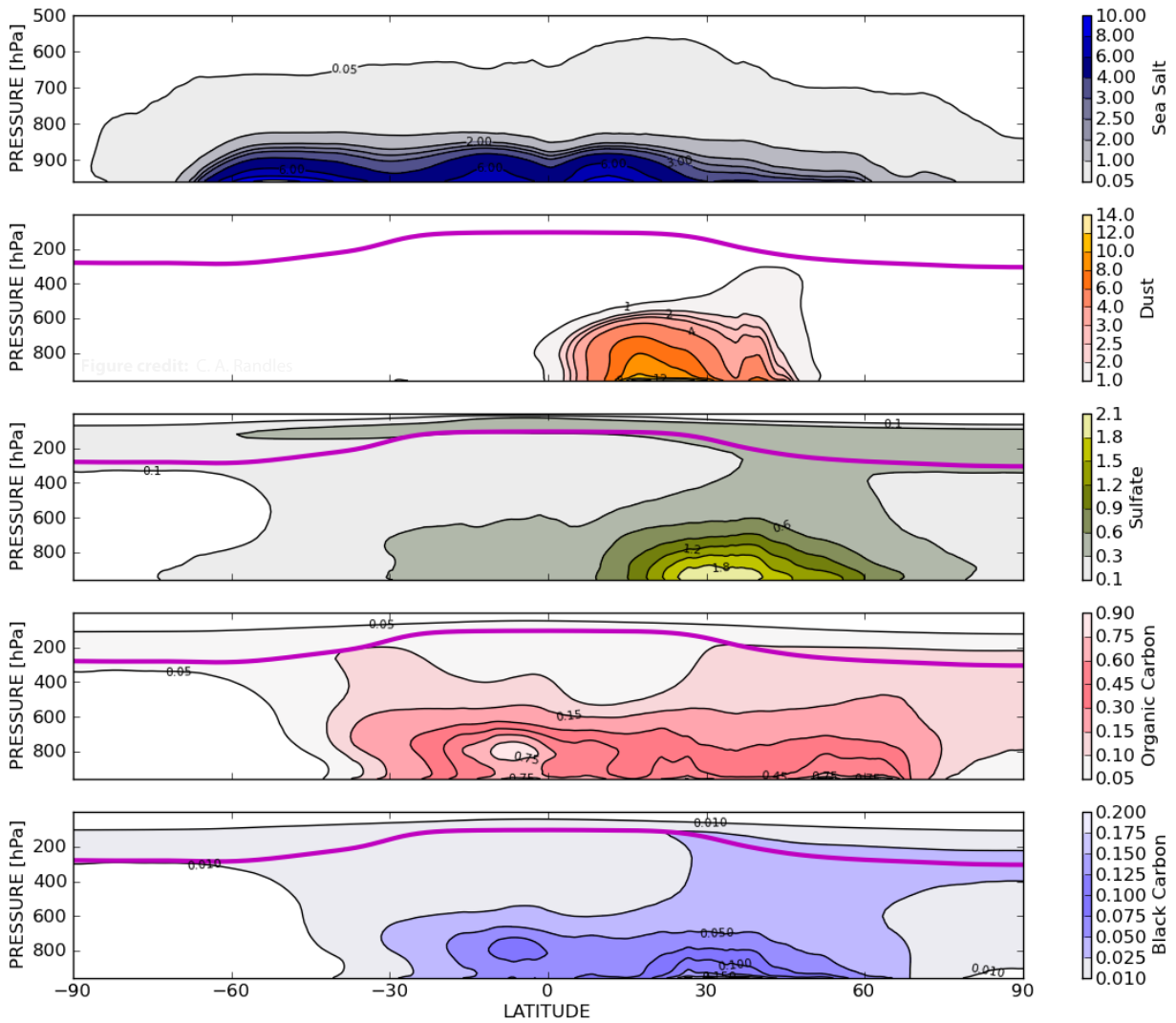
Figure 4.7: Zonal, annual mean aerosol mass mixing ratios [ng kg^{-1}] averaged over the period 2003-2014 for, from top to bottom, sea salt, dust, sulfate, organic carbon, and black carbon. The thick magenta line is the zonal mean tropopause height.

46

This underestimate is due to underestimated backscatter from sea-salt aerosol over the ocean (not shown).

4.5.3 Comparisons to aircraft observations

Airborne LIDAR: Using the HSRL technique, the first-generation NASA Langley Research Center (LaRC) airborne HSRL-1 system measures aerosol extinction, backscatter, and depolarization at 532 nm without requiring additional aerosol measurements or assumptions about aerosol type. HSRL-1 was deployed during the NASA Deriving Information on Surface Conditions from COlumn and VERtically Resolved Observations Relevant to Air Quality (DISCOVER-AQ) (`https://www.nasa.gov/mission_pages/discover-aq/`) deployment over the Baltimore, Maryland and Washington D.C. region in July 2011. In addition to implementing the HSRL technique at 532 nm, the second-generation HSRL-2 instrument also implements the technique at 355 nm enabling independent, unambiguous retrievals of aerosol extinction and backscatter at both wavelengths. It also uses standard backscatter technique at 1064 nm and has sensitivity to polarization at all three wavelengths. HSRL-2 provides profile measurements of extinction and optical thickness at 355 and 532 nm and profile measurements of backscatter and depolarization at all three wavelengths (Muller et al., 2014). HSRL-2 was deployed during the San Joaquin Valley, California (January - February, 2013) and Houston, Texas (September 2013) phases of the NASA DISCOVER-AQ campaign. Finally, the previously described DIAL/HSRL instrument was deployed during the SEAC[4]RS campaign in August-September, 2013. All three different instruments share similar measurement techniques and analysis algorithms.

Figure 4.9 compares the campaign-median extinction and backscatter profiles from the various phases of the DISCOVER-AQ and SEAC[4]RS campaigns to co-sampled profiles simulated in MERRA-2. In general, given the variability of the profiles encountered (shading) and the model resolution, MERRA-2 well-represents the observed vertical profiles of extinction and backscatter over the continental United States. The one exception is over the San Joaquin Valley region of California (bottom row, Fig. 4.9). Here the model profile does not show the strong increase in aerosol optical properties near the surface; this is likely due to the representation of the PBL in MERRA-2 and the lack of nitrate aerosols in the GEOS-5/GOCART system (Buchard et al., 2016).

Black Carbon Mass Mixing Ratio: The airborne Single Particle Soot Absorption Photometer
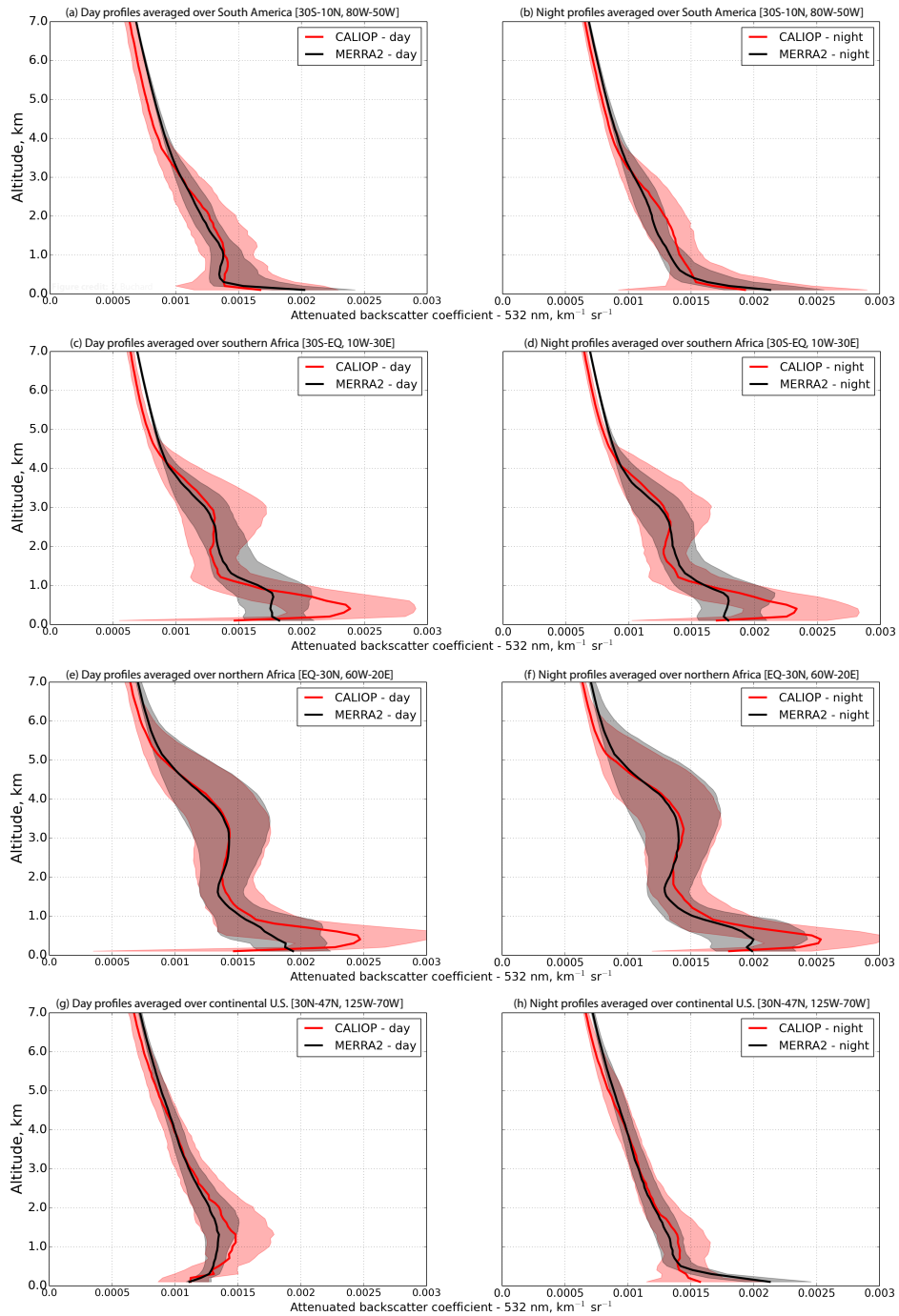
Figure 4.8: Seasonal (JJA, 2008) vertical profiles of attenuated backscatter coefficient $[\text{km}^{-1}\ \text{sr}^{-1}]$ at 532 nm from CALIOP and derived from MERRA-2 simulations sampled on the CALIOP path averaged over (a-b) South America, (c-d) southern Africa, (e-f) northern Africa, and (g-h) the continental United States for all day profiles (left column) and night profiles (right column). Solid lines are the median of all profiles, and shading represents the 25% to 75% percentile of all modeled and observed profiles. Similar plots over the continental US for the previous aerosol assimilation, MERRAero, are found in Buchard et al. (2016), and comparisons in north Africa can be seen in Buchard et al. (2015). Note that the attenuated backscatter shown here includes contributions from both Rayleigh and aerosol scattering.
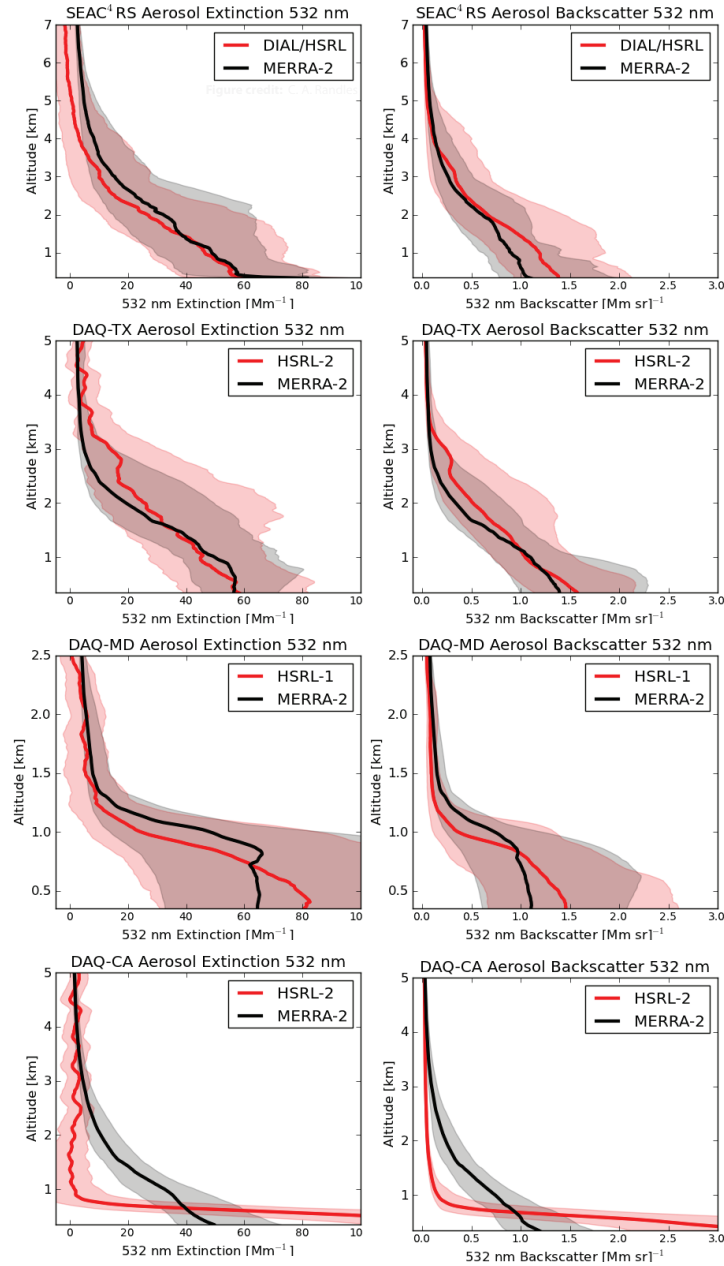
Figure 4.9: Vertical profiles of extinction coefficient (Mm^{-1}; left column) and aerosol backscatter ($Mm^{-1}\,sr^{-1}$; right column) at 532 nm measured by HSRL instruments and derived from MERRA-2 sampled on the HSRL flight path during US aircraft-based field campaign: SEAC[4]RS (top row; August-September 2013; western and southeastern US), DISCOVER-AQ TX (second row; September, 2013; Houston, Texas), DISCOVER-AQ MD (third row; Baltimore-Washington DC; July 2011), and DISCOVER-AQ CA (bottom row; San Joaquin Valley, California; January-February 2013). The solid red and black lines are the median for HSRL and MERRA-2, respectively. Shaded areas represent between the 25% and 75% percentiles of all modeled and observed profiles. Similar plots for the previous aerosol assimilation, MERRAero, are found in Buchard et al. (2016).

(SP2) (Schwarz et al., 2006; Slowik et al., 2007) instrument uses an intense laser to heat the refractory component of individual aerosol particles to vaporization. The refractory black carbon (rBC) mass of each particle is determined from the detected thermal radiation (Schwarz et al., 2006), independent of particle morphology and mixing state (Cross et al., 2010). SP2 observed rBC is interchangeable with the BC defined in model parameterizations and aerosol emission inventories (Dentener, 2006; Schwarz et al., 2010). The mass-mixing ratio of black carbon in the atmosphere along the flight track can be obtained by aggregating the observed particles over short time intervals (1 second - 1 minute; Schwarz et al., 2010). Unlike optical measurements of black carbon mass, comparing SP2 measured rBC to model-derived black carbon mass mixing ratio is not sensitive to assumptions about black carbon optical properties.

The NOAA High-performance Instrumented Airborne Platform for Environmental Research Pole-to-Pole Observations of Carbon Cycle and Greenhouse Gases Study (HIPPO; Wofsy et al., 2011) provides vertically resolved rBC mass over the remote Pacific ocean. The HIPPO aircraft campaign is unique in that it provides consistently collected observations of rBC mass vertical distribution at most latitudes spanning several seasons and years. Each of the five HIPPO phases consist of a meridional transect over the Pacific, with occasional detours to nearby continental regions. Regular ascents and descents were made along the track providing vertically resolved measurements from about 200 m to 8.5 km (and occasionally 14 km) above sea level. Averaged vertical profiles of rBC from HIPPO-1 data were compared to monthly mean results from 14 global models participating in the AeroCom project. The model ensemble spread was over an order of magnitude, and models typically overestimated black carbon concentrations by a factor of 5, with the highest biases in the tropical upper troposphere (Schwarz et al., 2010). Flight paths of the various HIPPO campaigns can be seen in Figure 1 of Schwarz et al. (2013).

The comparisons of vertically-resolved black carbon mass from MERRA-2 with observations from SP2 paint a mixed picture of model performance. Figure 4.10 compares the co-sampled MERRA-2 black carbon mass mixing ratio to observations from the HIPPO 1-5 campaigns for different latitude bands. In all cases MERRA-2 is biased high relative to the observations in the remote locations sampled during the HIPPO campaigns. Notably, though, this high bias tends to be smaller in the Northern Hemisphere high latitudes. In contrast, at higher latitudes MERRA-2 tends to underestimate the SP2 observations during the Arctic Research of the Composition of the Troposphere from Aircraft and Satellites (ARCTAS)-A campaign (Fig. 4.11a), when large springtime Siberian fires impacted the observed black carbon concentrations over northern Alaska
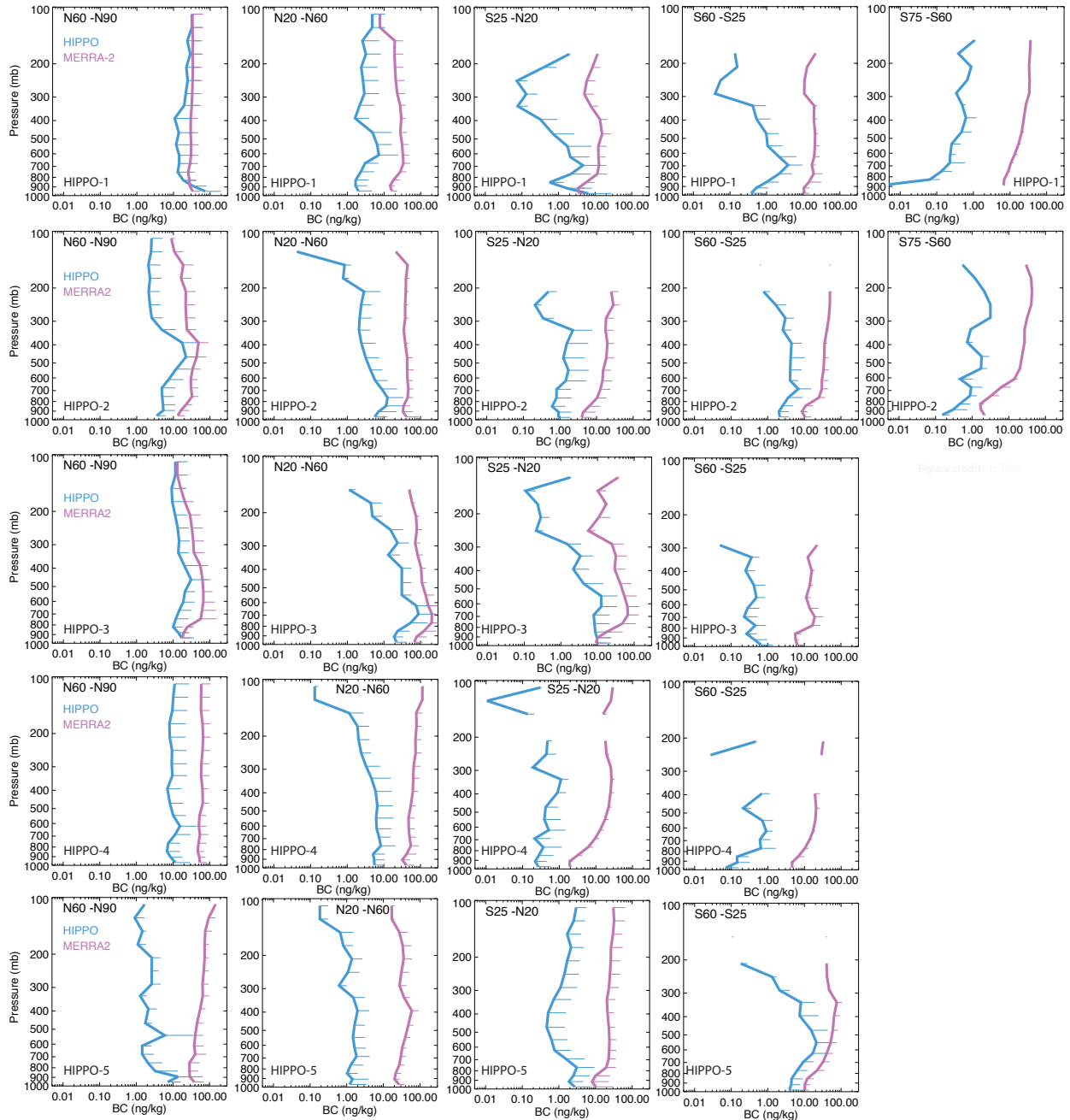
Figure 4.10: Comparison of MERRA-2 black carbon mass mixing ratio [ng kg^{-1}] to observations from the SP2 instrument zonally averaged over bands from north to south (left to right) for the five HIPPO campaigns (top to bottom). See Schwarz et al. (2013) for a map of the HIPPO flight paths.
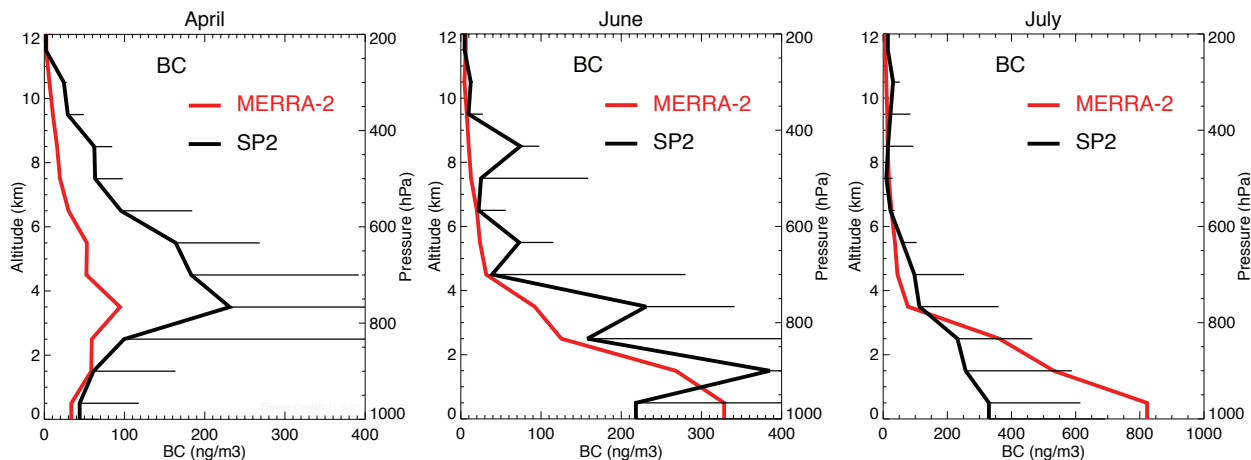
Figure 4.11: Comparison of MERRA-2 black carbon mass concentration [ng m^{-3}] to observations from the SP2 instrument during the (a) ARCTAS-A campaign (Fairbanks, Alaska; 3-19 April 2008), (b) the ARCTAS-CARB campaign (Palmdale, CA; 18-24 June, 2008), and (c) the ARCTAS-B campaign (Cold Lake, Alberta, Canada; 29 June -13 July, 2008).

(Jacob et al., 2010). Where northern California fires impacted the amount of black carbon observed during the ARCTAS-CARB campaign (Fig. 4.11b), MERRA-2 shows reasonable agreement with the observations. Finally in July over central Canada during ARCTAS-B, MERRA-2 tends to overestimate black carbon mass below about 3 km, though it is generally within the variability of the observations (Fig. 4.11c). This overestimate is similar to the results of Bian et al. (2013) who compared the GEOS-5 forecasted AOD to ARCTAS observations. Overall, the ARCTAS comparisons reveal that closer to sources the black carbon vertical distribution is somewhat reasonable. In contrast, the HIPPO comparisons show that the largest discrepancies exist over the remote ocean where MERRA-2 black carbon mass is generally too high throughout the column, and especially in the free troposphere. Global models including GOCART typically overestimate black carbon in these regions (Schwarz et al., 2010), and positive AOD increments can exacerbate the bias in the assimilation.

4.6 Surface aerosol mass

Fine surface particulates near the surface with diameters less than 2.5 μm (PM$_{2.5}$) negatively impact both air quality and human health (e.g. Pope and Dockery, 110; Pope III et al., 2009). Air quality monitoring networks exist in various regions over the globe, but they offer sparse geographical and temporal coverage. There exists a desire for some in the air quality scientific community to use data

assimilation systems as an integrator of observations and models to provide better spatio-temporal forecasts of $PM_{2.5}$. Here we examine the surface aerosol concentrations over the continental US as in Buchard et al. (2016), and we also compare surface SO_2 and sulfate to observations over East Asia.

$PM_{2.5}$ over the United States: The US Environmental Protection Agency (EPA) uses 24-hour surface filters to measure $PM_{2.5}$ and surface aerosol speciation as part of their Air Quality System (AQS) and Chemical Speciation Network (CSN) networks, respectively, both of which tend to be located in suburban or urban locations primarily in the eastern part of the US (Buchard et al., 2016; Malm et al., 2011, 1994). The National Park Service's Interagency Monitoring of Protected Visual Environments (IMPROVE) network has 150 stations in mostly remote or rural locations that measure speciated $PM_{2.5}$ and reconstruct total $PM_{2.5}$ through Reconstructed Fine Mass (RCFM) (Hand et al., 2011; Malm et al., 1994). Additional details on the AQS, CSN, and IMPROVE networks and how they are compared to the MERRAero aerosol reanalysis are found in Buchard et al. (2016).

Figure 4.12 compares the monthly-mean MERRA-2 $PM_{2.5}$ to observations from the AQS and IMPROVE networks over several regions of the United States for the period 2003 to 2012. Overall, MERRA-2 $PM_{2.5}$ compares to observations similarly well as MERRAero, except MERRA-2 $PM_{2.5}$ is higher than MERRAero in the eastern US, particularly in summer. The model biases in Figure 4.12 are largely explained in Buchard et al. (2016). Briefly, better agreement between the assimilation and observations is found for the rurally-located IMPROVE stations, and the largest model biases are found in the winter time compared to EPA stations.

Figure 4.13 shows the monthly-mean variation of surface $PM_{2.5}$ divided into different aerosol species for the northwestern and northeastern US, similar to Buchard et al. (2016, their Fig. 5). The comparison of MERRA-2 ammonium sulfate, black carbon, and organic carbon to the observations is similar to the results for MERRAero described in Buchard et al. (2016). For the mostly suburban and urban AQS sites, the underestimate in winter in both the northeastern and northwestern US (Fig. 4.12) is due to an underestimation of POM and a lack of nitrate aerosols. Unlike MERRAero, Figure 4.13 shows a larger overestimation of dust and especially sea salt for both networks. The excessive surface sea salt will be discussed further in Section 4.7.

Surface sulfur over Asia: The Acid Deposition Monitoring Network in East Asia (EANET)
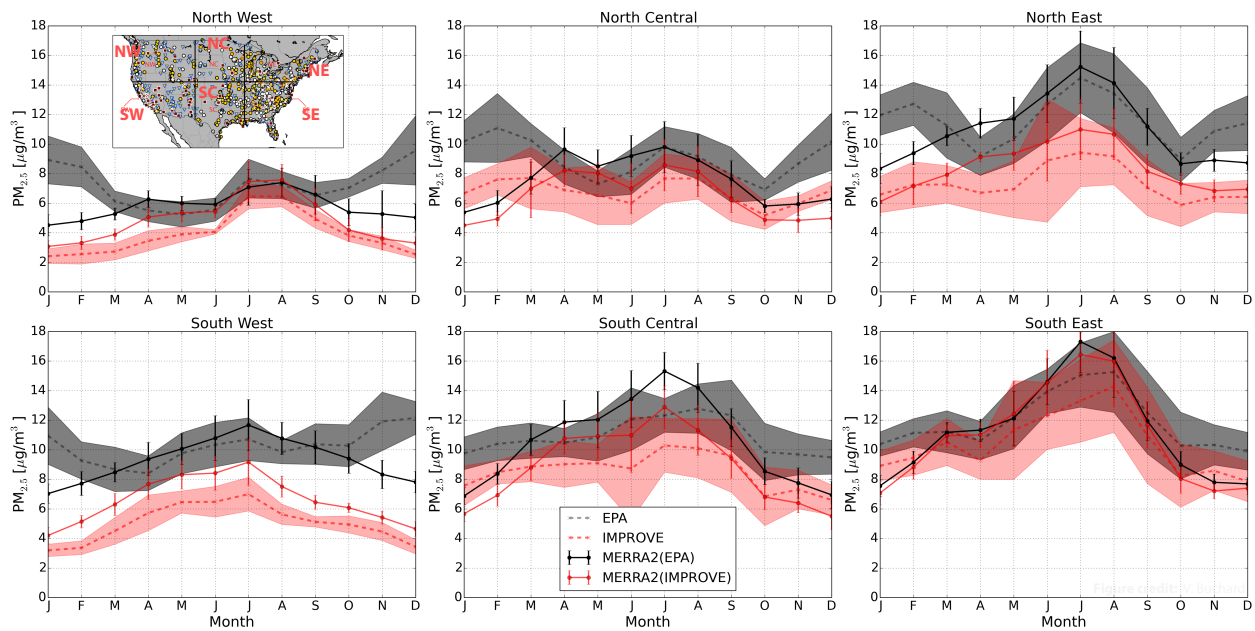
Figure 4.12: Monthly and regional variations of surface PM$_{2.5}$ [μg m^{-3}] from both the EPA-AQS (grey dashed-line) and IMPROVE (red dashed-line) networks compared to MERRA-2 sampled at AQS sites (black continuous-line) and IMPROVE sites (red continuous-line) located in the northwestern (NW), north-central (NC), northeastern (NE), southwestern (SW), south-central (SC), and southeastern (SE) US for the period 2003 to 2012. Vertical bars are the standard deviations of the monthly values calculated from the years 2003-2012 in the model, and the shaded areas are the standard deviations over this periods for the observations. The inset map shows the geographical regions as well as the AQS sites (circles), CSN sites (crosses), and IMPROVE sites (triangles). Yellow symbols are in rural areas and white symbols are urban and suburban areas. A larger version of the inset map can be found in Buchard et al. (2016).
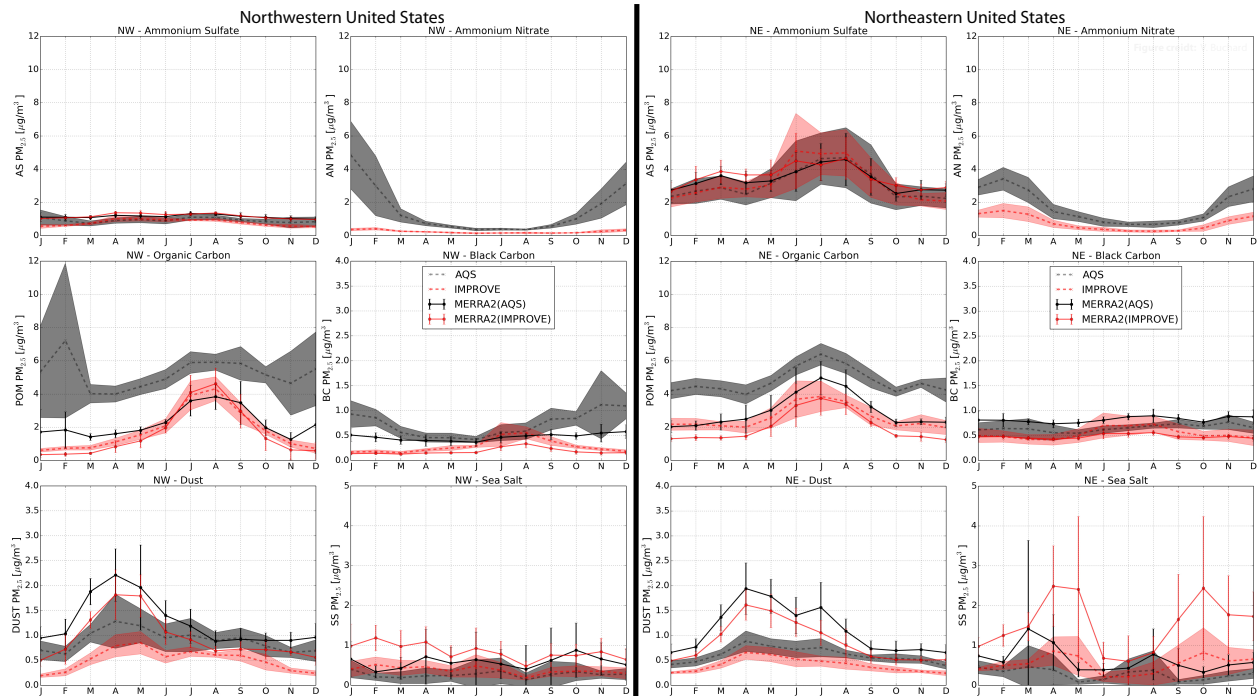
Figure 4.13: Monthly and regional variations of surface PM$_{2.5}$ [μg m^{-3}] for each species in the northwestern (NW) US (left two columns) and the northeastern (NE) US (right two columns). Species are (top row) ammonium sulfate (AS) and ammonium nitrate (AN), (middle row) POM and black carbon, and (bottom row) dust (DU) and sea salt (SS). The EPA-CSN and IMPROVE network observations are the grey and red dashed lines, respectively. MERRA-2 sampled at CSN and IMPROVE sites is shown by grey and red continuous lines, respectively. Vertical bars are the standard deviations of monthly values between 2003 and 2012 for the model, and the shaded regions are the standard deviations for the observations.

started in 1998 as an intergovernmental initiative to create a common understanding of the state of acid deposition problems in East Asia, to provide useful inputs for decision making at various levels with the aim of preventing or reducing adverse impacts on the environment, and to promote cooperation among countries. Thirteen countries in East Asia are participating in EANET at present. Details of the monitoring techniques, including sampling, chemical analysis, definitions of data completeness, and quality control and quality assurance are documented in the EANET monitoring manuals: EANET (2000a), EANET (2000b), EANET (2001), and EANET (2006).

We evaluate the monthly averaged surface SO_2 [ppb] and SO_4 [μg m^{-3}] surface concentration from MERRA-2 compared to EANET at 46 sites for the period of 2001 to 2008. Note that the observations are reported as monthly means, so the model has not been co-sampled at observation times (i.e. the MERRA-2 monthly mean includes all sub-monthly AODs). Figure 4.14 shows that for SO_4 surface concentrations at the EANET sites, there is good linear correlation considering all seasons ($r = 0.529$); however, MERRA-2 underestimates observed surface SO_4 in all seasons by about a factor of 2, particularly when observed SO_4 is greater than 1 μg m^{-3}. Relative biases (the ratio of MERRA-2 to EANET) range from 0.381 in winter to 0.457 in the fall. Figure 4.14 also shows that MERRA-2 overestimates SO_2 compared to EANET in all seasons except for the winter, with relative biases varying from 1.170 in the spring to 1.418 in the fall. MERRA-2 is biased low in the winter (B = 0.968), but the correlation is highest then ($r = 0.501$). Note that, unlike the sulfate aerosol which is constrained by both the meteorological and AOD assimilation, the sulfur dioxide gas concentration at the surface is determined by the imposed emission inventory (Section 2.2) and model meteorology (production and loss).

4.7   Dust transport and sea salt

Evaluation of MERRA-2 dust transport: Desert dust is one of the main contributors to the global aerosol burden (Textor et al., 2006) and it has a large impact on the Earth's radiative budget because it absorbs and scatters both solar and infrared radiation (Colarco et al., 2014b). Additionally, deposition of desert dust into the ocean is an important source of iron, and therefore dust deposition influences phytoplankton respiration (i.e. CO_2 uptake) and biosphere-climate interactions (Mahowald et al., 2009).

Here we compare the dust surface concentrations from MERRA-2 to the long-term observations at
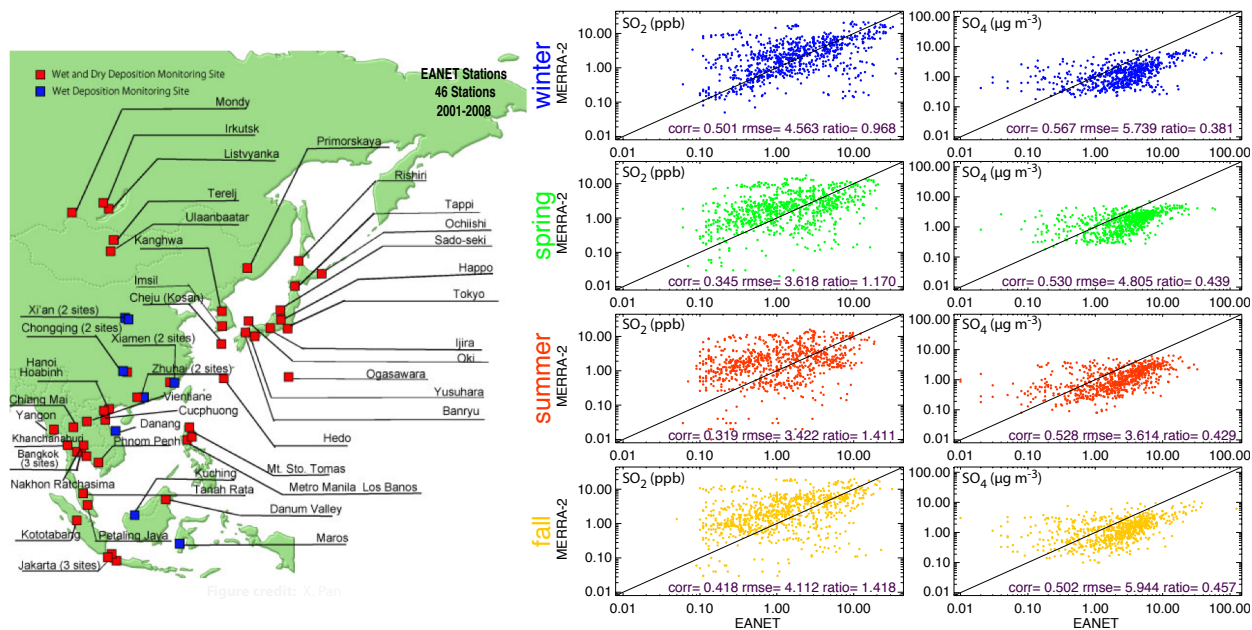
Figure 4.14: Comparison of surface concentration of SO_2 [ppb; left column] and sulfate aerosol [SO_4; μg m^{-3}; right column] between MERRA-2 and EANET at 46 sites (see map) between 2001 and 2008. Results are shown for boreal winter (top row), spring (second row), summer (third row), and fall (bottom row). $rmse$ is the root-mean-square error relative to EANET, r is the Pearson's correlation coefficient, and the relative bias ratio (B) is the $\sum$MERRA-2/$\sum$EANET.

Barbados (13.17°N, 59.53°W) and the University of Miami (25.75°N, 80.25°W) maintained by the Rosenstiel School of Marine and Atmospheric Science (RSMAS) (Prospero, 1996; Prospero et al., 1989). These sites are located far downwind of the dust emission sources over Africa. Measurements of Saharan dust particles over the Caribbean Sea have generally been reported as less than 10 μm in diameter (Reid et al., 2003), and the dust size bins assumed in MERRA-2 correspond to this size range.

Figure 4.15 shows a comparison of daily-mean dust surface concentration at Barbados from RSMAS observations, MERRA-2, and our first aerosol reanalysis (MERRAero) for 2006. The observations show a clear annual cycle in dust transport from northern Africa to the Caribbean, with a pronounced summer maximum and a secondary maximum in the spring. Both reanalyses show a high degree of correlation with the observed surface mass concentration. It is important to note, however, that surface concentration depends upon the the prevailing meteorology (e.g. PBL height, precipitation distribution) in addition to the aerosol vertical profile, the latter of which is not fully constrained in the assimilation. Differences between MERRAero and MERRA-2 arise from the fact that the model versions and physics are slightly different; MERRAero assimilated only bias-corrected (NNR) MODIS AOD, and MERRAero was driven by meteorology from MERRA. Figure 4.16 shows a comparison of the climatological dust surface concentration at the RSMAS Barbados [13.17°N, 59.53°W] and University of Miami [25.75°N, 80.25°W] stations. The long-term dust surface concentration seasonal cycle is well-simulated in MERRA-2 at both stations.

Pre-EOS observations of dust sedimentation and dust surface concentration at various stations around the world are shown in Figures 4.17 and 4.18, respectively, for the period 1980-1999. These observations are presented in Huneeus et al. (2011) and are derived from several sources: the Sea/Air Exchange (SEAREX) field campaign (Ginoux et al., 2001; Prospero et al., 1989), measurements presented in Mahowald et al. (2009), and measurements from the Dust Indicators and Records in Terrestrial and Marine Paleoenvironments (DIRTMAP) data set (Kohfeld and Harrison, 2001; Tegen et al., 2002). Compared to the GEOS-5/GOCART forecast model (i.e. without assimilation; Colarco et al., 2014b, their Figs. 5 and 6), MERRA-2 dust surface concentrations and deposition are generally the same or improved worldwide.

Finally, we examine the trans-Atlantic dust transport by comparing the slope of the zonal-mean AOD in MERRA-2 compared to MODIS Collection 5 retrievals. Note that the MODIS observations in Figure 4.19 are from the MOD04 product and are not the NNR retrievals used in the assimilation,
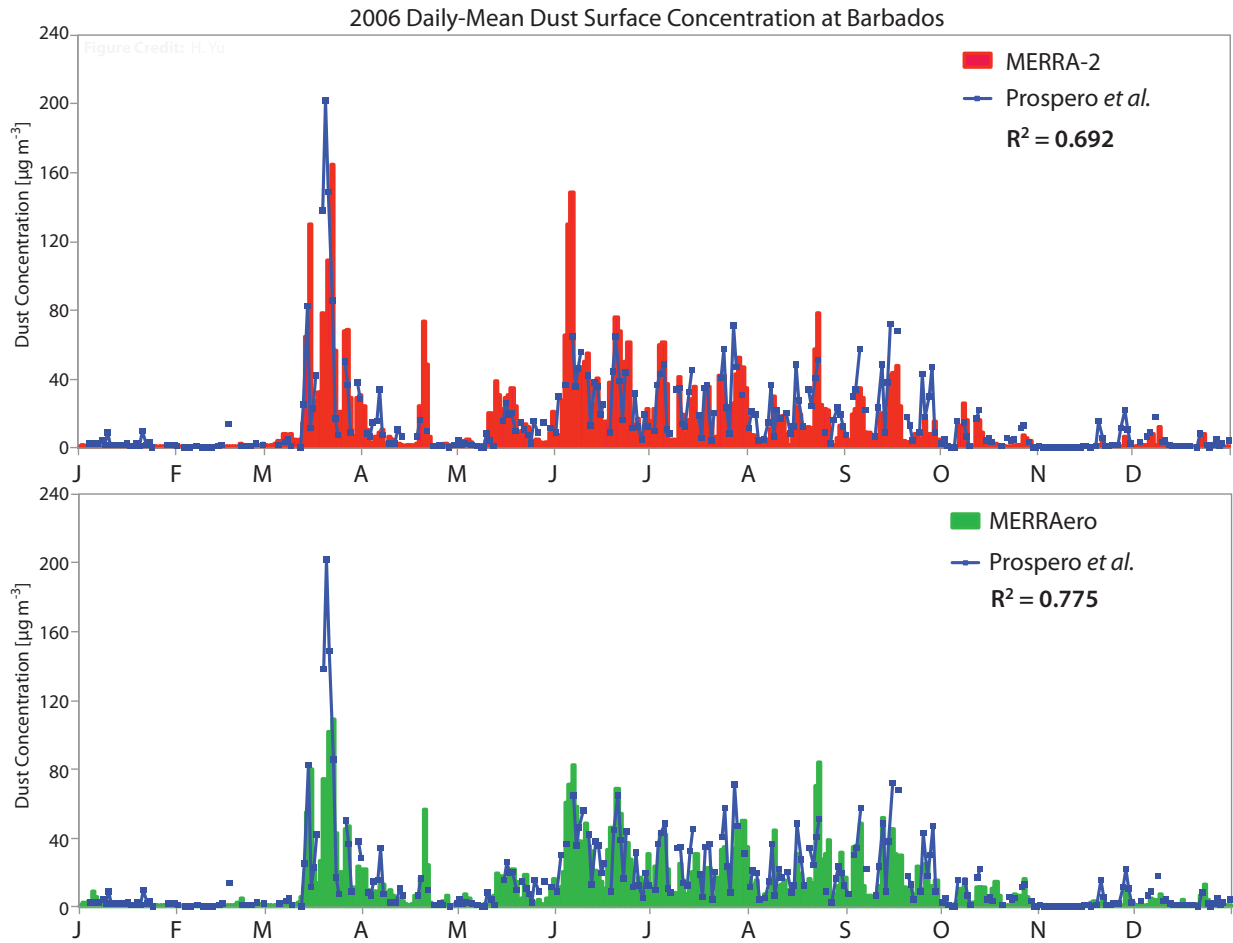
Figure 4.15: Daily-mean dust surface concentration [μg m^{-3}] at the RSMAS Barbados station [13.17°N, 59.53°W] for 2006 compared to MERRA-2 (top) and MERRAero (bottom).

which generally have lower AOD due to more stringent cloud-clearing. Nevertheless, both the model and observations show a similar decay in AOD from the African source region to the Caribbean region.

Sea salt surface concentrations: As shown in Figure 4.13, MERRA-2 overestimates the surface sea salt mass over the continental US. In the northeastern US, this is due to erroneous sea salt emissions from the Great Lakes due to an error in the land-masking algorithm that has since been corrected (see Fig. 2.1). Additionally, sea salt emissions penetrate into some coastal regions (see sea salt AOD in Appendix C), and such penetration is exacerbated by the assimilation if coastal AODs are lower than observed.
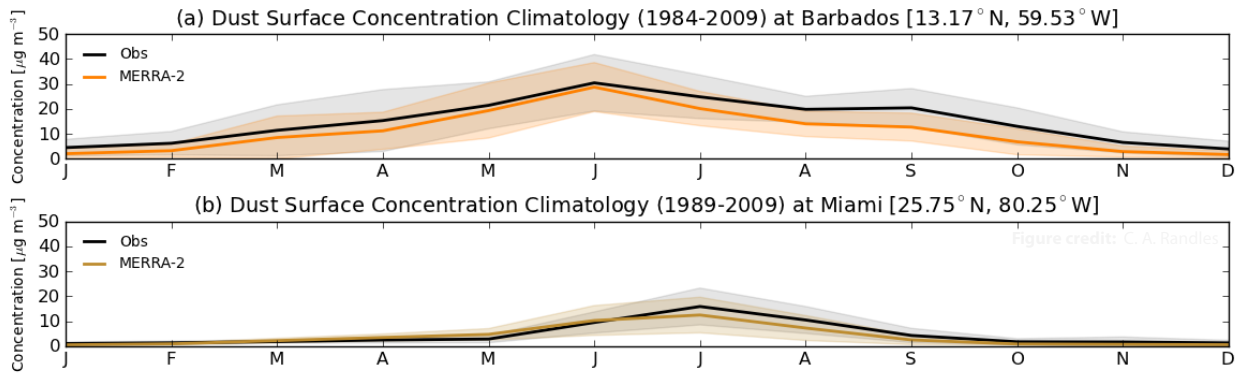
Figure 4.16: Climatology of monthly-mean dust surface concentration [μg m^{-3}] at the RSMAS Barbados [13.17°N, 59.53°W] and University of Miami [25.75°N, 80.25°W] stations. The mean (solid lines) and standard deviation (shading) are calculated for the period 1984-2009 at Barbados and 1989-2009 at the University of Miami. Note that data were available only as monthly means, so the model has not been sampled on sub-monthly timescales to be consistent with the measurements making up the reported monthly mean.
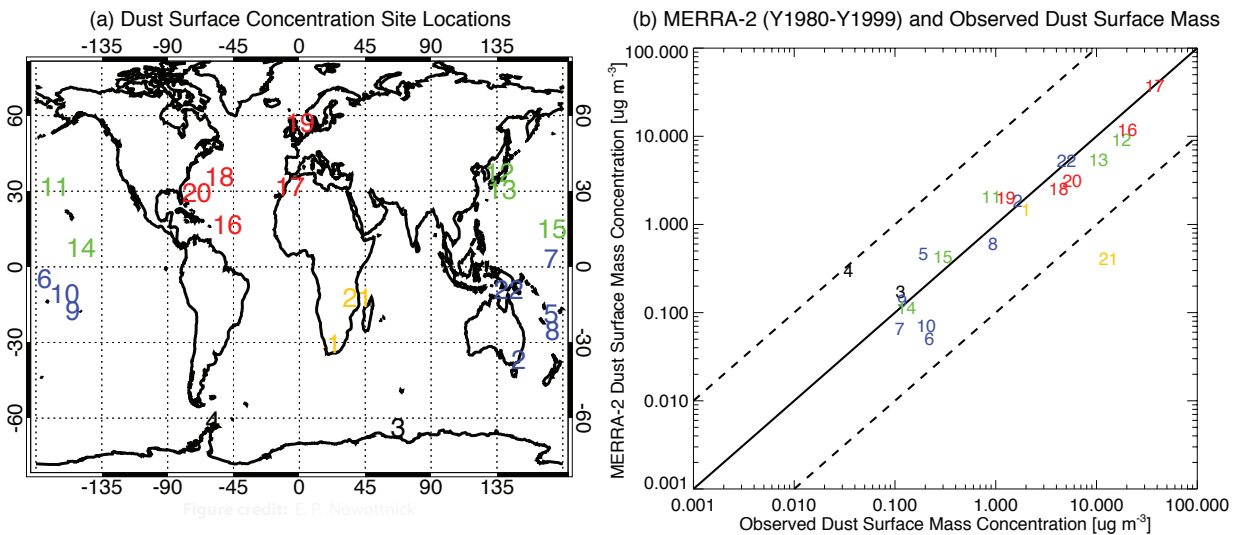
Figure 4.17: Dust surface mass concentration observations compared to MERRA-2. More details about the sites in (a) can be found in Colarco et al. (2014b) Table 3 and Huneeus et al. (2011). The scatter-plot in (b) shows the climatological-mean surface-concentration of MERRA-2 sampled at the surface site location and over the same years as the observations. The solid-line is the one-to-one line and the dashed lines are 10-to-1 and 1-to-10. Colors correspond to geographical regions, and numbers correspond to station locations in (a).
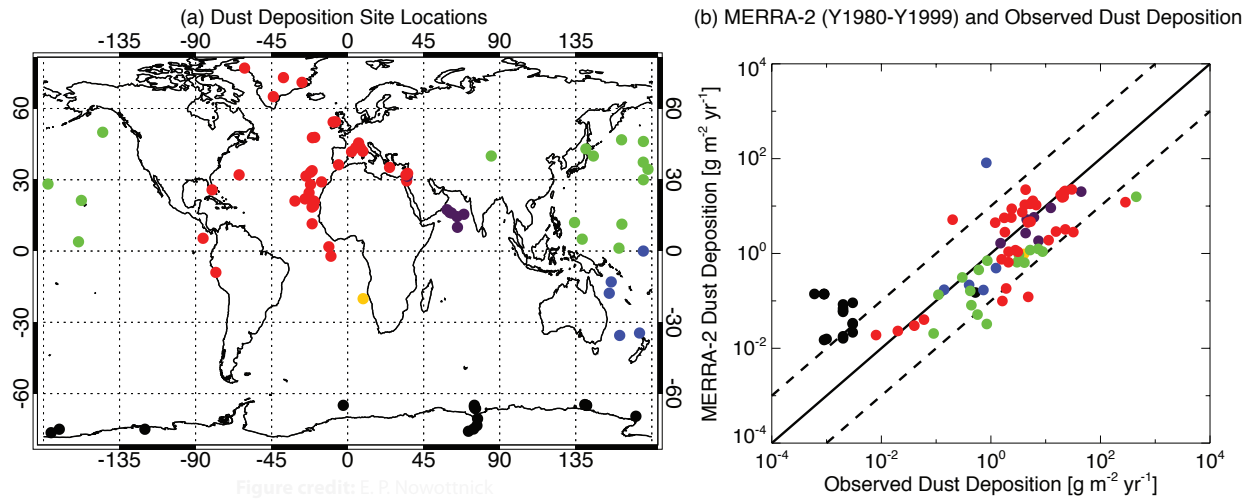
Figure 4.18: Same as Figure 4.17 except for dust deposition sites in Table S2 of Colarco et al. (2014b).
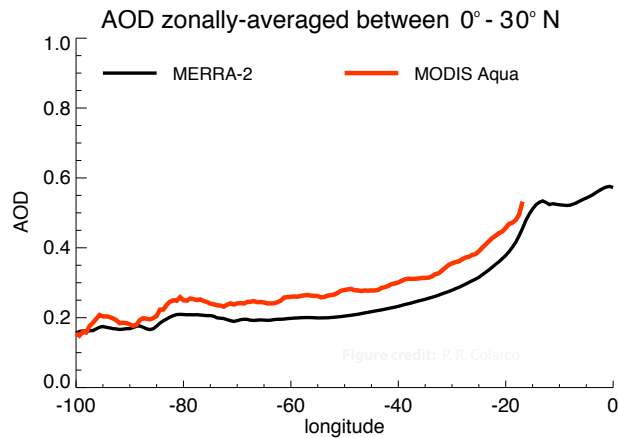
Figure 4.19: Meridional decay in AOD from the source region over Africa ($\sim$0°) to the Caribbean ($\sim$80° W) from MERRA-2 (black) and Collection 5 MODIS Aqua observations (red). Note that this is the standard MODIS data product, not the neural net retrieval used in the assimilation.
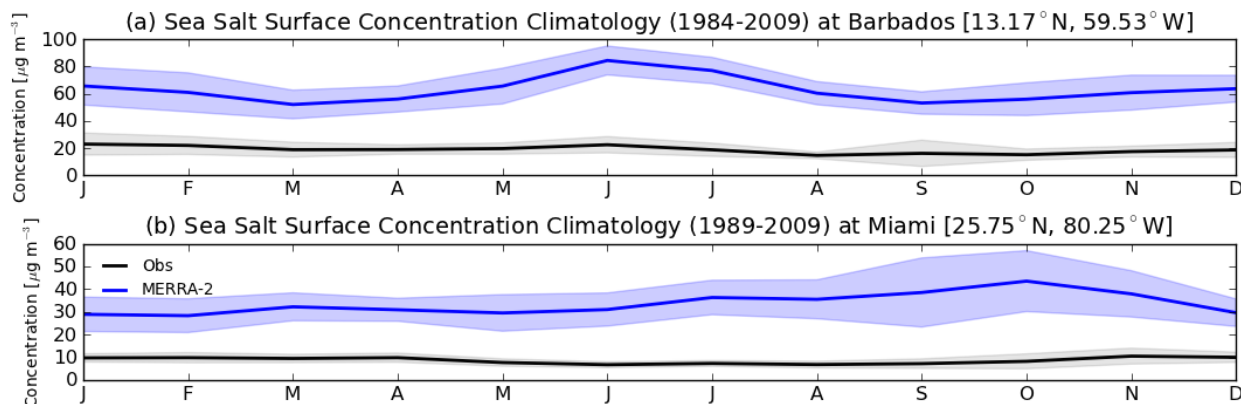
Figure 4.20: Climatology of monthly-mean sea salt concentration [μg m^{-3}] at the (a)RSMAS Barbados [13.17°N, 59.53°W] and (b) University of Miami [25.75°N, 80.25°W] stations. The mean (solid lines) and standard deviation (shading) are calculated for the period 1984-2009 at Barbados and 1989-2009 at the University of Miami. Note that data were available only as monthly means, so the model has not been sampled on sub-monthly timescales to be consistent with the measurements making up the reported monthly mean.

For example, Figures 4.20 and 4.21 show the surface sea salt and sulfate mass climatologies at the RSMAS Barbados and Miami sites for the periods of 1984-2009 and 1989-2009, respectively. At both stations, sea salt surface mass is overestimated by roughly a factor of 3 while sulfate mass is underestimated. The underestimate in SO$_4$ aerosol is similar to results from the offline GOCART model (Hongbin Yu, personal communication), indicating that there may be a missing sulfate aerosol source at these two stations. Rather than adding potentially missing extinction to sulfate, however, the assimilation tends to scale up the extinction proportionally to the forecast model aerosol composition, exacerbating the sea salt aerosol overestimate while somewhat reducing the low bias in sulfate aerosol.

A similar overestimate in sea salt aerosols (factor of 3) is seen at Cayenne in French Guiana, South America (Figure 4.22). To match the observable AOD in these coastal regions, MERRA-2 assumes the partitioning of aerosols *as is* from the forecast model. Thus, where sulfate is low, perhaps due to missing local sources, and sea salt is high due to the intrusion of emissions in coastal regions, when the assimilation imposes a positive AOD increment it exacerbates the overestimate in sea salt aerosol. Including only sea salt PM$_{2.5}$ in the calculation of PM$_{10}$ improves the agreement between the observations and MERRA-2 at Cayenne, indicating an overestimate of larger sea salt particles at this site.
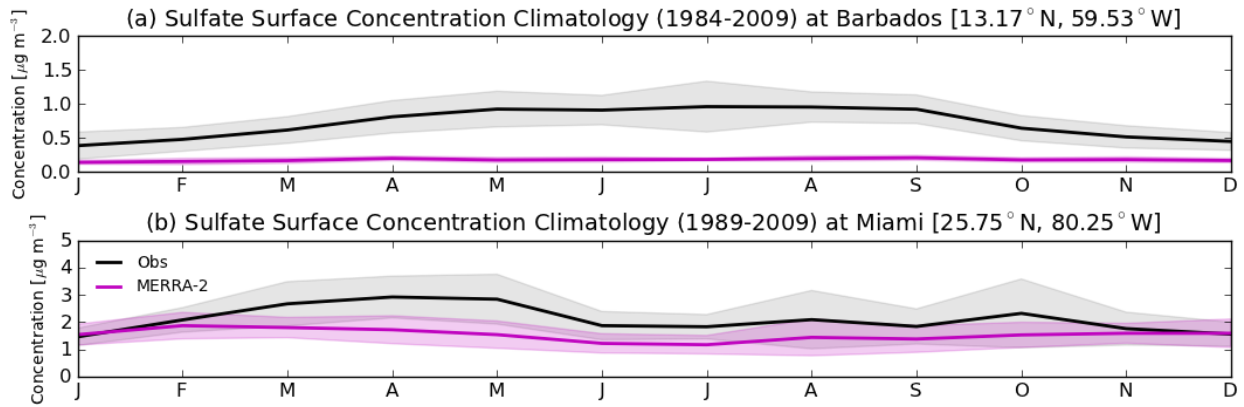
Figure 4.21: Same as 4.20 except for sulfate (SO$_4$)
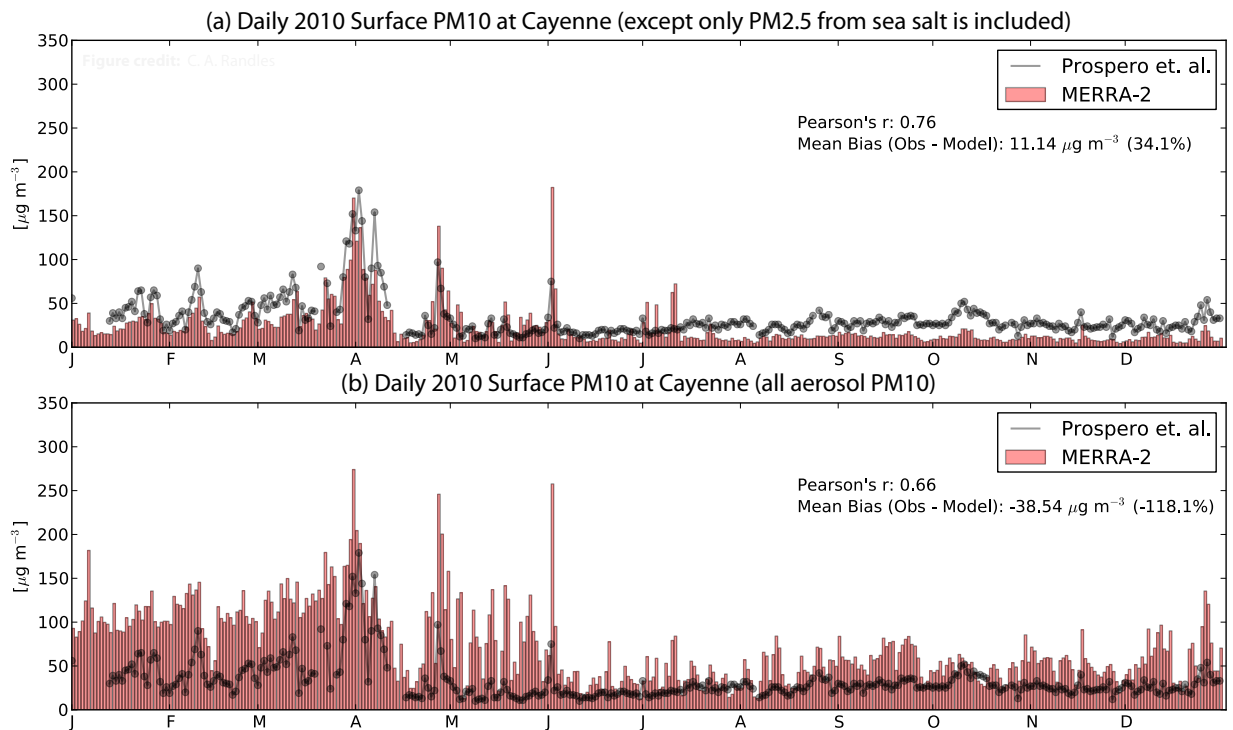
Figure 4.22: Comparison of observed and simulated surface PM$_{10}$ at Cayenne, French Guiana. (a) Comparison to MERRA-2 where PM$_{10}$ consists of *most* surface aerosols (dust, sulfate, organic and black carbon) plus sea salt PM$_{2.5}$. (b) Comparison to MERRA-2 where PM$_{10}$ consists of all surface aerosols (dust, sulfate, organic and black carbon, and sea salt), where the sea salt PM$_{10}$ is composed of all the sea salt bins.

4.8 Volcanic eruptions

Through conversion of SO_2 to SO_4 aerosol, large volcanic eruptions are a major source of reflective stratospheric sulfate aerosol that can cool the entire planet (Deshler, 2008; Robock, 2000). During the MERRA-2 aerosol reanalysis, the largest volcanic events were the 1982 El Chichón eruption in Mexico and the 1991 eruption of Mount Pinatubo in the Philippines. While stratospheric SO_4 from the earlier eruption was mainly confined to the Northern Hemisphere (McCormick and Swissler, 1983), the volcanic "cloud" from Pinatubo, which injected about 20 Tg of SO_2 into the atmosphere (Bluth et al., 1992), persisted for several years and diffused to the middle and high latitudes of both hemispheres (Aquila et al., 2012).

Figure 4.23 compares the approximate MERRA-2 stratospheric AOD at 550 nm to a reconstruction that was derived from observations from several instruments: the Stratospheric Aerosol and Gas Experiment II (SAGE-II), AVHRR, SAM II, lidar, and balloon observations (Stenchikov et al., 1998). Note that stratospheric AOD was not archived in MERRA-2. We therefore approximate the stratospheric portion of the AOD as in Aquila et al. (2012) by subtracting the AOD climtology calculated over January 1985 to May 1991. Compared to the reconstructed observations of Stenchikov et al. (1998) (Fig. 4.23), MERRA-2 well reproduces the peak observed stratospheric AOD (though it appears to be somewhat overestimated). Note that SAGE-observed AOD saturated at 0.15, and this is why the reconstructed AOD from Stenchikov et al. (1998) is lower than the approximated AVHRR-only stratospheric AOD. However, as with many global models, the volcanic plume too quickly spreads from the tropics to the polar regions whereas SAGE-II and AVHRR indicate that the plume was confined in the tropics for a longer period of time than simulated. This is likely due to the distribution of SO_2 up to 30 km into the stratosphere in the model, as indicated by the volcanic emissions database (Diehl et al., 2012). This plume height injection appears to be too high (Figure 4.24). The model does show the plume traveling towards both hemispheres as observed, and MERRA-2 also captures the November 1991 AOD cloud from the Cerro Hudson volcano (72.97°W, 45.90°S). Note that the increased AOD at high latitudes ($> 60°$) in summer is (a) not impacted by the AVHRR assimilation since no data exist at these latitudes and (b) is due to having highly hygroscopic SO_4 particles in a very high ($> 80\%$) relative humidity environment.

From the aerosol AOD timeseries in Figure 4.1 and Appendix B, it is clear that the eruptions of El Chichón and especially Pinatubo impacted not only the SO_4 AOD, but also the AOD of other species, especially dust and sea salt. Aquila et al. (2012) was able to show good agreement with

observations of the Pinatubo eruption AOD using a free-running version of GEOS-5. However, unlike in MERRA-2, the aforementioned study assumed a larger effective radius for volcanic SO_4 particles ($r_{eff} = 0.6$ μm) and injected them at a lower height (16-18 km). MERRA-2 treats all SO_4 aerosol using an effective radius that is more appropriate for non-volcanic, tropospheric aerosol. Smaller particles are more efficient at scattering visible light than larger particles. Thus, for the same amount of SO_4 injection, the assumption of smaller particles will yield an overestimate of sulfate AOD. When the assimilation then tries to reduce the AOD to better agree with the observations, it applies negative increments to *all* aerosol species proportionally. The apparent decrease in sea salt and dust AOD after Pinatubo is therefore an *artifact* of the assimilation process and the assumption of small effective radius for all sulfate particles, regardless of source. Figure 4.25 illustrates this point by showing the assimilated AVHRR observations, the model background or forecast, and the MERRA-2 analysis AOD for the period directly after the eruption. Clearly, the forecast AOD is too high compared to the assimilated observations, and the analysis AOD resembles the observations. This implies a negative AOD increment, which would be applied to all species, and not just stratospheric sulfate aerosol.
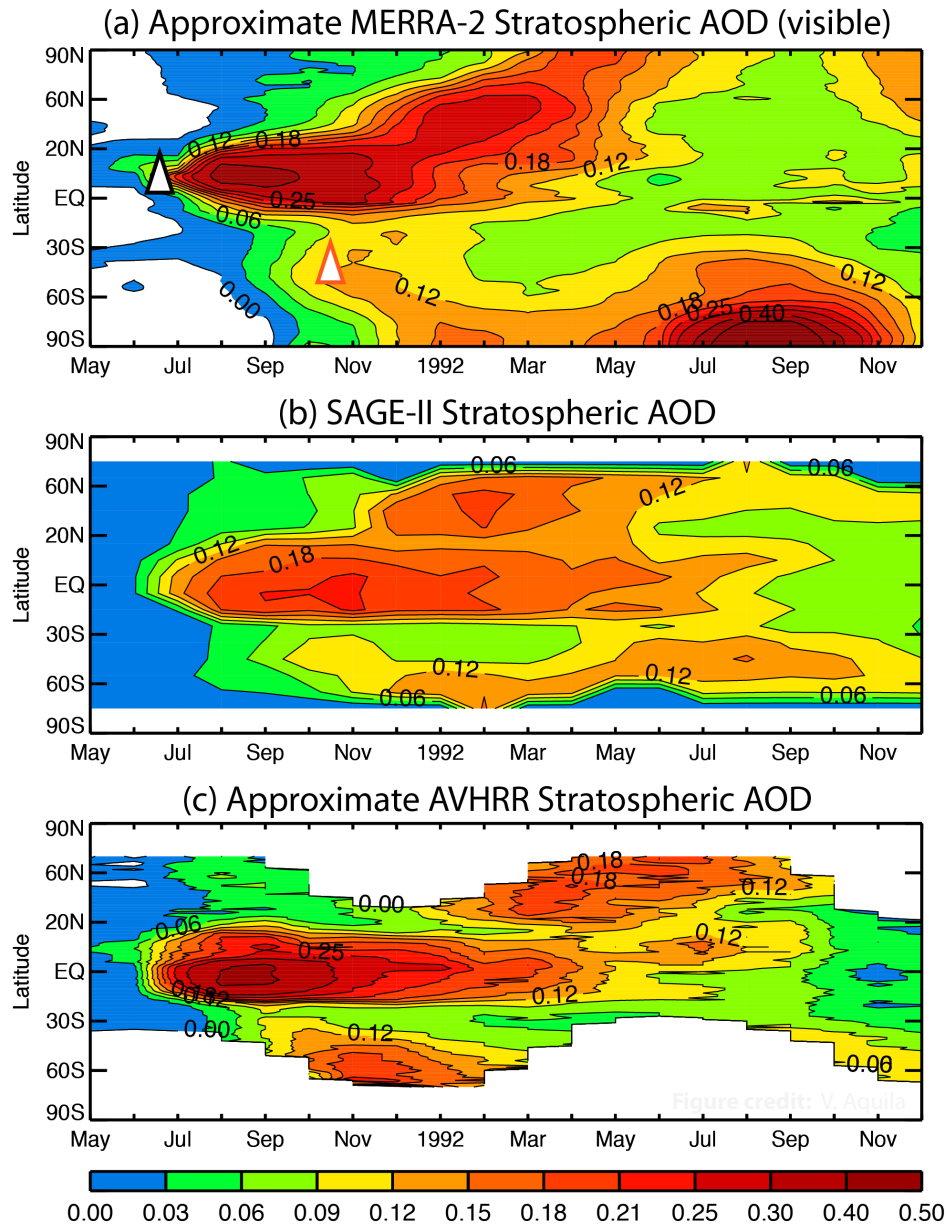
Figure 4.23: Zonal mean stratospheric AOD in the visible for (a) MERRA-2 and observed by (b) reconstructed SAGE II observations (Stenchikov et al., 1998) and (c) AVHRR. AVHRR measures total column AOD, and MERRA-2 did not separately archive stratospheric AOD. We therefore approximate the stratospheric AOD by removing the background values as in Aquila et al. (2012) (i.e. from the total AOD we subtracted the monthly AOD climatology calculated over January 1985 to May 1991 for MERRA-2 and from July 1989 to May 1991 for AVHRR). White triangles in (a) indicate the approximate times and locations of the Pinatubo (15.1°N, 120.4°E, 15 June 1991) and Cerro Hudson (45.9°S, 72.97°W, August-October 1991) eruptions.
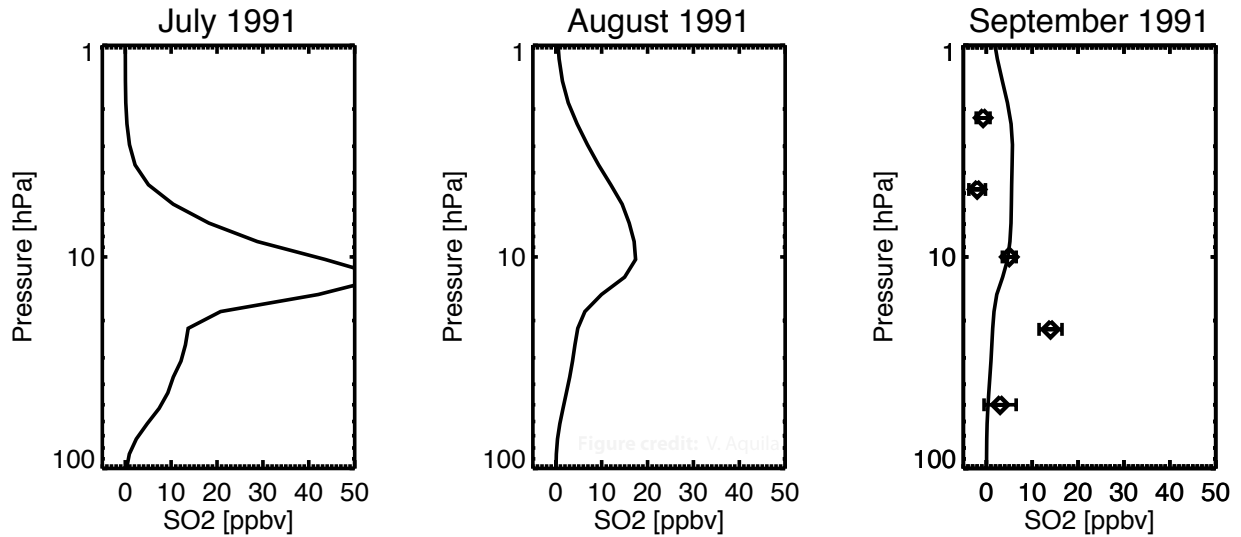
Figure 4.24: Monthly mean vertical distribution of stratospheric SO_2 in MERRA-2 after Pinatubo (black lines). The upper limit of the injection height in Diehl et al. (2012) was 30 km. The third panel (September 1991) includes observations from MLS (symbols), which indicate that the SO_2 injection height considered was likely too high. Microwave Limb Sounder (MLS) measurements are from Read et al. (1993)
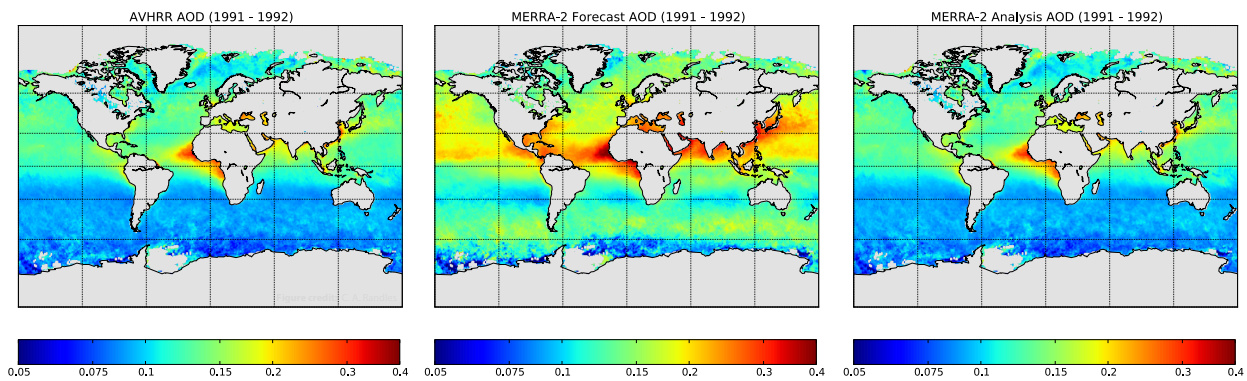
Figure 4.25: Comparison of (left) assimilated observations of AOD from AVHRR, (center) MERRA-2 forecasted AOD, and (right) the MERRA-2 reanalysis AOD for the years directly after the Pinatubo eruption. Because the observations (left) and analysis (right) look similar, it is clear that the assimilation draws strongly towards the observations; because the forecast (center) is much greater than the analysis (left), a negative AOD increment is implied.

67

Chapter 5

Summary and recommendations
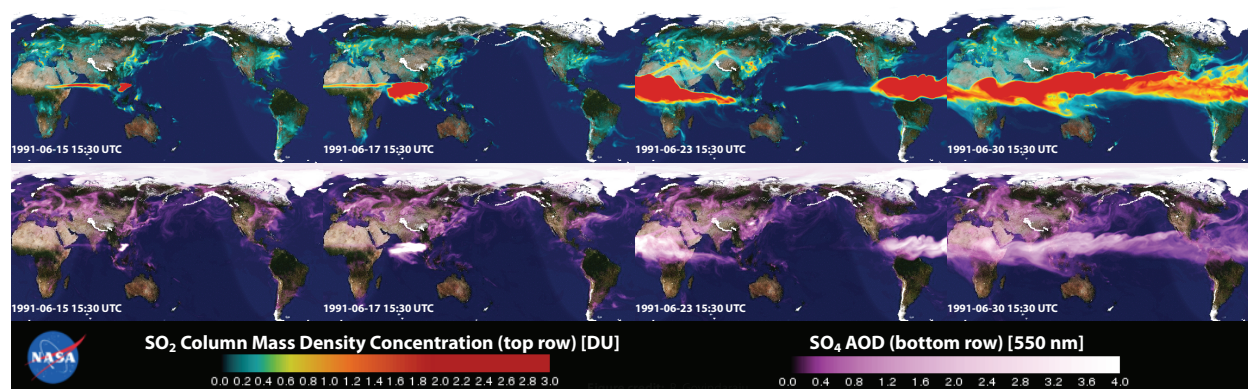
MERRA-2 AOD during July 1991 showing global transport of SO_2 (top row) and sulfate aerosols (bottom row) from the Pinatubo eruption on 15 June 1991. From left to right the dates are June 15, June 17, June 23, and June 30, 1991, all at 15:30 UTC.

Despite their rapid increase in complexity, aerosol models remain uncertain due to poorly constrained emissions and physical process parameterizations such as hygroscopic growth, mixing, and aerosol-cloud interactions (Benedetti et al., 2009; Kinne et al., 2006; Schutgens et al., 2010; Textor et al., 2006). Similarly, many aerosol observations such as those from remote sensing platforms, both satellite and ground based, suffer from limited coverage (e.g. due to their orbit and/or cloud contamination), contextual biases such as "clear-sky" bias, and biases due to assumptions made in retrieval algorithms (Shi et al., 2011; Zhang and Reid, 2009). Reanalyses optimally combine the continuity of a four-dimensional gridded model with observations that may be sparse and/or irregularly spaced both spatially and temporally (Rienecker et al., 2011; Schutgens et al., 2010). The resulting analyzed aerosol fields have numerous applications (see Bocquet et al. (2015) and

citations therein). Briefly, these fields can serve as initial conditions for regional modeling and air quality forecasting (Giordano et al., 2015; Zhang et al., 2012), as a tool to investigate aerosol-climate or aerosol-weather interactions (Bellouin et al., 2013; Reale et al., 2014), for use as *a priori* profiles used in satellite retrievals of other atmospheric constituents (Inness et al., 2013), and for optimal network/satellite sensor design in the context of Observing System Simulation Experiments (OSSEs) (e. g. Buchard et al., 2015; Colarco et al., 2014b).

In this document we have presented an overview of the NASA MERRA-2 aerosol assimilation, the first publicly available modern satellite-era aerosol reanalysis performed concurrently with a meteorological reanalysis. The evaluation presented here represents only an initial evaluation; more complete evaluations will come with time as manuscripts are prepared and submitted for peer-reviewed publication (see `http://gmao.gsfc.nasa.gov/reanalysis/MERRA-2/pubs/`).

Several important caveats must be understood when using the MERRA-2 aerosol reanalysis products. First, the relative paucity of (non-assimilated) aerosol observations make independent validation on the analyzed AOD challenging. Second, despite best efforts at harmonizing the observing system through quality control, differences in data coverage impact the analyzed aerosol AOD, particularly seen when comparing the pre- and post-Earth Observing System (EOS) periods (1980-1999 and 2000 onwards, respectively). Finally, and perhaps most importantly, non-analyzed aerosol properties (e.g. everything *other than AOD* such as vertical distribution, aerosol speciation, absorption) are not fully-constrained by the assimilation and draw strongly to the background model in most cases. Nevertheless, despite some deficiencies, previous studies (e.g. Buchard et al., 2015) and the current document demonstrate that the MERRA-2 GAAS modeling system does indeed show considerable skill in simulating numerous observable aerosol properties.

Below we summarize some of the strengths and weaknesses of MERRA-2's representation of aerosols and make recommendations for their use. The noted sections can be consulted for further details.

- As expected, compared to the forecasted AOD, the analyzed AOD fields show excellent agreement with spatially and temporally co-located observations from the assimilated sensors (Table 3.1; Section 3.3).

- MERRA-2 assimilates *bias-corrected* AOD from MODIS and AVHRR (Section 3.2.2). This must be considered when comparing the analyzed AOD fields to products available directly from instrument teams which *were not assimilated*.

- Because they are not available in Near Real Time (NRT), MISR and AERONET observations are not assimilated after June 2014 and October 2014, respectively. AVHRR assimilation ends when MODIS Aqua assimilation begins (August 2002) since both have afternoon equator crossings (Table 3.1).

- MERRA-2 assimilates AOD at 3-hour synoptic times only *when* and *where* data are available. AVHRR observations were only over the ocean for the pre-EOS period. MODIS data are only available for clear-sky regions and where the surface albedo is low. MISR takes approximately 9 days for full global coverage, and AERONET data availability depends on clear-sky conditions and operating conditions at specific stations. All observations are only available during the sunlit portion of the day (Section 3.2). The available AOD increments indicate gridboxes subjected to the AOD assimilation for a given time. When data are not available, the analysis resembles the forecast from the background model (e.g. Fig. 3.9).

- Compared to co-located, available, independent observations of AOD (aircraft, ship, and ground-based), MERRA-2 has both a high degree of correlation and low bias (Section 4.3).

- MERRA-2 Aerosol Absorption Optical Depth (AAOD) and simulated UV Aerosol Index (AI) compare well with observations from OMI; however, AI is biased low over southern Africa because GOCART does not currently consider the strong spectral variation of absorption in the near-UV associated with brown carbon (Buchard et al., 2016, Section 4.4).

- Like many global aerosol models, GOCART tends to overestimate black carbon aerosol mass in the remote free troposphere (Fig. 4.10). Black carbon aerosol is a small contributor to AOD but a strong contributor to Aerosol Absorption Optical Depth (AAOD). Thus, despite the reasonable agreement between OMI and MERRA-2 AAOD (Fig. 4.6), it is likely AAOD is overestimated particularly in regions remote from the major sources (e.g. biomass burning regions). Care must be taken, then, when examining the all-sky aerosol direct radiative effect and the clear-sky direct radiative effect over bright surfaces (e.g. polar regions) as these quantities are sensitive to both the AOD and the AAOD.

- MERRA-2 generally shows good agreement with CALIOP and aircraft observations of the vertical structure of aerosol optical properties (Section 4.5). The use of Local Displacement Ensembles (LDE) to characterize plume misplacements (Section 3.1) means that the vertical structure of the aerosol fields is not simply a scaling of the forecast fields, but rather represents an optimal weighting of nearest neighbor gridboxes that best minimize the needed AOD increment. Our comparisons show that these plume misplacements generally improve the

representation of aerosol optical properties in the vertical compared to observations.

- Small particulate mass ($PM_{2.5}$) in MERRA-2 generally agrees well with observations as it did in our previous reanalysis (MERRAero, Buchard et al., 2016). Discrepancies in total $PM_{2.5}$ in the western United States arise due to the lack of nitrate in GOCART and too-low emissions of organic carbon (Section 4.6). Additionally, as seen in Section 4.7, surface sea salt aerosol is overestimated in the northeastern US (due to erroneous lake-masking) and in some coastal regions (due to weak wet deposition). Dust surface mass shows good agreement with observations, especially over the North Atlantic transport region (Figs. 4.15, 4.16, 4.17, and 4.18)

- With the exception of plume misplacements associated with the LDE algorithm (Section 3.1), the apportionment of aerosol mass amongst the various aerosol tracers (species) is determined by the convolution of the aerosol parameterizations and assumptions built into the GOCART model with the GEOS-5 meteorology and assumed aerosol emissions. If a particular species is overestimated by mass, a positive AOD increment will exacerbate this underlying bias. Thus, it is possible to have a good agreement between AOD and observations while having a poor agreement with speciated mass and/or speciated aerosol optical properties.

- The injection altitude of the Mt. Pinatubo 1991 eruption was too high in MERRA-2, and this led to quicker transport of the plume from the tropics to the poles. Further, MERRA-2 treats all sulfate aerosol as having the same extinction coefficient ($\beta_{ext,i}$) and thus the same assumed size distribution. Smaller particles are optically more efficient at scattering light compared to larger particles. For the amount of SO_2 injected by the Pinatubo eruption (20 Tg), this assumption led to an overestimate of AOD and a negative AOD increment (Fig. 4.25). The negative increment is applied to *all* aerosol tracers. This results in a marked decrease in the AOD of non-sulfate aerosol directly after the eruption (Fig. 4.1 and Appendix B). These decreases are an *artifact* of the negative AOD increment, and care must be taken when examining the speciated AOD timeseries after major volcanic eruptions.

- Care must always be taken when examining trends from *any* reanalysis product. This is true for both the MERRA-2 analyzed AOD fields and *especially* for other, non-analyzed aerosol products (e.g. speciated AOD). Changes in the observing system, data availability and coverage, and changes in assumed emissions inventories all impart a signature on these fields. For example, as seen in Appendix C, pre- and post-EOS dust seasonal cycles differ. Before 2000, AVHRR data are only available over the ocean; therefore, dust emissions over the land source regions resembles the forecast model. Biomass burning emissions prior to

1997 are scaled from the RETRO database, which incorporates far fewer observations than the MODIS-based GFED and QFED inventories. Further, prior to 2010, biomass burning emissions are monthly; thereafter they are daily (Section 2.2.2). Anthropogenic emissions generally only have inter-annual variability (Section 2.2.3).

- Aerosol increments, available for both total AOD and three-dimensional aerosol mass mixing ratios, can be used to examine when and where there are systematic biases in the model (e.g. where emissions are low or where loss is too high) by considering mass balance with the incremental mass as an additional term.

These brief points only summarize the more detailed results presented in this document. Future peer-reviewed publications will shed more light on both the successes and weaknesses of this first-ever modern satellite-era aerosol reanalysis. Separate technical memoranda describe in detail the performance of the MERRA-2 climate (Bosilovich et al., 2016), including the improved representation of the stratosphere, and the MERRA-2 meteorological observing system (McCarty, 2016). As this is a publicly available reanalysis, we invite the community of users to contact us with any questions, to share important results, and to provide any other feedback that will be helpful in the development of the GMAO's next reanalysis. Questions and comments can be sent to merra-questions@lists.nasa.gov.

References

Aquila, V., C. I. Garfinkel, P. Newman, L. Oman, and D. Waugh, 2014: Modifications of the Quasi-Biennial Oscillation by a geoengineering perturbation of the stratospheric aerosol layer. *Geophysical Research Letters*, **41 (5)**, 1738–1744, 10.1002/2013GL058818, URL http://dx.doi.org/10.1002/2013GL058818.

Aquila, V., L. D. Oman, R. S. Stolarski, P. R. Colarco, and P. A. Newman, 2012: Dispersion of the volcanic sulfate cloud from a Mount Pinatubo–like eruption. *Journal of Geophysical Research: Atmospheres*, **117 (D6)**, 10.1029/2011JD016968, URL http://dx.doi.org/10.1029/2011JD016968.

Bellouin, N., J. Quaas, J.-J. Morcrette, and O. Boucher, 2013: Estimates of aerosol radiative forcing from the MACC re-analysis. *Atmospheric Chemistry and Physics*, **13 (4)**, 2045–2062, 10.5194/acp-13-2045-2013, URL http://www.atmos-chem-phys.net/13/2045/2013/.

Benedetti, A., and Coauthors, 2009: Aerosol analysis and forecast in the European Centre for Medium-range Weather Forecasts Integrated Forecast System: 2. Data assimilation. *Journal of Geophysical Research: Atmospheres*, **114 (D13)**, 10.1029/2008JD011115, URL http://dx.doi.org/10.1029/2008JD011115.

Bian, H., and Coauthors, 2013: Source attributions of pollution to the Western Arctic during the NASA ARCTAS field campaign. *Atmospheric Chemistry and Physics*, **13 (9)**, 4707–4721, 10.5194/acp-13-4707-2013, URL http://www.atmos-chem-phys.net/13/4707/2013/.

Bluth, G. J. S., S. D. Doiron, C. C. Schnetzler, A. J. Krueger, and L. S. Walter, 1992: Global tracking of the SO_2 cloud from the June, 1991 Mount Pinatubo eruptions. *Geophysical Research Letters*, **19 (2)**, 151–154, 10.1029/91GL02792, URL http://dx.doi.org/10.1029/91GL02792.

Bocquet, M., and Coauthors, 2015: Data assimilation in atmospheric chemistry models: Current status and future prospects for coupled chemistry meteorology models. *Atmospheric Chemistry and Physics*, **15 (10)**, 5325–5358, 10.5194/acp-15-5325-2015, URL http://www.atmos-chem-phys.net/15/5325/2015/.

Bond, T. C., D. G. Streets, K. F. Yarber, S. M. Nelson, J.-H. Woo, and Z. Klimont, 2004: A technology-based global inventory of black and organic carbon emissions from combustion. *Journal of Geophysical Research: Atmospheres*, **109 (D14)**, 10.1029/2003JD003697, URL http://dx.doi.org/10.1029/2003JD003697.

Bosilovich, M. G., and Coauthors, 2016: MERRA-2: Initial evaluation of the climate. Technical Report Series on Global Modeling and Data Assimilation 43, NASA Global Modeling and Assimilation Office. URL http://gmao.gsfc.nasa.gov/pubs/tm/docs/Bosilovich803.pdf.

Buchard, V., and Coauthors, 2014: Evaluation of GEOS-5 sulfur dioxide simulations during the Frostburg, MD 2010 field campaign. *Atmospheric Chemistry and Physics*, **14 (4)**, 1929–1941, 10.5194/acp-14-1929-2014, URL http://www.atmos-chem-phys.net/14/1929/2014/.

Buchard, V., and Coauthors, 2015: Using the OMI aerosol index and absorption aerosol optical depth to evaluate the NASA MERRA Aerosol Reanalysis. *Atmospheric Chemistry and Physics*, **15 (10)**, 5743–5760, 10.5194/acp-15-5743-2015, URL http://www.atmos-chem-phys.net/15/5743/2015/.

Buchard, V., and Coauthors, 2016: Evaluation of the surface $PM_{2.5}$ in Version 1 of the NASA MERRA Aerosol Reanalysis over the United States. *Atmospheric Environment*, **125**, 100–111, 10.1016/j.atmosenv.2015.11.004, URL http://www.sciencedirect.com/science/article/pii/S1352231015305136.

Chambers, J., W. Cleveland, B. Kleiner, and P. Tukey, 1983: *Graphical Methods for Data Analysis*. Wadsworth.

Chin, M., and Coauthors, 2002: Tropospheric aerosol optical thickness from the GOCART model and comparisons with satellite and sun photometer measurements. *Journal of the Atmospheric Sciences*, **59**, 461–483, 10.1175/1520-0469(2002)059<0461:TAOTFT>2.0.CO;2, URL http://dx.doi.org/10.1175/1520-0469(2002)059<0461:TAOTFT>2.0.CO;2.

Cohn, S., A. da Silva, and J. Guo, 1998: Assessing the effects of data selection with the DAO Physical-Space Statistical Analysis System. *Monthly Weather Review*, **126**, 2913–2926.

Colarco, P., A. da Silva, M. Chin, and T. Diehl, 2010: Online simulations of global aerosol distributions in the NASA GEOS-4 model and comparisons to satellite and ground-based aerosol optical depth. *Journal of Geophysical Research*, **115 (D14207)**, 10.1029/2009JD012820, URL http://dx.doi.org/10.1029/2009JD012820.

Colarco, P. R., R. A. Kahn, L. A. Remer, and R. C. Levy, 2014a: Impact of satellite viewing-swath width on global and regional aerosol optical thickness statistics and trends. *Atmospheric Measurement Techniques*, **7 (7)**, 2313–2335, 10.5194/amt-7-2313-2014, URL http://dx.doi.org/10.5194/amt-7-2313-2014.

Colarco, P. R., E. P. Nowottnick, C. A. Randles, B. Yi, P. Yang, K.-M. Kim, J. A. Smith, and C. G. Bardeen, 2014b: Impact of radiatively interactive dust aerosols in the NASA GEOS-5 climate model: Sensitivity to dust particle shape and refractive index. *Journal of Geophysical Research: Atmospheres*, **119 (2)**, 753–786, 10.1002/2013JD020046, URL http://dx.doi.org/10.1002/2013JD020046.

Cross, E. S., and Coauthors, 2010: Soot particle studies instrument inter-comparison project overview. *Aerosol Science and Technology*, **44**, 592–611, 10.1080/02786826.2010.482113, URL http://www.tandfonline.com/doi/abs/10.1080/02786826.2010.482113.

Darmenov, A. S., and A. da Silva, 2015: The Quick Fire Emissions Dataset (QFED) - Documentation of versions 2.1, 2.2 and 2.4. Tech. rep., NASA Global Modeling and Assimilation Office. URL http://gmao.gsfc.nasa.gov/pubs/docs/Darmenov796.pdf.

de Graaf, M., and P. Stammes, 2005: SCIAMACHY Absorbing Aerosol Index – calibration issues and global results from 2002–2004. *Atmospheric Chemistry and Physics*, **5**, 2385–2394, 10.5194/acp-5-2385-2005, URL http://www.atmos-chem-phys.net/5/2385/2005/acp-5-2385-2005.pdf.

Dee, D. P., and A. M. da Silva, 1999: Maximum-likelihood estimation of forecast and observation error covariance parameters. part i: Methodology. *Monthly Weather Review*, **127**, 1811–1834, URL http://dx.doi.org/10.1175/1520-0493(1999)127<1822:MLEOFA>2.0.CO;2.

Dee, D. P., L. Rukhovets, R. Todling, A. M. da Silva, and L. J. W., 2001: An adaptive buddy check for observational quality control. *Quarterly Journal of the Royal Meteorological Society*, **127**, 2451–2471, 10.1002/qj.49712757714, URL http://dx.doi.org/10.1002/qj.49712757714.

Dentener, F., 2006: Emission of primary aerosol and precursor gases in the years 2000 and 1750: Prescribed data-sets for AeroCom. *Atmospheric Chemistry and Physics*, **6**, 4321–4344, 10.5194/acp-6-4321-2006, URL http://dx.doi.org/10.5194/acp-6-4321-2006.

Deshler, T., 2008: A review of global stratospheric aerosol: Measurements, importance, life cycle and local stratospheric aerosol. *Atmospheric Research*, **90 (2–4)**, 223–232, 10.1016/j.atmosres.2008.03.016, URL http://dx.doi.org/10.1016/j.atmosres.2008.03.016.

Diehl, T., A. Heil, M. Chin, X. Pan, D. Streets, M. Schultz, and S. Kinne, 2012: Anthropogenic, biomass burning, and volcanic emissions of black carbon, organic carbon, and SO_2 from 1980 to 2010 for hindcast model experiments. *Atmospheric Chemistry and Physics Discussions*, **12 (9)**, 24 895–24 954, 10.5194/acpd-12-24895-2012, URL http://www.atmos-chem-phys-discuss.net/12/24895/2012/.

Diner, D., and Coauthors, 1998: Multi-angle Imaging SpectroRadiometer (MISR) instrument description and experiment overview. *IEEE Transactions onGeoscience and Remote Sensing*, **36 (4)**, 1072–1087, 10.1109/36.700992, URL http://dx.doi.org/10.1109/36.700992.

Dunagan, S. E., and Coauthors, 2013: Spectrometer for Sky-Scanning Sun-Tracking Atmospheric Research (4STAR): Instrument technology. *Remote Sensing*, **5 (8)**, 10.3390/rs5083872, URL http://dx.doi.org/10.3390/rs5083872.

Duncan, B. N., R. V. Martin, A. C. Staudt, R. Yevich, and J. A. Logan, 2003: Interannual and seasonal variability of biomass burning emissions constrained by satellite observations. *Journal of Geophysical Research: Atmospheres*, **108 (D2)**, 10.1029/2002JD002378, URL http://dx.doi.org/10.1029/2002JD002378.

EANET, 2000a: Quality Assurance/Quality Control (QA/QC) program for wet deposition monitoring in East Asia. URL http://www.eanet.cc/product/qaqc/qaqcwet.pdf.

EANET, 2000b: Technical manual for wet deposition monitoring in East Asia. URL http://www.eanet.cc//product/techwet.pdf.

EANET, 2001: Quality Assurance/Quality Control (QA/QC) program for the air concentration monitoring in East Asia. URL http://www.eanet.cc/product/qaqc/qaqcair.pdf.

EANET, 2006: Data report on the acid deposition in the East Asian region 2000 to 2005. URL http://www.eanet.cc/product.html.

European Comission, 2011: European Commission/Joint Research Centre (JRC)/Netherlands Environmental Assessment agency (PBL): Emission Database for Global Atmospheric Research (EDGAR), release version 4.2. URL http://edgar.jrc.ec.europa.eu.

European Commission, 2010: European Commission/Joint Research Centre (JRC)/Netherlands Environmental Assessment agency (PBL): Emission Database for Global Atmospheric Research (EDGAR), release version 4.1. URL http://edgar.jrc.ec.europa.eu.

Eyring, V., H. W. Köhler, J. van Aardenne, and A. Lauer, 2005: Emissions from international shipping: 1. The last 50 years. *Journal of Geophysical Research: Atmospheres*, **110 (D17)**, 10.1029/2004JD005619, URL http://dx.doi.org/10.1029/2004JD005619.

Gerber, H. E., 1985: Relative-humidity parameterization of the Navy Aerosol Model (NAM). Tech. Rep. NTIS ADA1632090, Naval Research Laboratory, Washington, DC.

Ginoux, P., M. Chin, I. Tegen, J. M. Prospero, B. Holben, O. Dubovik, and S.-J. Lin, 2001: Sources and distributions of dust aerosols simulated with the GOCART model. *Journal of Geophysical Research: Atmospheres*, **106 (D17)**, 20 255–20 273, 10.1029/2000JD000053, URL http://dx.doi.org/10.1029/2000JD000053.

Giordano, L., and Coauthors, 2015: Assessment of the MACC reanalysis and its influence as chemical boundary conditions for regional air quality modeling in AQMEII-2. *Atmospheric Environment*, **115**, 371–388, http://dx.doi.org/10.1016/j.atmosenv.2015.02.034, URL http://www.sciencedirect.com/science/article/pii/S1352231015001533.

Gong, S. L., 2003: A parameterization of sea-salt aerosol source function for sub- and super-micron particles. *GBC*, **17 (4)**, 10.1029/2003GB002079, URL http://dx.doi.org/10.1029/2003GB002079.

Gorkavyi, N., D. F. Rault, P. A. Newman, A. M. da Silva, and A. E. Dudorov, 2013: New stratospheric dust belt due to the Chelyabinsk bolide. *Geophysical Research Letters*, **40 (17)**, 4728–4733, 10.1002/grl.50788, URL http://dx.doi.org/10.1002/grl.50788.

Guenther, A., and Coauthors, 1995: A global model of natural volatile organic compound emissions. *Journal of Geophysical Research: Atmospheres*, **100 (D5)**, 8873–8892, 10.1029/94JD02950, URL http://dx.doi.org/10.1029/94JD02950.

Hair, J. W., and Coauthors, 2008: Airborne High Spectral Resolution Lidar for profiling aerosol optical properties. *Applied Optics*, **47 (36)**, 6734–6752, 10.1364/AO.47.006734, URL http://ao.osa.org/abstract.cfm?URI=ao-47-36-6734.

Hand, J., and Coauthors, 2011: IMPROVE (Interagency Monitoring of Protected Visual Environments): Spatial and seasonal patterns and temporal variability of haze and its constituents in the United States. Tech. Rep. 0737-5352-87, Colorado State University, Fort Collins. URL http://vista.cira.colostate.edu/improve/publications/reports/2011/PDF/Cover_TOC.pdf.

Heidinger, A. K., M. J. Foster, A. Walther, and X. Zhao, 2014: The Pathfinder Atmospheres – Extended AVHRR climate dataset. *Bulletin of the American Meteorological Society*, 909–922, 10.1175/BAMS-D-12-00246.1, URL http://journals.ametsoc.org/doi/abs/10.1175/BAMS-D-12-00246.1.

Henze, D. K., J. H. Seinfeld, and D. T. Shindell, 2009: Inverse modeling and mapping US air quality influences of inorganic $PM_{2.5}$ precursor emissions using the adjoint of GEOS-Chem. *Atmospheric Chemistry and Physics*, **9 (16)**, 5877–5903, 10.5194/acp-9-5877-2009.

Herman, J. R., P. K. Bhartia, O. Torres, C. Hsu, C. Sefto, and E. Celarier, 1997: Global distribution of UV-absorbing aerosols from Nimbus 7/TOMS data. *Journal of Geophysical Research*, **102**, 16 911–16 922, 10.1029/96JD03680, URL http://onlinelibrary.wiley.com/doi/10.1029/96JD03680/full.

Hess, M., P. Koepke, and I. Schult, 1998: Optical Properties of Aerosols and Clouds: The software package OPAC. *Bulletin of the American Meteorological Society*, **79**, 831–844, 10.1175/1520-0477(1998)079<0831:OPOAAC>2.0.CO;2, URL http://dx.doi.org/10.1175/1520-0477(1998)079<0831:OPOAAC>2.0.CO;2.

Holben, B., and Coauthors, 1998: AERONET – A federated instrument network and data archive for aerosol characterization. *Remote Sensing of Environment*, **66 (1)**, 1–16, 10.1016/S0034-4257(98)00031-5, URL http://www.sciencedirect.com/science/article/pii/S0034425798000315.

Hsu, N., and Coauthors, 1999: Comparisons of the TOMS aerosol index with sun-photometer aerosol optical thickness: results and applications. *Journal of Geophysical Research*, **104**, 6269–6279, 10.1029/1998JD200086, URL http://onlinelibrary.wiley.com/doi/10.1029/1998JD200086/full.

Huneeus, N., and Coauthors, 2011: Global dust model intercomparison in AeroCom Phase I. *Atmospheric Chemistry and Physics*, **11 (15)**, 7781–7816, 10.5194/acp-11-7781-2011, URL http://www.atmos-chem-phys.net/11/7781/2011/.

Inness, A., and Coauthors, 2013: The MACC reanalysis: An 8 yr data set of atmospheric composition. *Atmospheric Chemistry and Physics*, **13 (8)**, 4073–4109, 10.5194/acp-13-4073-2013, URL http://www.atmos-chem-phys.net/13/4073/2013/.

Jacob, D. J., and Coauthors, 2010: The Arctic Research of the Composition of the Troposphere from Aircraft and Satellites (ARCTAS) mission: Design, execution, and first results. *Atmospheric Chemistry and Physics*, **10 (11)**, 5191–5212, 10.5194/acp-10-5191-2010, URL http://www.atmos-chem-phys.net/10/5191/2010/.

Jaeglé, L., P. K. Quinn, T. S. Bates, B. Alexander, and J.-T. Lin, 2011: Global distribution of sea salt aerosols: New constraints from in situ and remote sensing observations. *ACP*, **11 (7)**, 3137–3157, 10.5194/acp-11-3137-2011, URL http://www.atmos-chem-phys.net/11/3137/2011/.

Kahn, R. A., B. J. Gaitley, J. V. Martonchik, D. J. Diner, K. A. Crean, and B. Holben, 2005: Multiangle Imaging Spectroradiometer (MISR) global aerosol optical depth validation based on 2 years of coincident Aerosol Robotic Network (AERONET) observations. *Journal of Geophysical Research – Atmospheres*, **110 (D10)**, 10.1029/2004JD004706, URL http://dx.doi.org/10.1029/2004JD004706.

Kaiser, J. W., and Coauthors, 2012: Biomass burning emissions estimated with a global fire assimilation system based on observed fire radiative power. *Biogeosciences*, **9 (1)**, 527–554, 10.5194/bg-9-527-2012, URL http://www.biogeosciences.net/9/527/2012/.

Kinne, S., and Coauthors, 2006: An AeroCom initial assessment – Optical properties in aerosol component modules of global models. *Atmospheric Chemistry and Physics*, **6 (7)**, 1815–1834, 10.5194/acp-6-1815-2006, URL http://www.atmos-chem-phys.net/6/1815/2006/.

Kishcha, P., A. M. da Silva, B. Starobinets, and P. Alpert, 2014: Air pollution over the Ganges basin and northwest Bay of Bengal in the early post-monsoon season based on NASA MERRAero data. *Journal of Geophysical Research: Atmospheres*, **119 (3)**, 1555–1570, 10.1002/2013JD020328, URL http://dx.doi.org/10.1002/2013JD020328.

Kohfeld, K. E., and S. P. Harrison, 2001: DIRTMAP: The geological record of dust. *Earth-Science Reviews*, **54 (1–3)**, 8–114, 10.1016/S0012-8252(01)00042-3, URL http://www.sciencedirect.com/science/article/pii/S0012825201000423.

Lana, A., and Coauthors, 2011: An updated climatology of surface dimethlysulfide concentrations and emission fluxes in the global ocean. *Global Biogeochemical Cycles*, **25 (1)**, 10.1029/2010GB003850, URL http://dx.doi.org/10.1029/2010GB003850.

Lary, D., L. A. Remer, D. MacNeil, B. Roscoe, and S. Paradise, 2010: Machine learning and bias correction of MODIS aerosol optical depth. *IEEE Geosci. Remote Sens. Lett.*, **6 (694)**, 10.1109/LGRS.2009.2023605, URL http://dx.doi.org/10.1109/LGRS.2009.2023605.

Levy, R. C., L. A. Remer, S. Mattoo, E. F. Vermote, and Y. J. Kaufman, 2007: Second-generation operational algorithm: Retrieval of aerosol properties over land from inversion of Moderate Resolution Imaging Spectroradiometer spectral reflectance. *Journal of Geophysical Research: Atmospheres*, **112 (D13)**, 10.1029/2006JD007811, URL http://dx.doi.org/10.1029/2006JD007811.

Liu, L., M. I. Mishchenko, I. Geogdzhayev, A. Smirnov, S. M. Sakerin, D. M. Kabanov, and O. A. Ershov, 2004: Global validation of two-channel AVHRR aerosol optical thickness retrievals over the oceans. *Journal of Quantitative Spectroscopy and Radiative Transfer*, **88 (1–3)**, 97–109, http://dx.doi.org/10.1016/j.jqsrt.2004.03.031, URL http://www.sciencedirect.com/science/article/pii/S0022407304001323.

Mahowald, N. M., and Coauthors, 2009: Atmospheric iron deposition: Global distribution, variability, and human perturbations. *Annu. Rev. Mar. Sci.*,, 245–278, 10.1146/annurev.marine.010908.163727, URL http://www.annualreviews.org/doi/abs/10.1146/annurev.marine.010908.163727?journalCode=marine.

Malm, W. C., B. A. Schichtel, and M. L. Pitchford, 2011: Uncertainties in PM2.5 gravimetric and speciation measurements and what we can learn from them. *Journal of the Air and Waste Management Association*, **61 (11)**, 1131–1149, 10.1080/10473289.2011.603998, URL http://doi.dx.org/10.1080/10473289.2011.603998.

Malm, W. C., J. F. Sisler, D. Huffman, R. A. Eldred, and T. A. Cahill, 1994: Spatial and seasonal trends in particle concentration and optical extinction in the United States. *Journal of Geophysical Research: Atmospheres*, **99 (D1)**, 1347–1370, 10.1029/93JD02916, URL http://onlinelibrary.wiley.com/doi/10.1029/93JD02916/full.

Maria, S. F., L. M. Russell, M. K. Gilles, and S. C. B. Myneni, 2004: Organic aerosol growth mechanisms and their climate-forcing implications. *Science*, **306 (5703)**, 1921–1924, 10.1126/science.1103491, URL http://www.sciencemag.org/content/306/5703/1921.abstract.

Marticorena, B., and G. Bergametti, 1995: Modeling the atmospheric dust cycle: 1. Design of a soil-derived dust emission scheme. *Journal of Geophysical Research: Atmospheres*, **100 (D8)**, 16 415–16 430, 10.1029/95JD00690, URL http://dx.doi.org/10.1029/95JD00690.

McCarty, W., 2016: MERRA-2: Observing system. Technical Report Series on Global Modeling and Data Assimilation 45, NASA Global Modeling and Assimilation Office. URL http://gmao.gsfc.nasa.gov/pubs/tm/docs/Bosilovich803.pdf.

McCormick, M. P., and T. J. Swissler, 1983: Stratospheric aerosol mass and latitudinal distribution of the El Chichón eruption cloud for October 1982. *Geophysical Research Letters*, **10 (9)**, 877–880, 10.1029/GL010i009p00877, URL http://dx.doi.org/10.1029/GL010i009p00877.

Meng, Z., P. Yang, G. W. Kattawar, L. Bi, K. N. Liou, and I. Laszlo, 2010: Single-scattering properties of tri-axial ellipsoidal mineral dust aerosols: A database for application to radiative transfer calculations. *J Aerosol Sci*, **41 (5)**, 501–512, 10.1016/j.jaerosci.2010.02.00, URL http://dx.doi.org/10.1016/j.jaerosci.2010.02.008.

Molod, A., L. Takacs, M. S. andJ. Bacmeister, I.-S. Song, and A. Eichmann, 2012: The GEOS-5 atmospheric general circulation model: Mean climate and development from MERRA to Fortuna. NASA Technical Report Series on Global Modeling and Data Assimilation NASA TM—2012-104606, NASA Global Modeling and Assimilation Office, 117 pp. URL http://gmao.gsfc.nasa.gov/pubs/docs/Molod484.pdf.

Molod, A., L. Takacs, M. Suarez, and J. Bacmeister, 2014: Development of the GEOS-5 atmospheric general circulation model: evolution from MERRA to MERRA-2. *Geosci. Model Dev. Discuss.*, **7**, 7575–7617, 10.5194/gmdd-7-7575-2014, URL http://dx.doi.org/10.5194/gmdd-7-7575-2014.

Muller, D., and Coauthors, 2014: Airborne multiwavelength High Spectral Resolution Lidar (HSRL-2) observations during TCAP 2012: Vertical profiles of optical and microphysical properties of a smoke/urban haze plume over the northeastern coast of the US. *Atmos. Meas. Tech. Discuss.*, **7 (2)**, 1059–1973, 10.5194/amtd-7-1059-2014, URL http://dx.doi.org/10.5194/amtd-7-1059-2014.

Nowottnick, E., P. Colarco, A. da Silva, D. Hlavka, and M. McGill, 2011: The fate of Saharan dust across the Atlantic and implications for a Central American dust barrier. *Atmospheric Chemistry and Physics*, **11 (16)**, 8415–8431, 10.5194/acp-11-8415-2011, URL http://www.atmos-chem-phys.net/11/8415/2011/.

Nowottnick, E. P., P. R. Colarco, E. J. Welton, and A. da Silva, 2015: Use of the CALIOP vertical feature mask for evaluating global aerosol models. *Atmospheric Measurement Techniques*, **8 (9)**, 3647–3669, 10.5194/amt-8-3647-2015, URL http://www.atmos-meas-tech.net/8/3647/2015/.

O'Neill, N., A. Ignatov, B. N. Holben, and T. F. Eck, 2000: The lognormal distribution as a reference for reporting aerosol optical depth statistics: Empirical tests using multi-year, multi-site AERONET Sunphotometer data. *Geophysical Research Letters*, **27 (20)**, 3333–3336, 10.1029/2000GL011581, URL http://onlinelibrary.wiley.com/doi/10.1029/2000GL011581/abstract.

Pan, X., and Coauthors, 2015: A multi-model evaluation of aerosols over South Asia: Common problems and possible causes. *Atmospheric Chemistry and Physics*, **15 (10)**, 5903–5928, 10.5194/acp-15-5903-2015, URL http://www.atmos-chem-phys.net/15/5903/2015/.

Pitari, G., and Coauthors, 2014: Stratospheric ozone response to sulfate geoengineering: Results from the Geoengineering Model Intercomparison Project (GeoMIP). *Journal of Geophysical Research: Atmospheres*, **119 (5)**, 2629–2653, 10.1002/2013JD020566, URL http://dx.doi.org/10.1002/2013JD020566.

Pope, C. A., and D. W. Dockery, 110: Air pollution and life expectancy in China and beyond. *Proceedings of the National Academy of Sciences*, **32 (12861–12862)**, 10.1073/pnas.1310925110, URL http://www.pnas.org/content/110/32/12861.

Pope III, C. A., M. Ezzati, and D. W. Dockery, 2009: Fine particulate air pollution and life expectancy in the United States. *New England Journal of Medicine*, **360 (4)**, 376–386, 10.1056/NEJMsa0805646, URL http://www.nejm.org/doi/full/10.1056/NEJMsa0805646.

Prospero, J. M., 1996: *The Atmospheric Transport of Particles to the Ocean, In: Particle Flux in the Ocean.* John Wiley and Sons Ltd., New York.

Prospero, J. M., M. Uematsu, and D. L. Savoie, 1989: *Mineral aerosol transport to the Pacific Ocean*, Vol. 10, 187–218. Academic Press, New York.

Randerson, J. T., and Coauthors, 2006: The impact of boreal forest fire on climate warming. *Science*, **314 (5802)**, 1130–1132, 10.1126/science.1132075, URL http://www.sciencemag.org/content/314/5802/1130.abstract.

Randles, C. A., P. R. Colarco, and A. da Silva, 2013: Direct and semi-direct aerosol effects in the NASA GEOS-5 AGCM: aerosol-climate interactions due to prognostic versus prescribed aerosols. *Journal of Geophysical Research: Atmospheres*, **118 (1)**, 149–169, 10.1029/2012JD018388, URL http://dx.doi.org/10.1029/2012JD018388.

Randles, C. A., and Coauthors, 2016: Use of the NASA GEOS-5 SEAC[4]RS meteorological and aerosol reanalysis for assessing simulated aerosol optical properties as a funciton of smoke age, in preparation for Journal of Geophysical Research.

Read, W. G., L. Froidevaux, and J. W. Waters, 1993: Microwave Limb Sounder measurement of stratospheric SO_2 from the Mt. Pinatubo volcano. *Geophysical Research Letters*, **20 (12)**, 1299–1302, 10.1029/93GL00831, URL http://onlinelibrary.wiley.com/doi/10.1029/93GL00831/full.

Reale, O., K. M. Lau, A. da Silva, and T. Matsui, 2014: Impact of assimilated and interactive aerosol on tropical cyclogenesis. *Geophysical Research Letters*, **41 (9)**, 3282–3288, 10.1002/2014GL059918, URL http://dx.doi.org/10.1002/2014GL059918.

Reichle, R. H., and Q. Liu, 2014: Observation-corrected precipitation estimates in GEOS-5. Tech. rep., NASA. URL http://gmao.gsfc.nasa.gov/pubs/docs/Reichle734.pdf.

Reid, J. S., and Coauthors, 2003: Comparison of size and morphological measurements of coarse mode dust particles from Africa,. *Journal of Geophysical Research: Atmospheres*, **108 (D19)**, 8593, 10.1029/2002JD002485, URL http://onlinelibrary.wiley.com/doi/10.1029/2002JD002485/full.

Remer, L. A., and Coauthors, 2005: The MODIS aerosol algorithm, products, and validation. *Journal of the Atmospheric Sciences*, **62**, 947–973, 10.1175/JAS3385.1, URL http://dx.doi.org/10.1175/JAS3385.1.

Remer, L. A., and Coauthors, 2008: Global aerosol climatology from the MODIS satellite sensors. *Journal of Geophysical Research: Atmospheres*, **113 (D14)**, 10.1029/2007JD009661, URL http://dx.doi.org/10.1029/2007JD009661.

Rienecker, M. M., M. J. Suarez, R. Todling, and Coauthors, 2008: The GEOS-5 Data Assimilation System – Documentation of versions 5.0.1, 5.1.0, and 5.2.0. Tech. rep., NASA Global Modeling and Assimilation Offic. URL http://gmao.gsfc.nasa.gov/pubs/docs/Rienecker369.pdf.

Rienecker, M. M., and Coauthors, 2011: MERRA: NASA's Modern-Era Retrospective analysis for Research and Applications. *Journal of Climate*, **24**, 3624–3648, 10.1175/JCLI-D-11-00015.1, URL http://dx.doi.org/10.1175/JCLI-D-11-00015.1.

Robock, A., 2000: Volcanic eruptions and climate. *Review of Geophysics*, **28 (2)**, 191–219, doi: 10.1029/1998RG000054, URL http://dx.doi.org/10.1029/1998RG000054.

Saide, P. E., G. R. Carmichael, Z. Liu, C. S. Schwartz, H. C. Lin, A. M. da Silva, and E. Hyer, 2013: Aerosol optical depth assimilation for a size-resolved sectional model: Impacts of observationally constrained, multi-wavelength and fine mode retrievals on regional scale analyses and forecasts. *Atmospheric Chemistry and Physics*, **13**, 10 425–10 444, doi:10.5194/acp-13-10425-2013, URL http://dx.doi.org/10.5194/acp-13-10425-2013.

Schutgens, N. A. J., T. Miyoshi, T. Takemura, and T. Nakajima, 2010: Applying an ensemble Kalman filter to the assimilation of AERONET observations in a global aerosol transport model. *Atmospheric Chemistry and Physics*, **10 (5)**, 2561–2576, 10.5194/acp-10-2561-2010, URL http://www.atmos-chem-phys.net/10/2561/2010/.

Schwarz, J. P., R. S. Gao, D. W. Fahey, D. S. Thomson, L. A. Watts, and J. C. Wilson, 2006: Single-particle measurements of midlatitude black carbon and light-scattering aerosols from the boundary layer to the lower stratosphere. *Journal of Geophysical Research*, **111 (D16) (D16207)**, 10.1029/2006JD007076, URL http://dx.doi.org/10.1029/2006JD007076.

Schwarz, J. P., and Coauthors, 2010: Global-scale black carbon profiles observed in the remote atmosphere and compared to models. *Geophysical Research Letters*, **L18812**, 10.1029/2010GL044372, URL http://dx.doi.org/10.1029/2010GL044372.

Schwarz, J. P., and Coauthors, 2013: Global-scale seasonally resolved black carbon vertical profiles over the Pacific. *Geophysical Research Letters*, **40 (20)**, 5542–5547, 10.1002/2013GL057775, URL http://dx.doi.org/10.1002/2013GL057775.

Scott, 1992: *Multivariate Density Estimation: Theory, Practice, and Visualization*. Wiley.

Segal-Rosenheimer, M., and Coauthors, 2014: Tracking elevated pollution layers with a newly developed HyperSpectral Sun/Sky spectrometer (4STAR): Results from the TCAP 2012 and 2013 campaigns. *J. Geophys. Res.*, **119 (5)**, 10.1002/2013jd020884, URL http://dx.doi.org/10.1002/2013jd020884.

Shi, Y., J. Zhang, J. S. Reid, B. Holben, E. J. Hyer, and C. Curtis, 2011: An analysis of the collection 5 MODIS over-ocean aerosol optical depth product for its implication in aerosol assimilation. *Atmospheric Chemistry and Physics*, **11 (2)**, 557–565, 10.5194/acp-11-557-2011, URL http://www.atmos-chem-phys.net/11/557/2011/.

Shinozuka, Y., and Coauthors, 2013: Hyperspectral aerosol optical depths from TCAP flights. *J. Geophys. Res.*, **118**, 1–15, doi:10.1002/2013jd020596, URL http://dx.doi.org/10.1002/2013jd020596.

Silverman, B. W., 1986: *Density Estimation.* Chapman and Hall, London.

Slowik, J. G., and Coauthors, 2007: An inter-comparison of instruments measuring black carbon content of soot particles. *Aerosol Science and Technology*, **41 (295-314)**, 10.1080/02786820701197078, URL http://www.tandfonline.com/doi/abs/10.1080/02786820701197078.

Smirnov, A., 2000: Cloud-screening and quality control algorithms for the AERONET database. *Remote Sensing of Environment*, **73 (3)**, 337 – 349, http://dx.doi.org/10.1016/S0034-4257(00)00109-7, URL http://www.sciencedirect.com/science/article/pii/S0034425700001097.

Smirnov, A., B. N. Holben, Y. J. Kaufman, O. Dubovik, T. F. Eck, I. Slutsker, C. Pietras, and R. N. Halthore, 2002: Optical properties of atmospheric aerosol in maritime environments. *Journal of the Atmospheric Sciences*, **59**, 501–523, 10.1175/1520-0469(2002)059<0501:OPOAAI>2.0.CO;2, URL http://dx.doi.org/10.1175/1520-0469(2002)059<0501:OPOAAI>2.0.CO;2.

Smirnov, A., and Coauthors, 2009: Maritime Aerosol Network as a component of Aerosol Robotic Network. *Journal of Geophysical Research: Atmospheres*, **114 (D06204)**, 10.1029/2008JD011257, URL http://dx.doi.org/10.1029/2008JD011257.

Spurr, R., 2006: VLIDORT: A linearized pseudo-spherical vector dis- crete ordinate radiative transfer code for forward model and retrieval studies in multilayer multiple scattering media. *Journal of Quantatative Spectroscopy*, **102**, 316–342, 10.1016/j.jqsrt.2006.05.005, URL http://www.sciencedirect.com/science/article/pii/S0022407306001191.

Stenchikov, G. L., I. Kirchner, A. Robock, H.-F. Graf, J. C. Antuna, R. G. Grainger, A. Lambert, and L. Thomason, 1998: Radiative forcing from the 1991 Mount Pinatubo volcanic eruption. *Journal of Geophysical Research: Atmospheres*, **103 (D12)**, 13 837–13 857, 10.1029/98JD00693, URL http://onlinelibrary.wiley.com/doi/10.1029/98JD00693/abstract.

Streets, D. G., C. Yu, Y. Wu, M. Chin, Z. Zhao, T. Hayasaka, and G. Shi, 2008: Aerosol trends over China, 1980–2000. *Atmospheric Research*, **88 (2)**, 174–182, 10.1016/j.atmosres.2007.10.016, URL http://www.sciencedirect.com/science/article/pii/S0169809507001949.

Streets, D. G., and Coauthors, 2009: Anthropogenic and natural contributions to regional trends in aerosol optical depth, 1980–2006. *Journal of Geophysical Research: Atmospheres*, **114 (D10)**, 10.1029/2008JD011624, URL http://dx.doi.org/10.1029/2008JD011624.

Takacs, L. L., M. J. Suarez, and R. Todling, 2015: Maintaining atmospheric mass and water balance within reanalysis. Tech. rep., NASA Global Modeling and Assimilation Office. URL http://gmao.gsfc.nasa.gov/pubs/docs/Takacs737.pdf.

Tegen, I., S. P. Harrison, K. Kohfeld, I. C. Prentice, M. Coe, and M. Heimann, 2002: Impact of vegetation and preferential source areas on global dust aerosol: Results from a model study. *Journal of Geophysical Research: Atmospheres*, **107 (D21)**, 10.1029/2001JD000963, URL http://dx.doi.org/10.1029/2001JD000963.

Textor, C., and Coauthors, 2006: Analysis and quantification of the diversities of aerosol life cycles within AeroCom. *ACP*, **6 (7)**, 1777–1813, 10.5194/acp-6-1777-2006, URL http://www.atmos-chem-phys.net/6/1777/2006/.

Torres, O., C. Ahn, and Z. Chen, 2013: Improvements to the OMI near-UV aerosol algorithm using A-train CALIOP and AIRS observations. *Atmospheric Measurement Techniques*, **6 (11)**, 3257–3270, 10.5194/amt-6-3257-2013, URL http://www.atmos-meas-tech.net/6/3257/2013/.

Torres, O., P. K. Bhartia, J. Herman, Z. Ahmad, and J. Gleason, 1998: Derivation of aerosol properties from satellite measurements of backscattered ultraviolet radiation: Theoretical basis. *Journal of Geophysical Research*, **103**, 17 099–17 110, 10.1029/98JD00900, URL http://onlinelibrary.wiley.com/doi/10.1029/98JD00900/full.

Torres, O., A. Tanskanen, B. Veihelmann, C. Ahn, R. Braak, P. K. Bhartia, P. Veefkind, and P. Levelt, 2007: Aerosols and surface UV products from Ozone Monitoring Instrument observations: An overview. *Journal of Geophysical Research*, **112 (D24S47)**, 10.1029/2007JD008809, URL http://onlinelibrary.wiley.com/doi/10.1029/2007JD008809/abstract.

van der Werf, G. R., J. T. Randerson, L. Giglio, G. J. Collatz, P. S. Kasibhatla, and A. F. Arellano Jr., 2006: Interannual variability in global biomass burning emissions from 1997 to 2004. *Atmospheric Chemistry and Physics*, **6 (11)**, 3423–3441, 10.5194/acp-6-3423-2006, URL http://www.atmos-chem-phys.net/6/3423/2006/.

Winker, D. M., W. H. Hunt, and M. J. McGill, 2007: Initial performance assessment of CALIOP. *Geophys. Res. Lett.*, **L19803 (34)**, 10.1029/2007GL030135, URL http://dx.doi.org/10.1029/2007GL030135.

Winker, D. M., M. A. Vaughan, A. Omar, Y. Hu, K. A. Powell, Z. Liu, W. H. Hunt, and S. A. Young, 2009: Overview of the CALIPSO mission and CALIOP data processing algorithms. *Journal of Atmospheric and Oceanic Technology*, **26 (11)**, 2310–2323., 10.1175/2009JTECHA1281.1, URL http://dx.doi.org/10.1175/2009JTECHA1281.1.

Wiscombe, W. J., 1980: Improved Mie scattering algorithms. *Appl. Opt.*, **19 (9)**, 1505–1509, 10.1364/AO.19.001505, URL http://ao.osa.org/abstract.cfm?URI=ao-19-9-1505.

Wofsy, S. C., and Coauthors, 2011: HIAPER Pole-to-Pole Observations (HIPPO): Fine-grained, global-scale measurements of climatically important atmospheric gases and aerosols. *Phil. Trans. Math. Phys. Eng. Sci.*, **369 (1943)**, 2073–2086, 10.1098/rsta.2010.0313, URL http://dx.doi.org/10.1098/rsta.2010.0313.

Yasunari, T. J., and Coauthors, 2014: The GOddard SnoW Impurity Module (GOSWIM) for the NASA GEOS-5 Earth System Model: Preliminary comparisons with observations in Sapporo, Japan. *SOLA*, **10**, 50–56, 10.2151/sola.2014-011, URL http://dx.doi.org/10.2151/sola.2014-011.

Zhang, J., J. R. Campbell, E. J. Hyer, J. S. Reid, D. L. Westphal, and R. S. Johnson, 2014: Evaluating the impact of multisensor data assimilation on a global aerosol particle transport model. *Journal of Geophysical Research: Atmospheres*, **119 (8)**, 4674–4689, 10.1002/2013JD020975, URL http://dx.doi.org/10.1002/2013JD020975.

Zhang, J., and J. S. Reid, 2006: Modis aerosol product analysis for data assimilation: Assessment of over-ocean Level 2 aerosol optical thickness retrievals. *Journal of Geophysical Research: Atmospheres*, **111 (D22)**, 10.1029/2005JD006898, URL http://dx.doi.org/10.1029/2005JD006898.

Zhang, J., and J. S. Reid, 2009: An analysis of clear sky and contextual biases using an operational over ocean MODIS aerosol product. *Geophysical Research Letters*, **36 (15)**, 10.1029/2009GL038723, URL http://dx.doi.org/10.1029/2009GL038723.

Zhang, J., J. S. Reid, D. L. Westphal, N. L. Baker, and E. J. Hyer, 2008: A system for operational aerosol optical depth data assimilation over global oceans. *Journal of Geophysical Research: Atmospheres*, **113 (D10)**, 10.1029/2007JD009065, d10208.

Zhang, Y., M. Bocquet, V. Mallet, C. Seigneur, and A. Baklanov, 2012: Real-time air quality forecasting, Part I: History, techniques, and current status. *Atmospheric Environment*, **60**, 632–655, 10.1016/j.atmosenv.2012.06.031, URL http://www.sciencedirect.com/science/article/pii/S1352231012005900.

Appendices

Appendix A

Acronyms

4STAR   Spectrometer for Sky-Scanning, Sun-Tracking Atmospheric Research

AAOD   Aerosol Absorption Optical Depth

AEAP   Atmospheric Effects of Aviation Program

AeroCom   AEROsol COMparisons between Observations and Models

AERONET   AEROsol RObotic NETwork

ADAS   atmospheric data assimilation system

AI   Aerosol Index

AN   ammonium nitrate

AOD   aerosol optical depth

AQS   Air Quality System

ARCTAS   Arctic Research of the Composition of the Troposphere from Aircraft and Satellites

AS   ammonium sulfate

ATSR   Dunno acronym

AVHRR   Advanced Very High Resolution Spectroradiometer

BC   black carbon

CALIOP   Cloud Aerosol Lidar with Orthogonal Polarization

CARB   California Air Resources Board

CASA   Carnegie-Ames-Stanford Approach

CDR   Climate Data Record

CPC   Climate Prediction Center

CSN   Chemical Speciation Network

DIAL   DIfferential Absorption Lidar

DIRTMAP   Dust Indicators and Records in Terrestrial and Marine Paleoenvironments

DISC   Data and Information Services Center

DISCOVER-AQ   Deriving Information on Surface Conditions from COlumn and VERtically Resolved Observations Relevant to Air Quality

DMS   di-methyl sulfide

DU   dust

EANET   Acid Deposition Monitoring Network in East Asia

EDGAR   Emissions Database for Global Atmospheric Research

EOS   Earth Observing System

EPA   Environmental Protection Agency

FRP   Fire Radiative Power

GAAS   Goddard Aerosol Assimilation System

GES   Goddard Earth Sciences

GEOS   Goddard Earth Observing System

GEOS-5   Goddard Earth Observing System Model, Version 5

GFED   Global Fire Emissions Database, Version 3.1

GMAO   Global Modeling and Assimilation Office

GPS　　　　Global Positioning Satellite

GOCART　　Goddard Chemistry, Aerosol, Radiation, and Transport model

HFED　　　historical, homogenized emissions database

HIPPO　　　HIAPER Pole-to-Pole Observations of Carbon Cycle and Greenhouse Gases Study

HSRL　　　High Spectral Resolution Lidar

IESA　　　Integrated Earth System Analysis

IMPROVE　Interagency Monitoring of Protected Visual Environments

LaRC　　　NASA Langley Research Center

LDE　　　Local Displacement Ensembles

LER　　　Lambertian Equivalent Reflectivity

LUTs　　　look-up tables

NASA　　　National Aeronautics and Space Administration

NOAA　　　National Oceanic and Atmospheric Administration

MAN　　　Maritime Aerosol Network

MERRA　　Modern-Era Retrospective analysis for Research and Applications

MERRAero　MERRA Aerosol Reanalysis

MERRA-2　Modern-Era Retrospective analysis for Research and Applications, Version 2

MISR　　　Multi-angle Imaging SpectroRadiometer

MLS　　　Microwave Limb Sounder

MODIS　　MODerate Resolution Imaging Spectroradiometer

MSA　　　methane sulfonic acid

NNR　　　Neural Net Retrieval

NOAA　　　National Oceanic and Atmospheric Administration

NRT　　　Near Real Time

OC   organic carbon

OMI   Ozone Monitoring Instrument

OPAC   Optical Properties of Aerosols and Clouds

OSSE   Observing System Simulation Experiment

PATMOS-x Pathfinder Atmosphere-Extended

PBL   Planetary Boundary Layer

PDF   probability distribution function

POES   Polar Operational Environmental Satellites

POM   Particulate Organic Matter

QFED   Quick Fire Emissions Dataset

RETRO   REanalysis of the TROpospheric chemical composition over the past 40 years

RETROv2   REanalysis of the TROpospheric chemical composition over the past 40 years, Version 2

RCFM   Reconstructed Fine Mass

rBC   refractory black carbon

RMS   root mean square of the difference

RSMAS   Rosenstiel School of Marine and Atmospheric Science

SAGE-II   Stratospheric Aerosol and Gas Experiment II

SEAREX   Sea/Air Exchange

SOI   Southern Oscillation Index

SP2   Single Particle Soot Absorption Photometer

SS   sea salt

STDV   standard deviation of the differences

TOA   top-of-the atmosphere

TOMS Total Ozone Mapping Spectrometer

UV ultra-violet

VLIDORT Vector LInearized Discrete Ordinate Radiative Transfer

Appendix B

Regional Timeseries
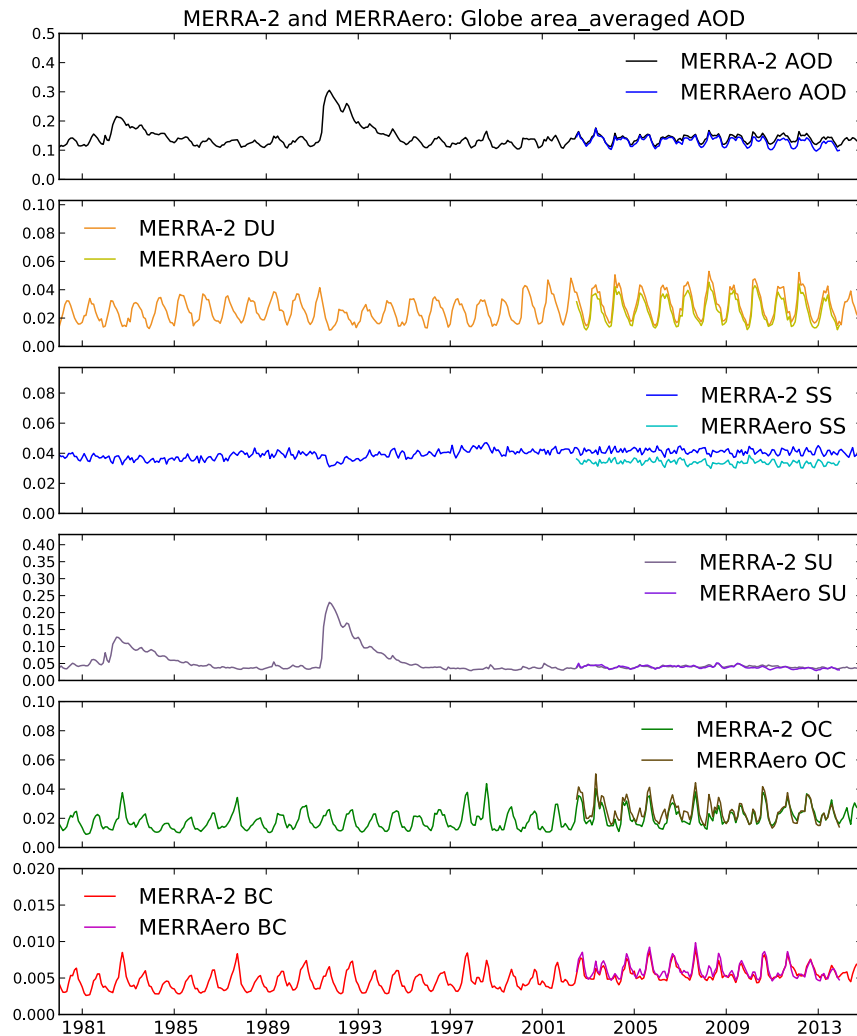
Figure B.1: Global-average, area-weighted monthly-mean time series of (from top to bottom) total AOD, dust AOD, sea salt AOD, sulfate AOD, organic carbon AOD, and black carbon AOD from MERRA-2 and MERRAero.
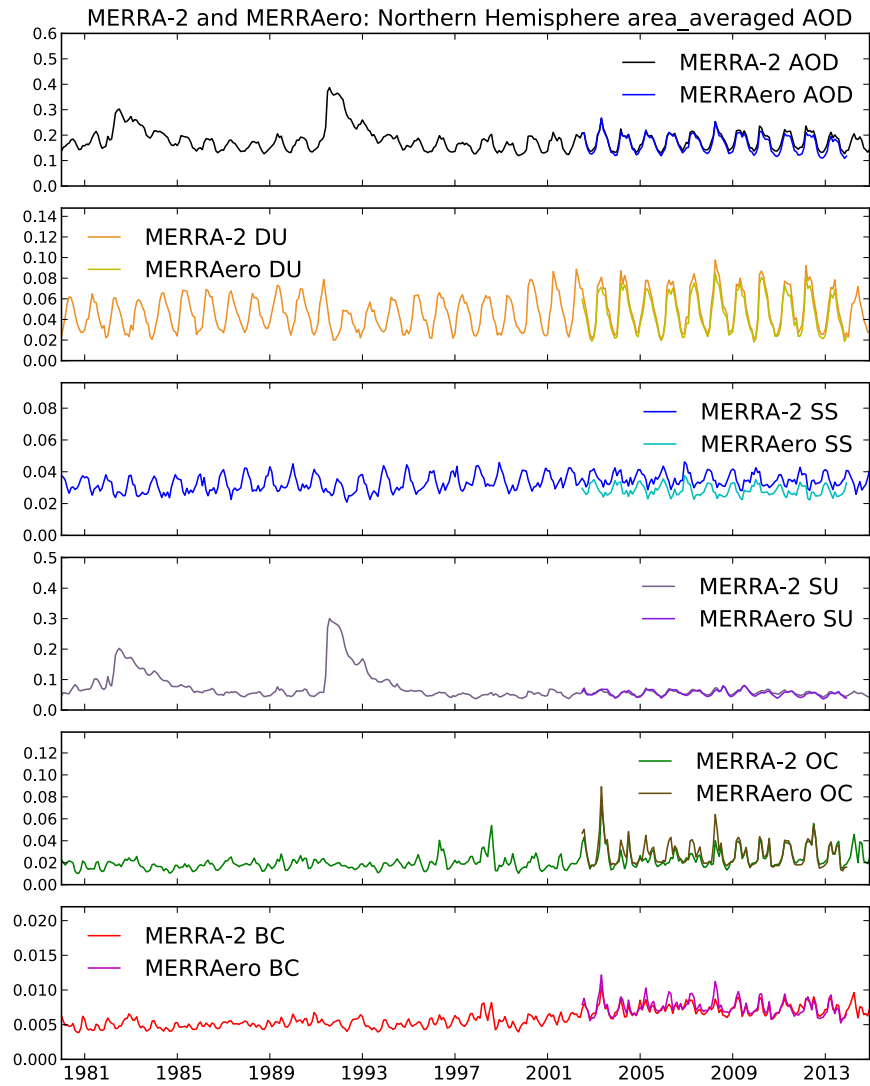
Figure B.2: Same as Fig. B.1 except in the Northern Hemisphere.
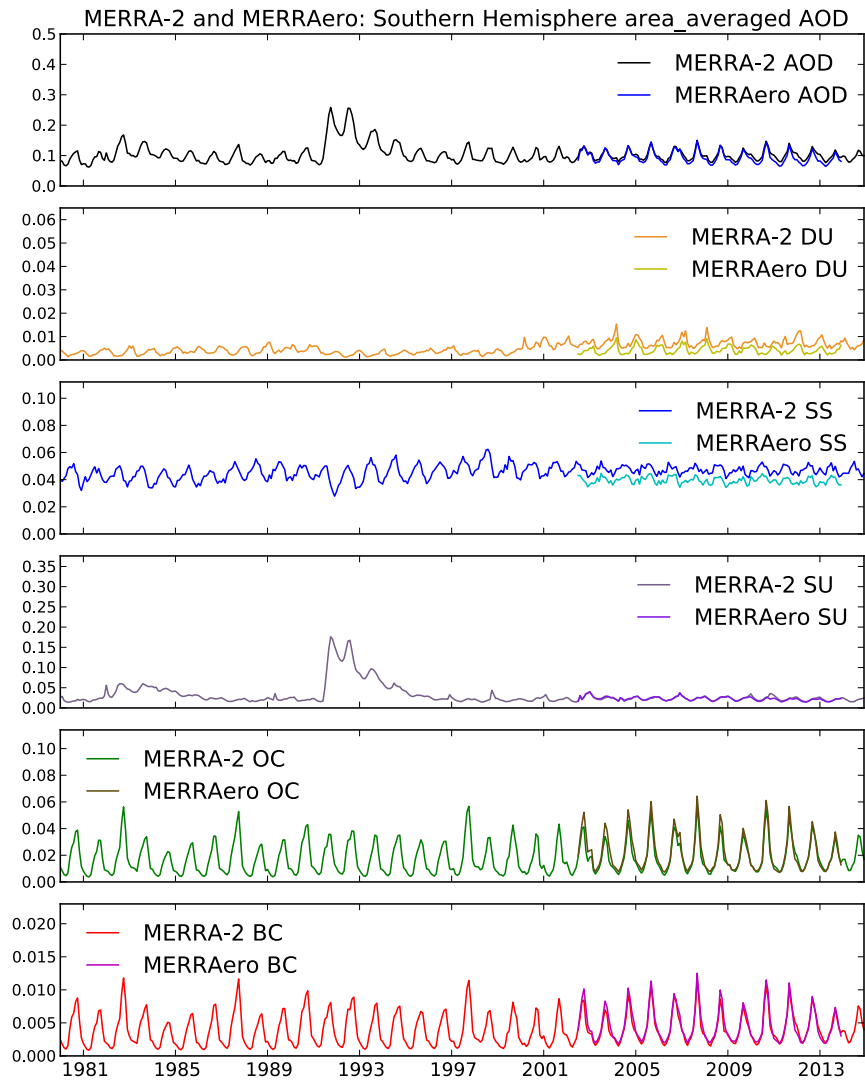
Figure B.3: Same as Fig. B.1 except in the Southern Hemisphere.
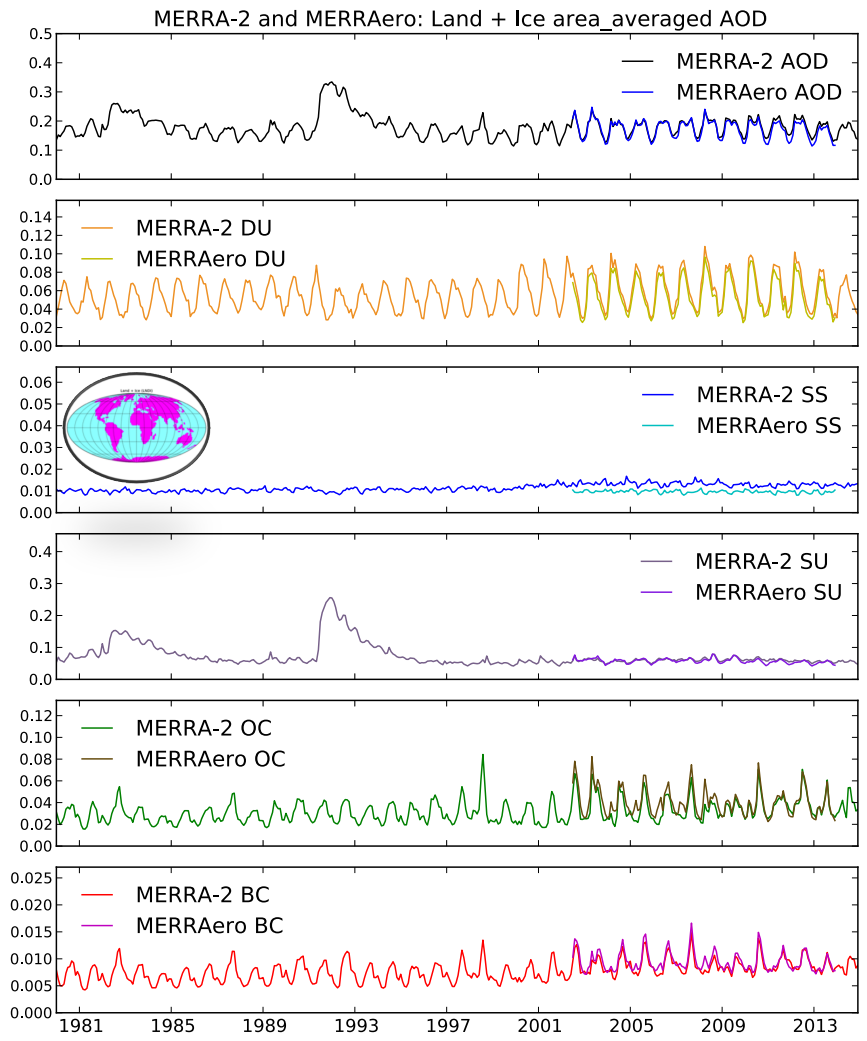
Figure B.4: Same as Fig. B.1 except over all land (see magenta highlighted region in inset map).
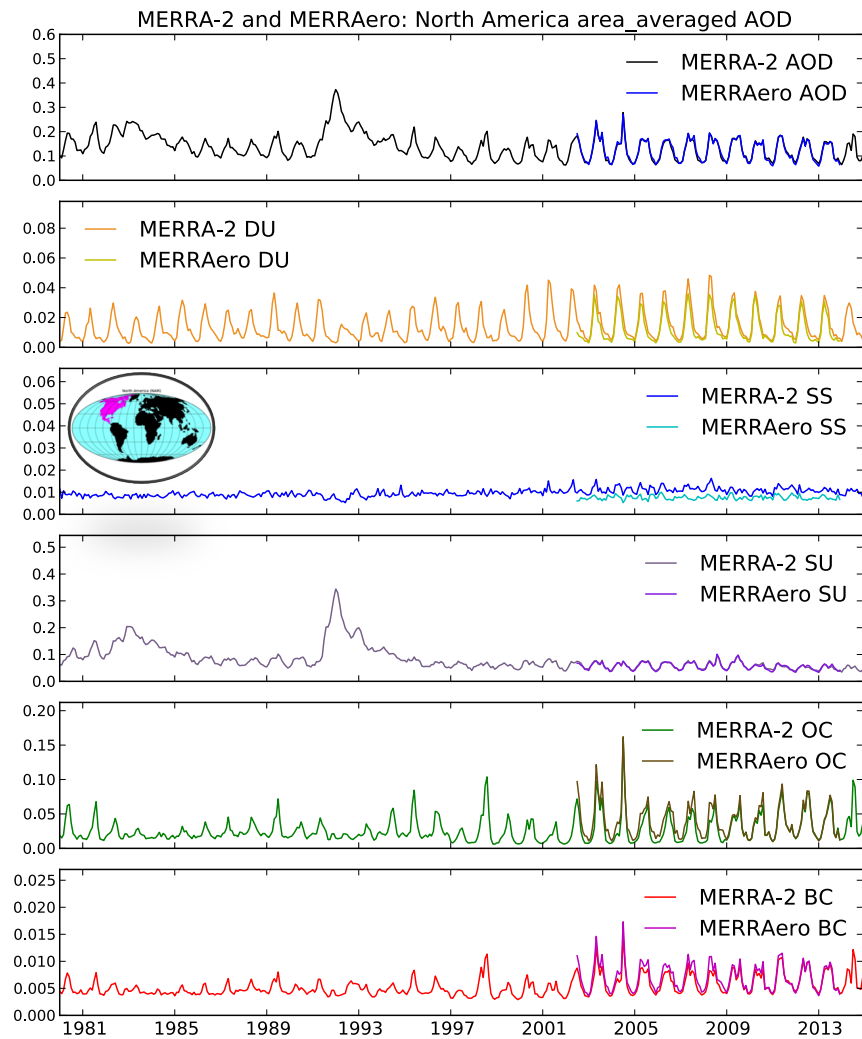
Figure B.5: Same as Fig. B.1 except over North America (see magenta highlighted region in inset map).
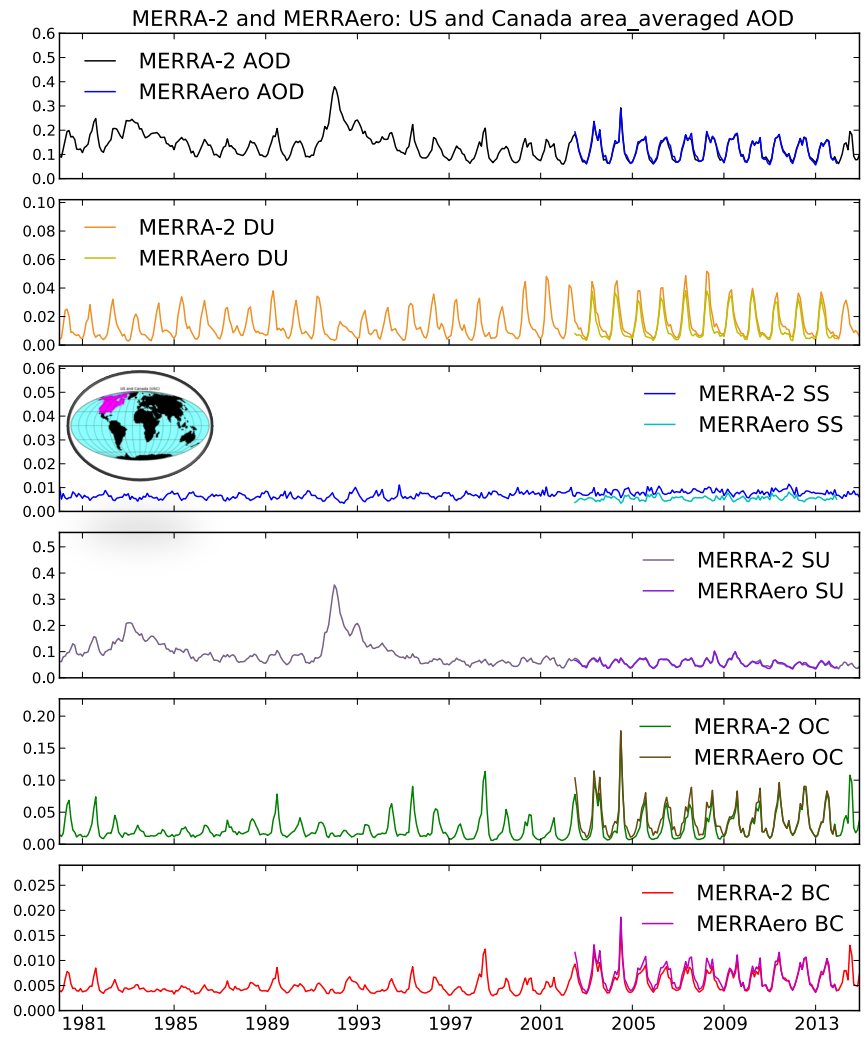
Figure B.6: Same as Fig. B.1 except over Canada and the United States (see magenta highlighted region in inset map).
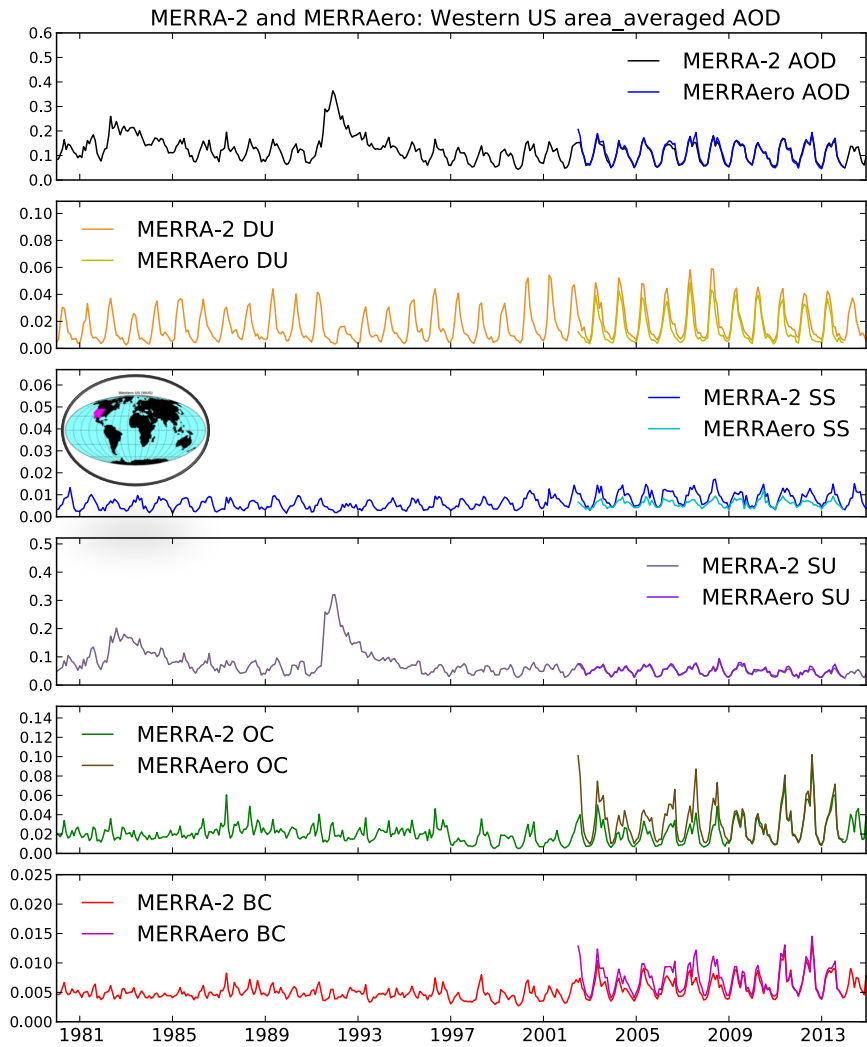
Figure B.7: Same as Fig. B.1 except over the western United States (see magenta highlighted region in inset map).
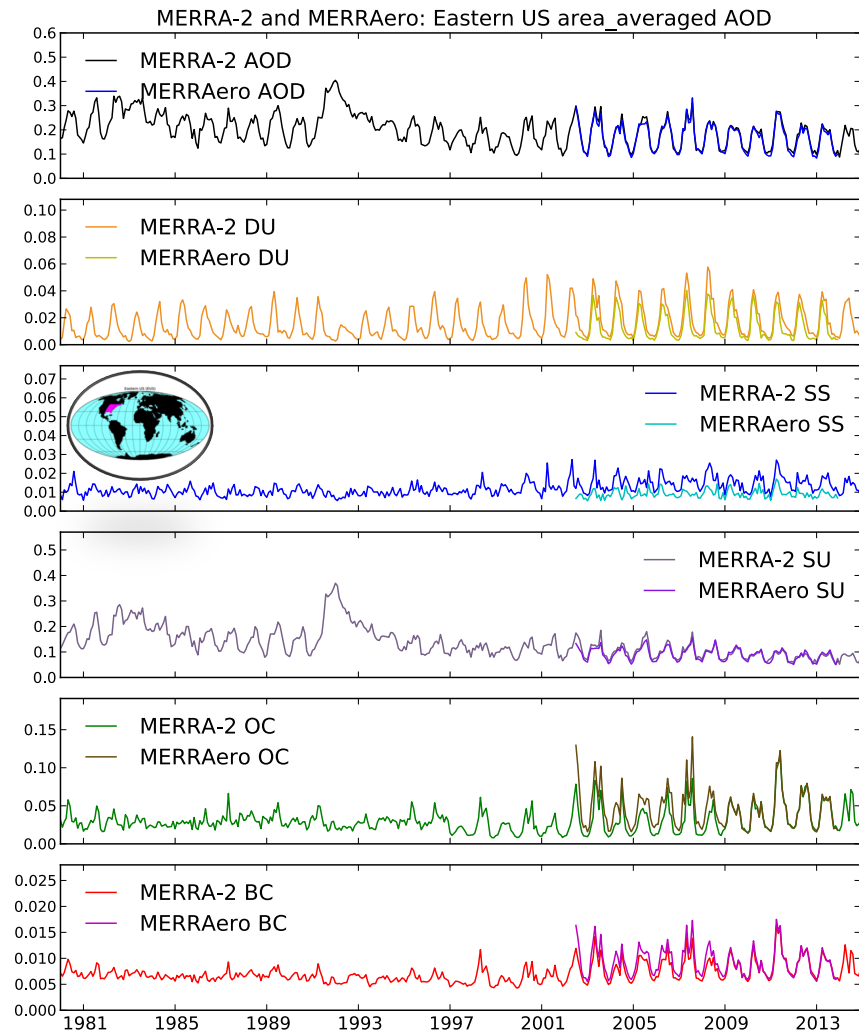
Figure B.8: Same as Fig. B.1 except over the eastern United States (see magenta highlighted region in inset map).
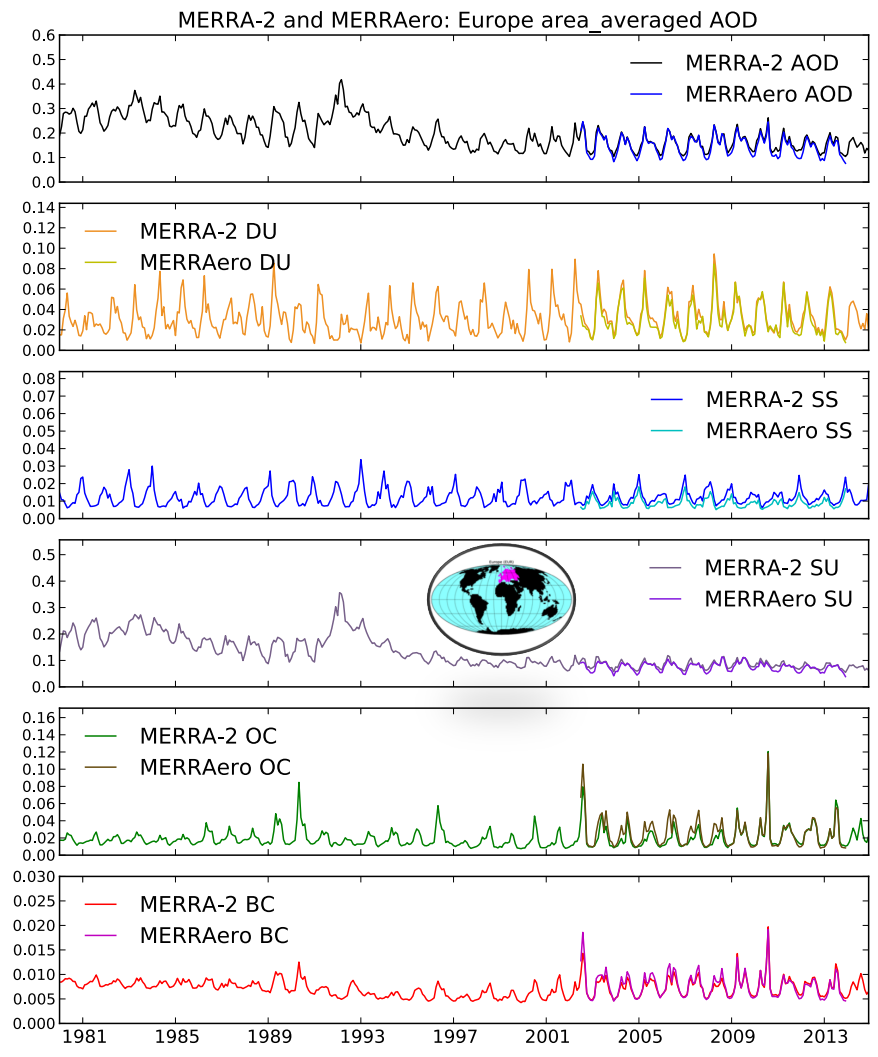
Figure B.9: Same as Fig. B.1 except over Europe (see magenta highlighted region in inset map).
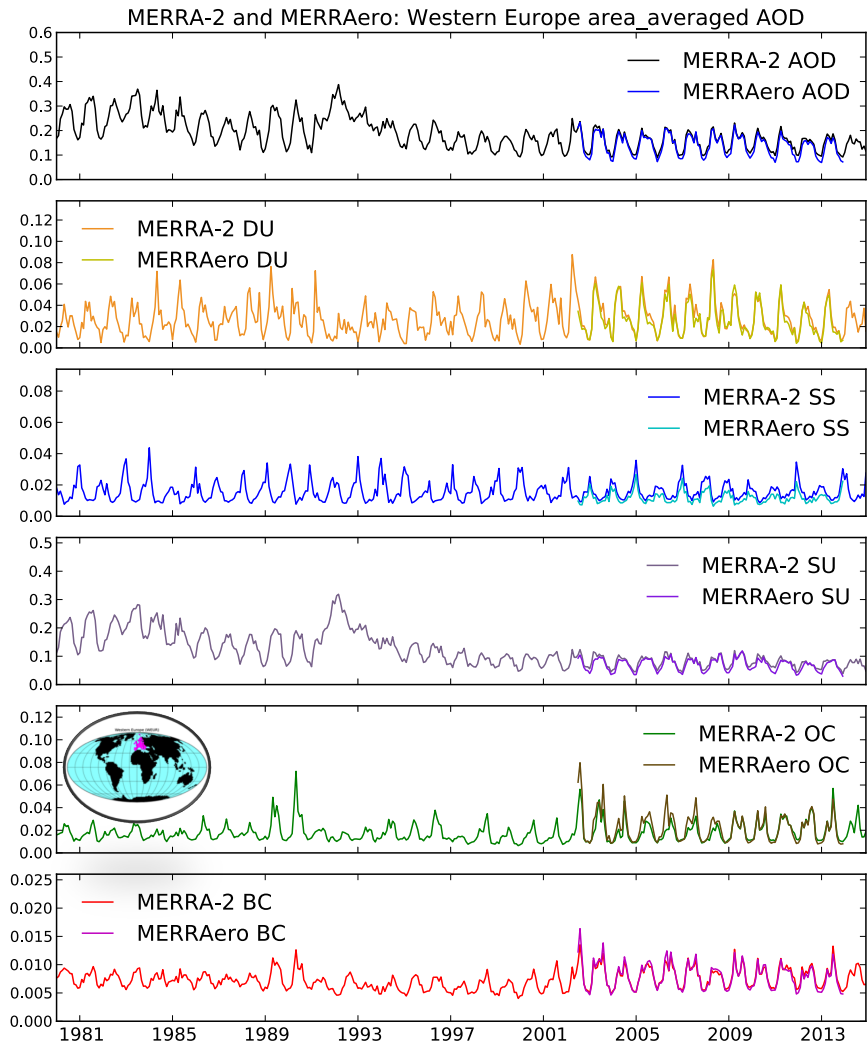
Figure B.10: Same as Fig. B.1 except over western Europe (see magenta highlighted region in inset map).
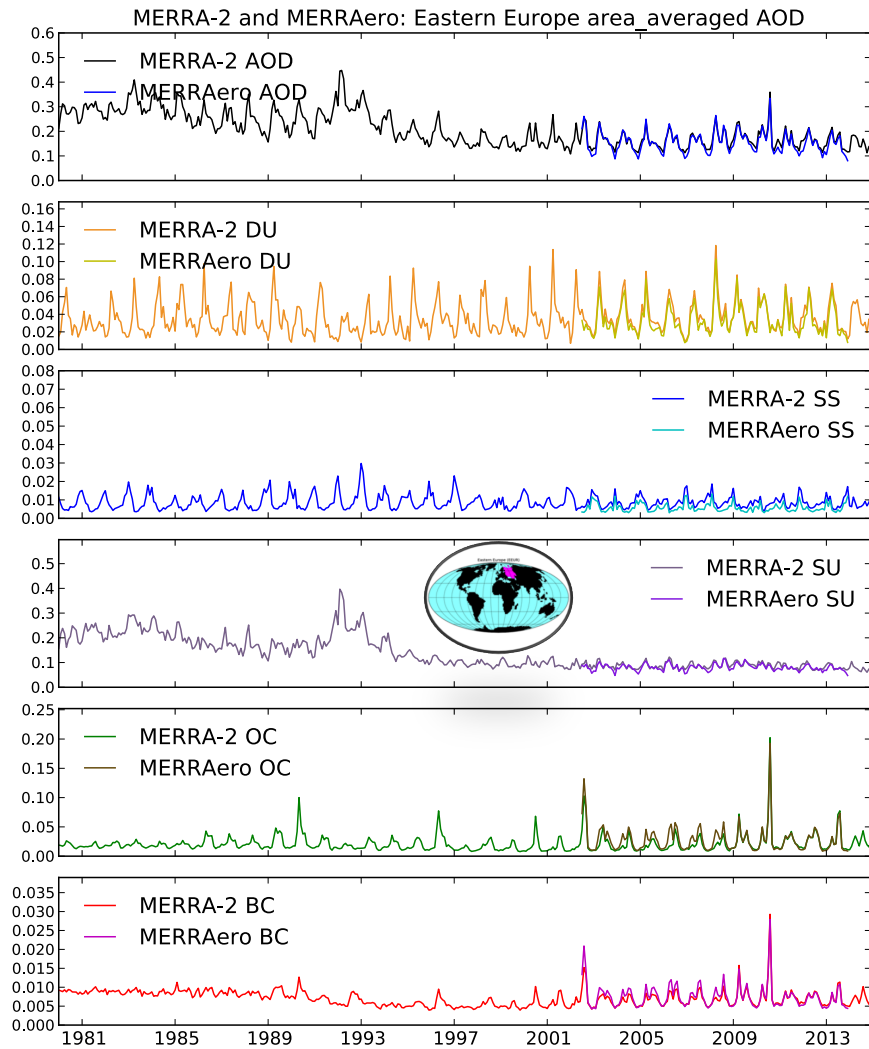
Figure B.11: Same as Fig. B.1 except over eastern Europe (see magenta highlighted region in inset map).
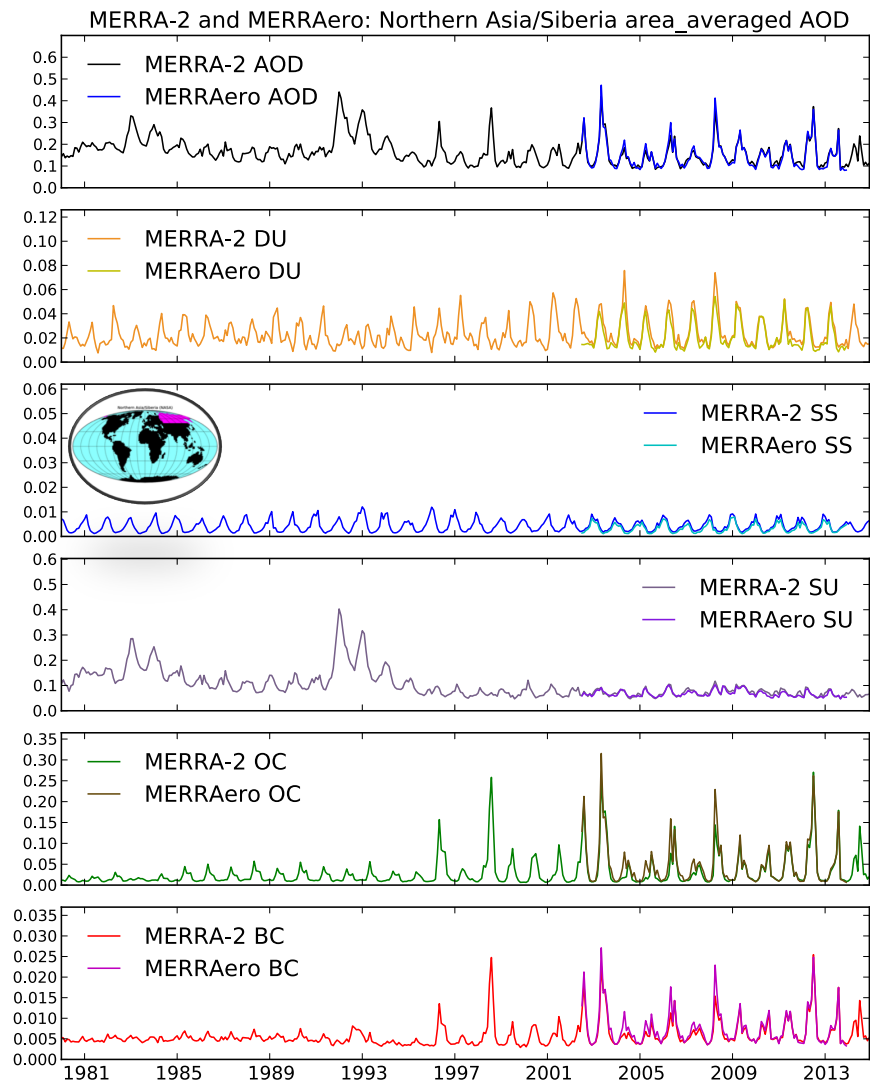
Figure B.12: Same as Fig. B.1 except over northern Asia/Siberia (see magenta highlighted region in inset map).
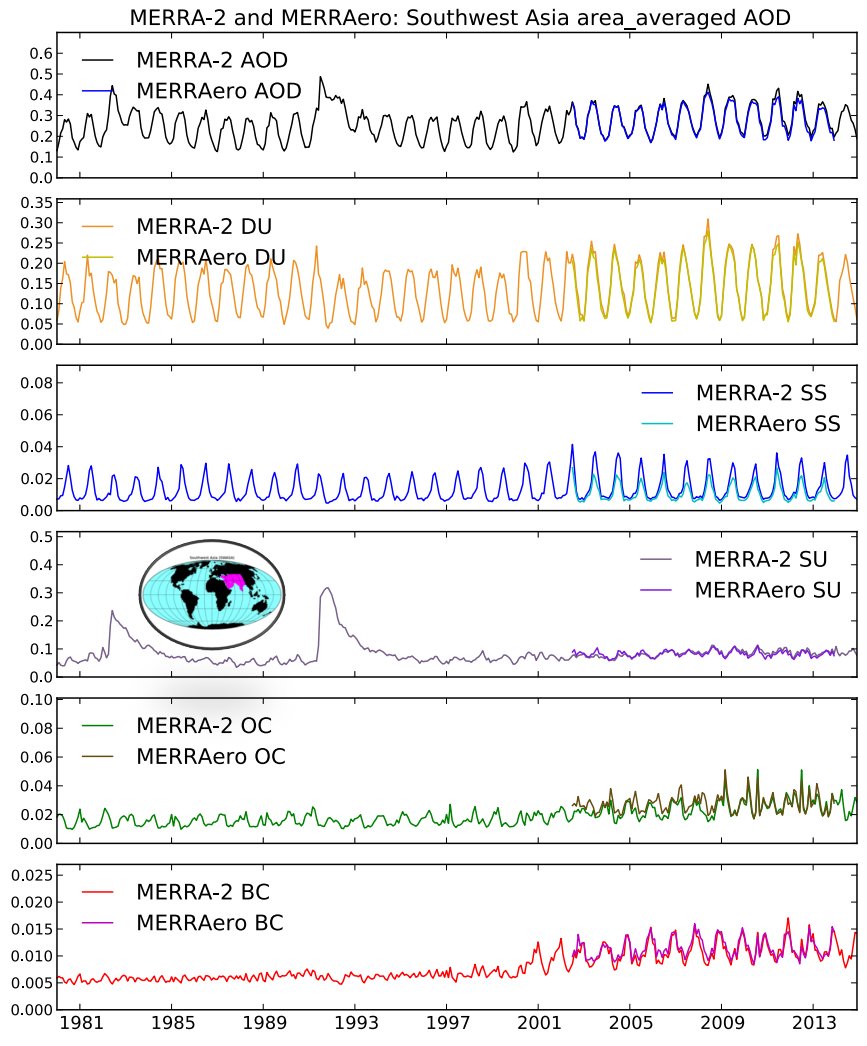
Figure B.13: Same as Fig. B.1 except over the Middle East and southwestern Asia (see magenta highlighted region in inset map).
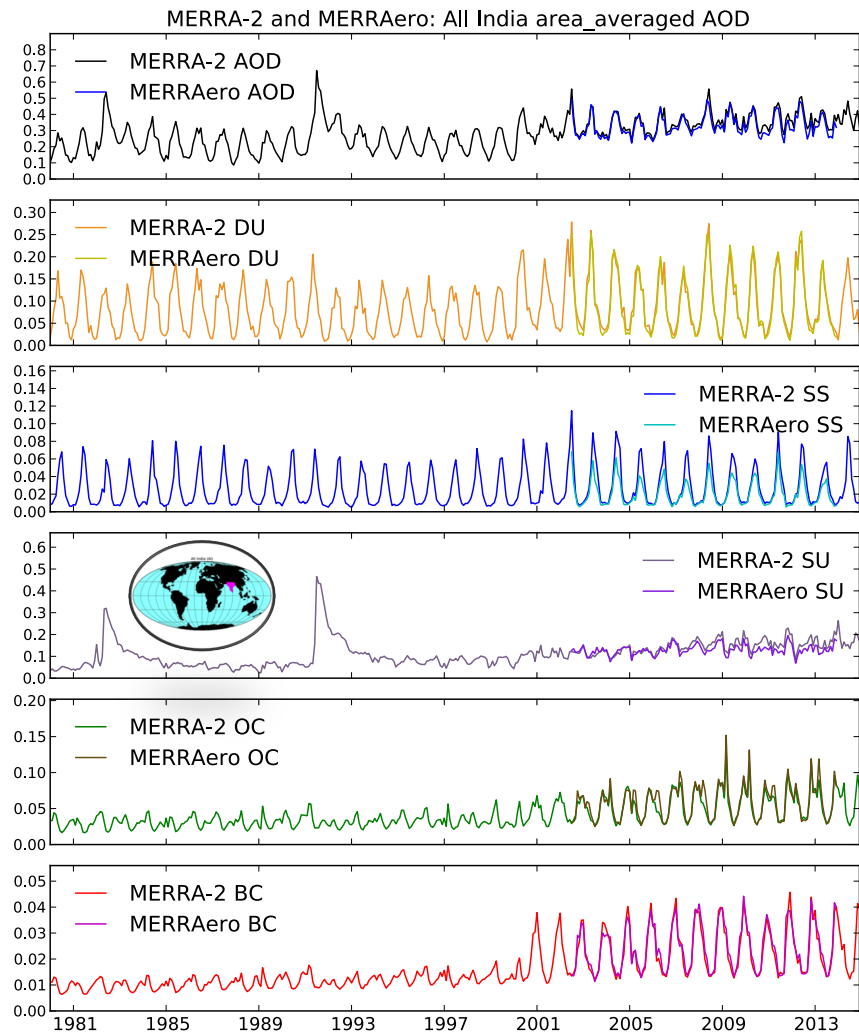
Figure B.14: Same as Fig. B.1 except over India (see magenta highlighted region in inset map).
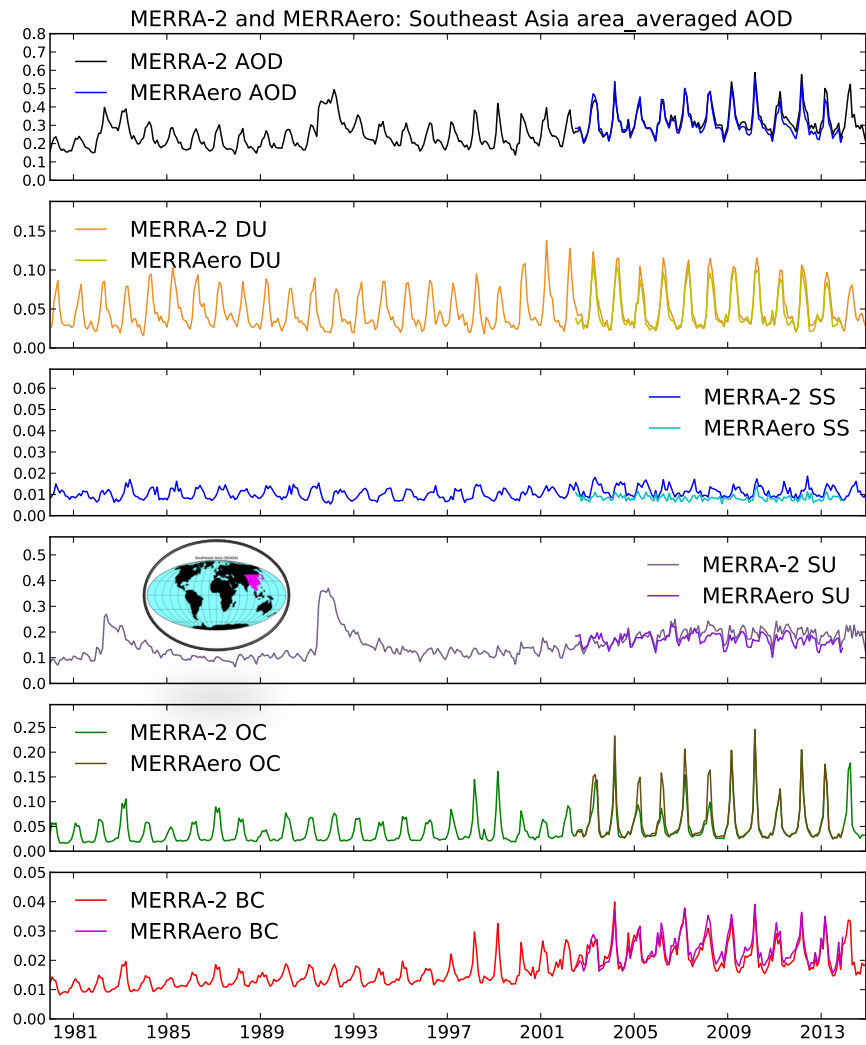
Figure B.15: Same as Fig. B.1 except over China and Southeast Asia (see magenta highlighted region in inset map).
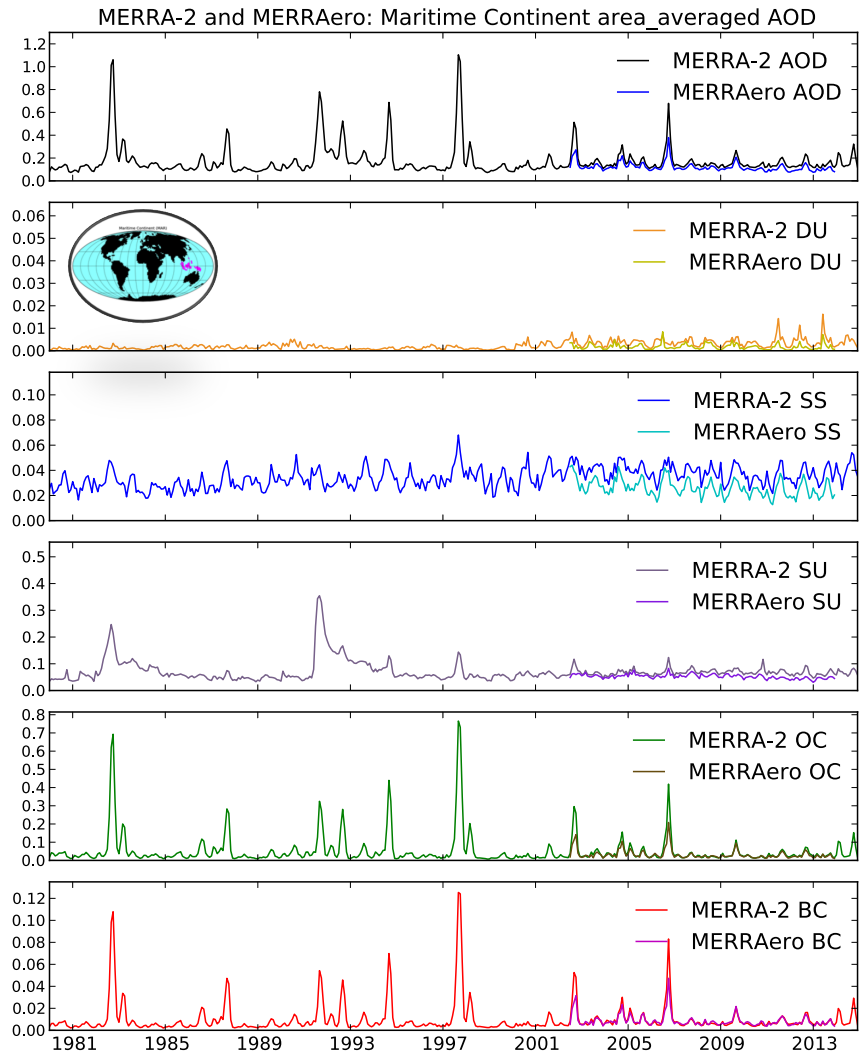
Figure B.16: Same as Fig. B.1 except over the Maritime Continent (see magenta highlighted region in inset map).
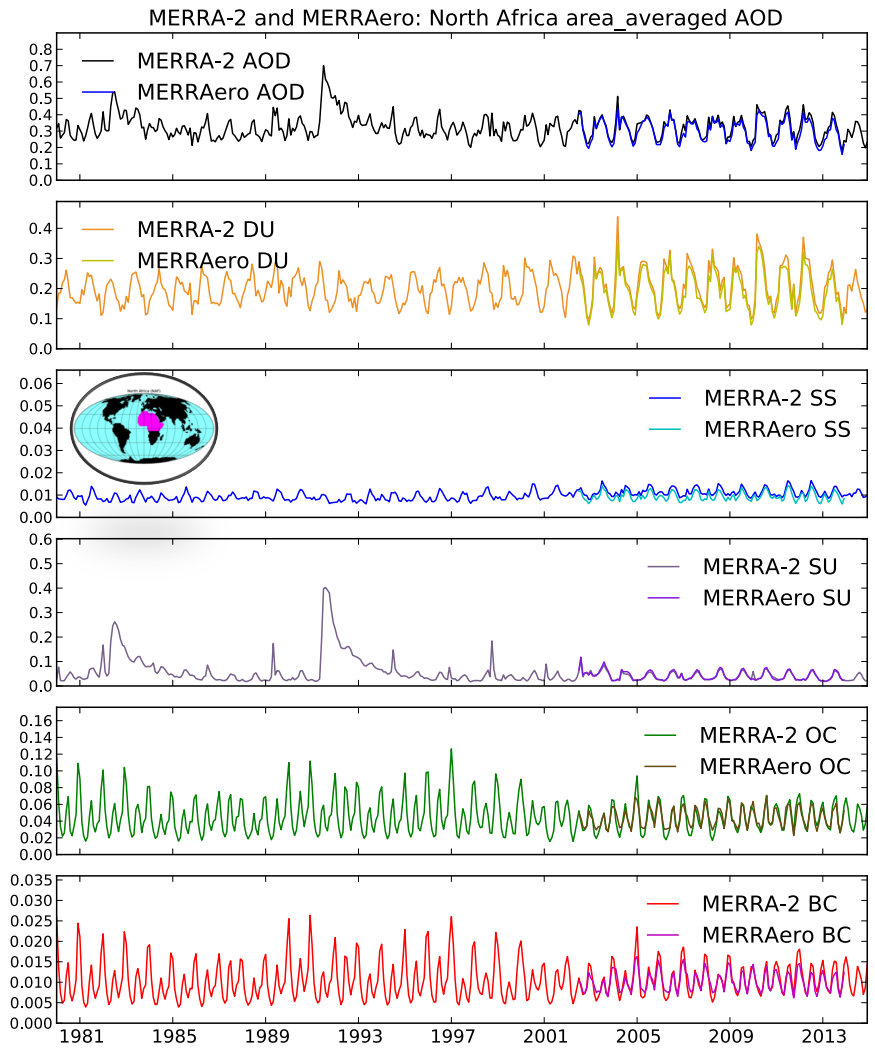
Figure B.17: Same as Fig. B.1 except over northern Africa (see magenta highlighted region in inset map).
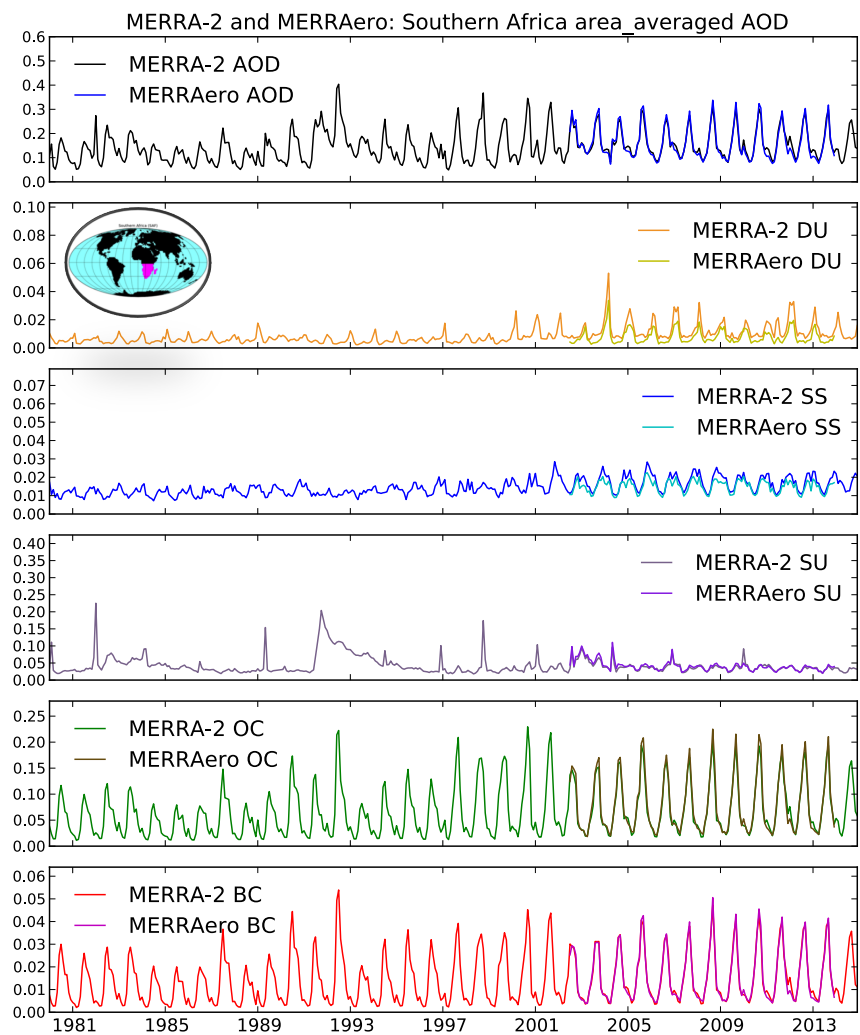
Figure B.18: Same as Fig. B.1 except over southern Africa (see magenta highlighted region in inset map).
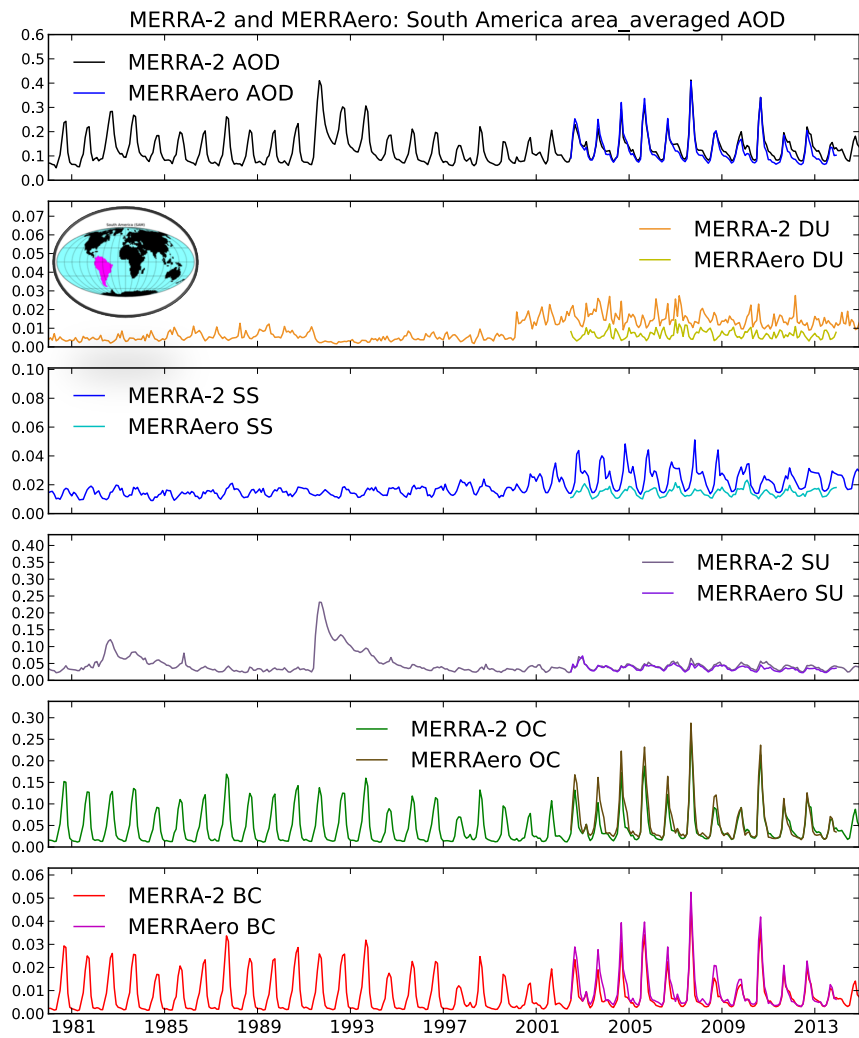
Figure B.19: Same as Fig. B.1 except over South America (see magenta highlighted region in inset map).
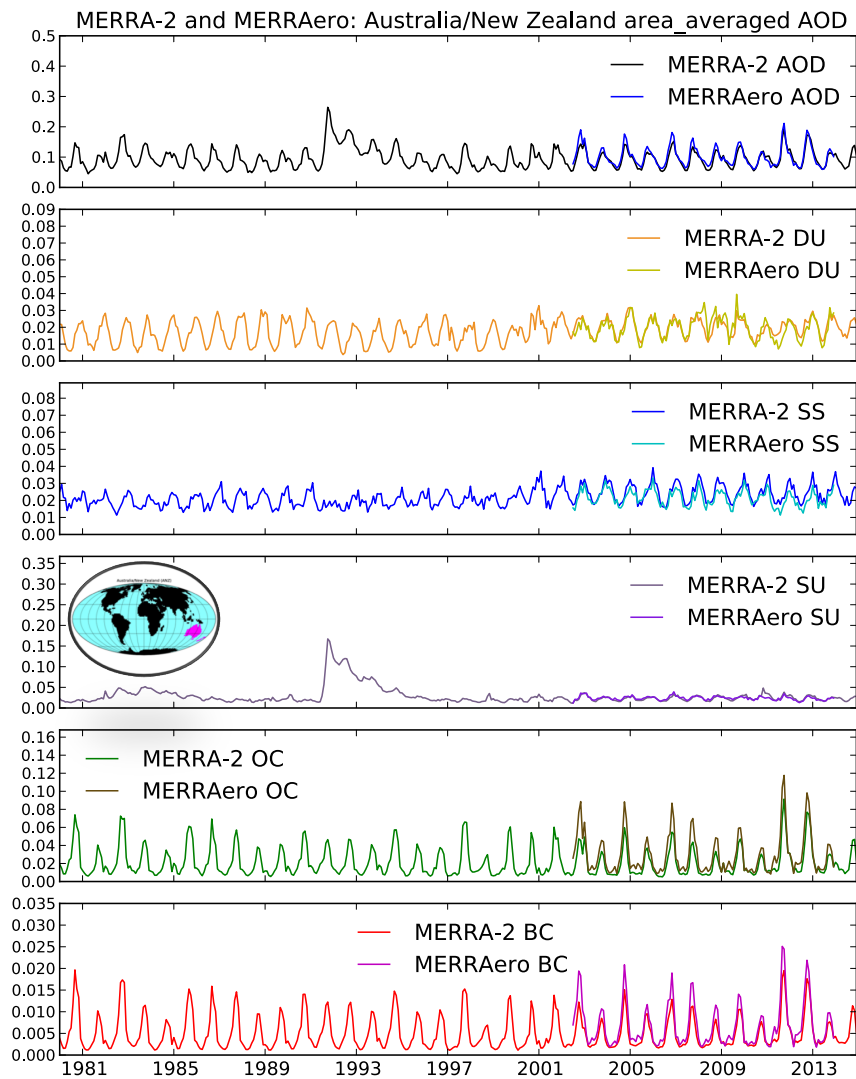
Figure B.20: Same as Fig. B.1 except over Australia and New Zealand (see magenta highlighted region in inset map).
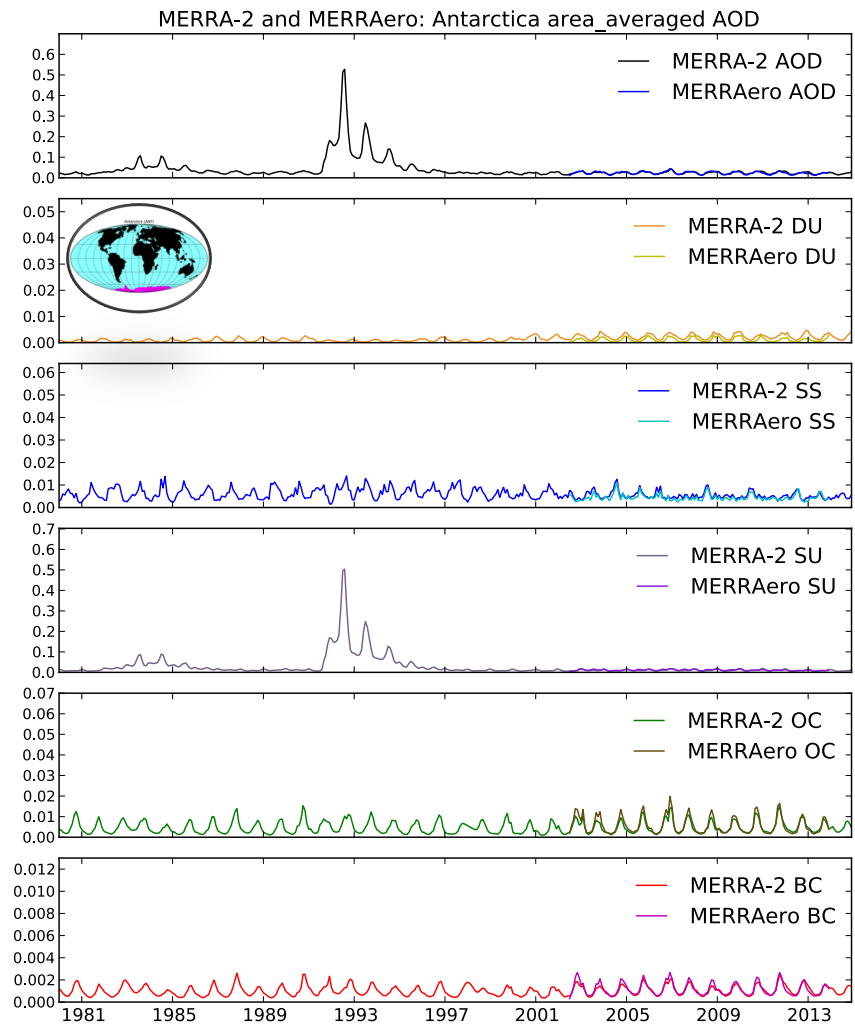
Figure B.21: Same as Fig. B.1 except over Antartica (see magenta highlighted region in inset map).
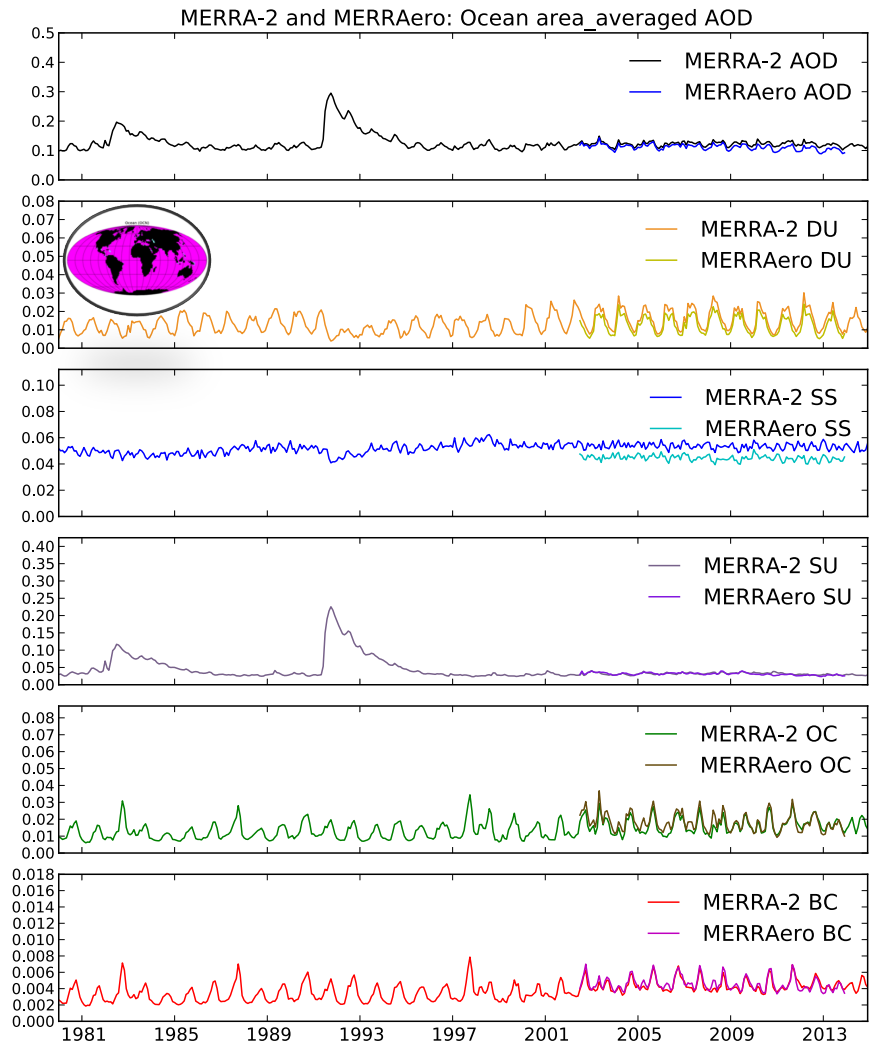
Figure B.22: Same as Fig. B.1 except over all ocean (see magenta highlighted region in inset map).
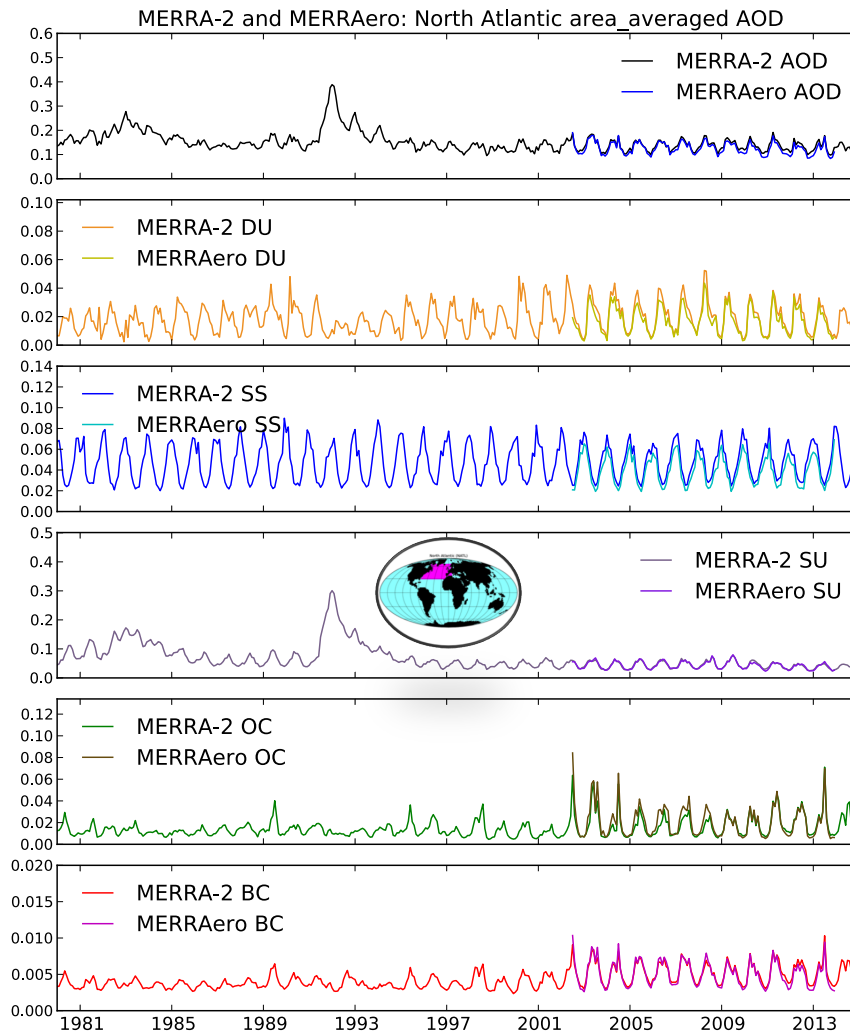
Figure B.23: Same as Fig. B.1 except over the northern Atlantic Ocean (see magenta highlighted region in inset map).
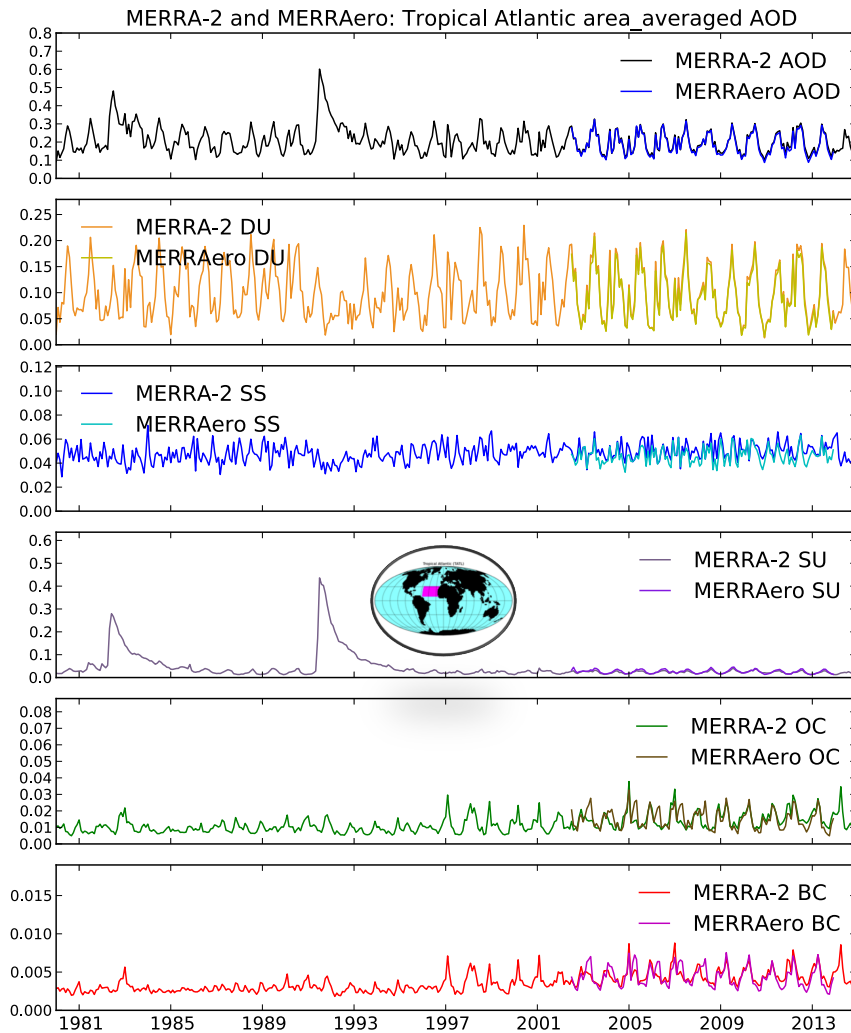
Figure B.24: Same as Fig. B.1 except over the tropical Atlantic Ocean (see magenta highlighted region in inset map).
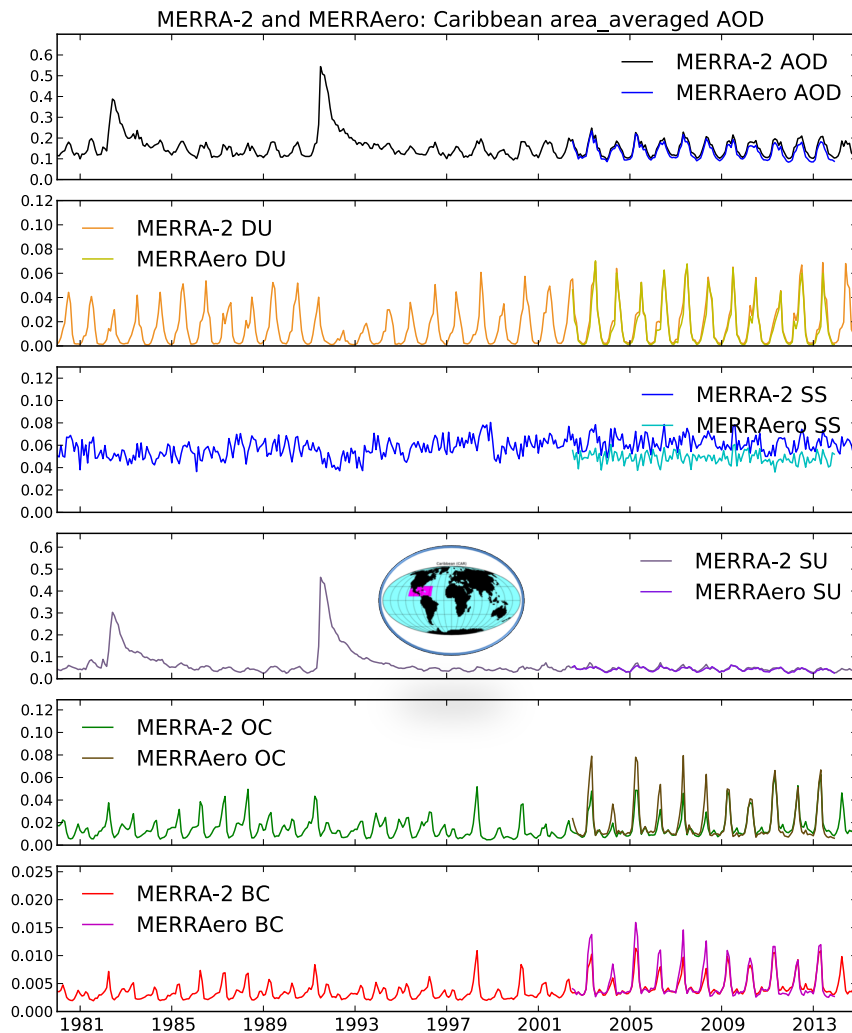
Figure B.25: Same as Fig. B.1 except over the Caribbean (see magenta highlighted region in inset map).
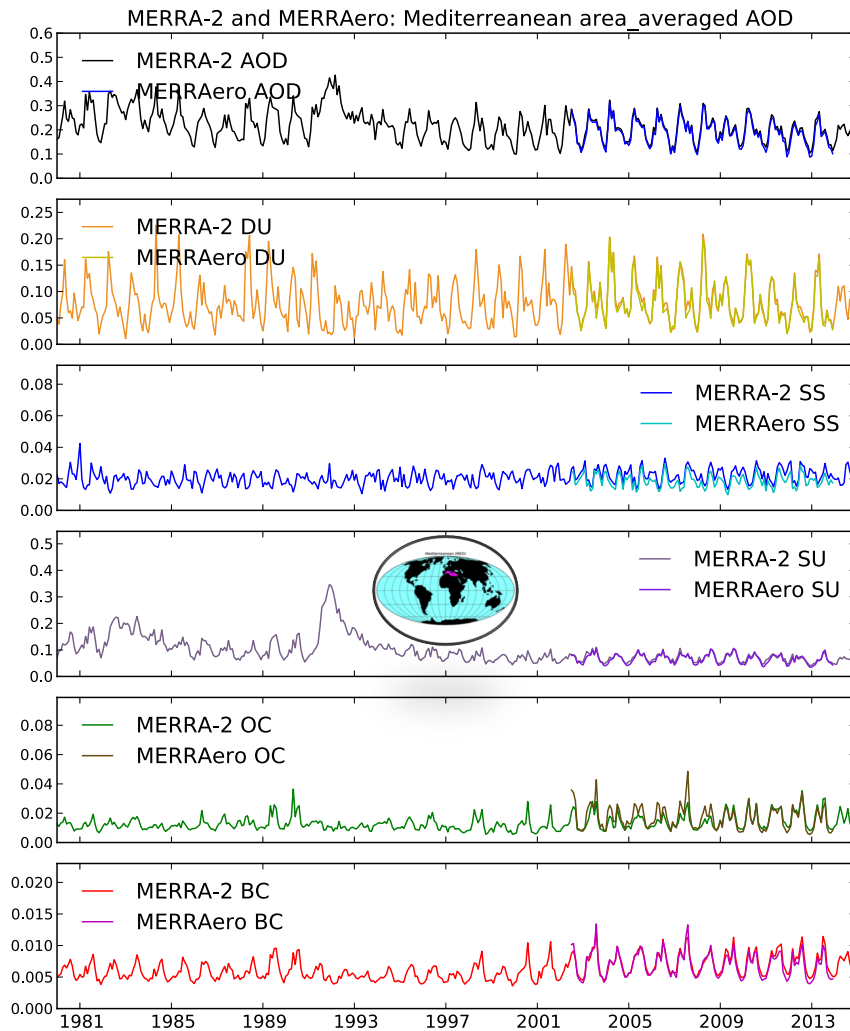
Figure B.26: Same as Fig. B.1 except over the Mediterranean (see magenta highlighted region in inset map).
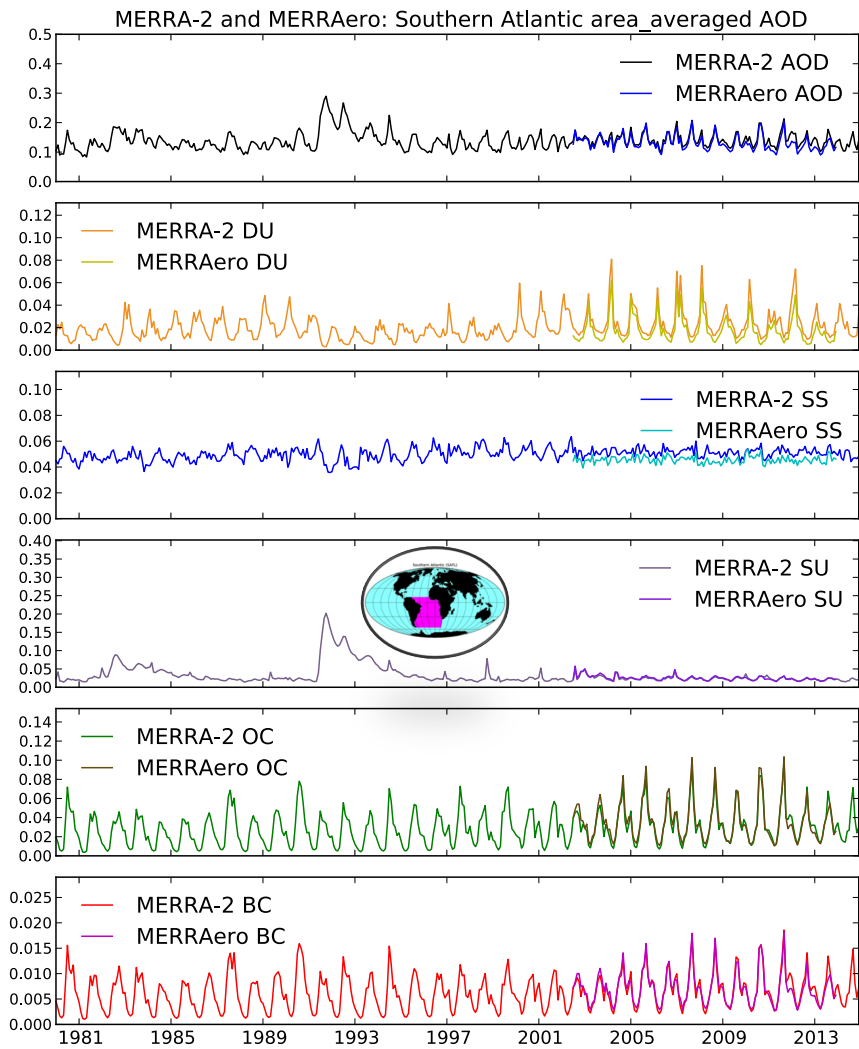
Figure B.27: Same as Fig. B.1 except over the southern Atlantic Ocean (see magenta highlighted region in inset map).
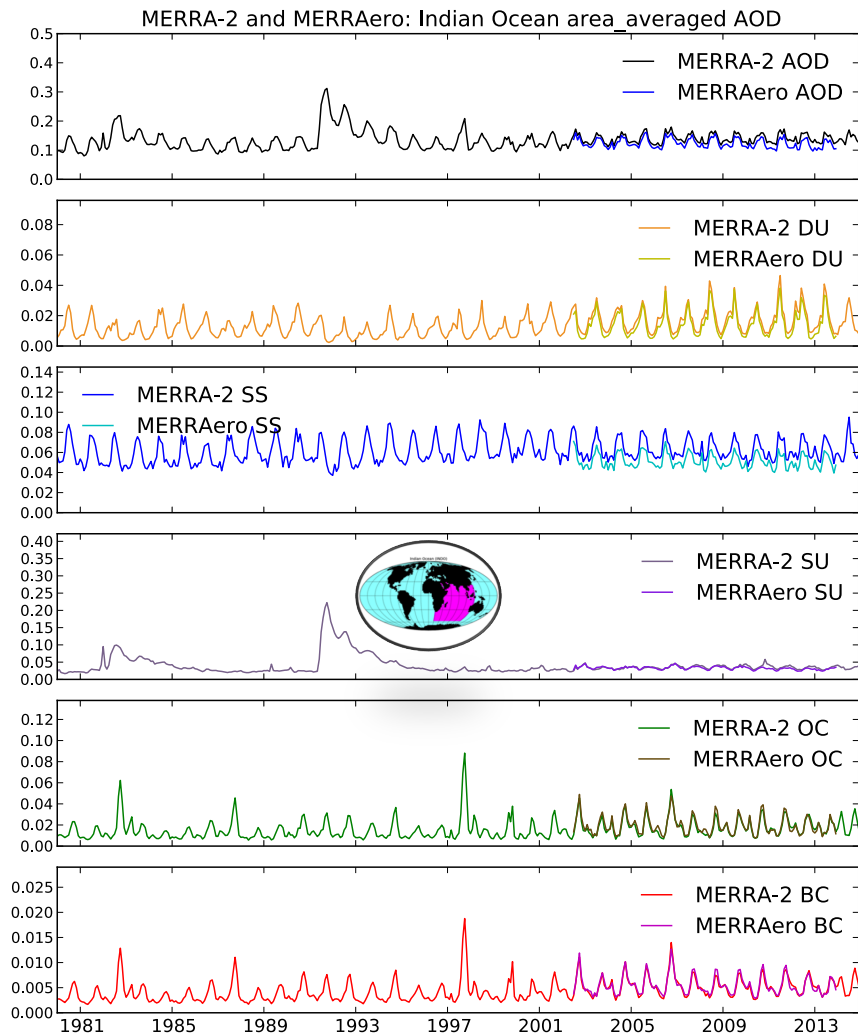
Figure B.28: Same as Fig. B.1 except over the Indian Ocean (see magenta highlighted region in inset map).
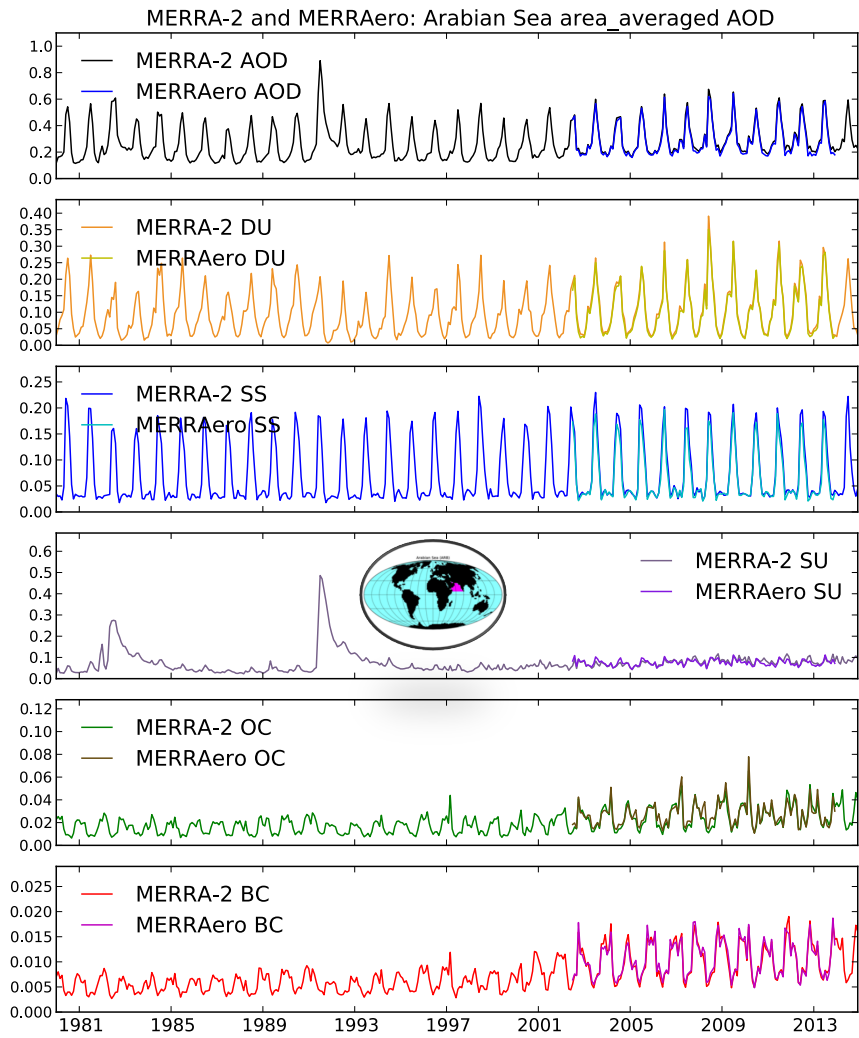
Figure B.29: Same as Fig. B.1 except over the Arabian Sea (see magenta highlighted region in inset map).
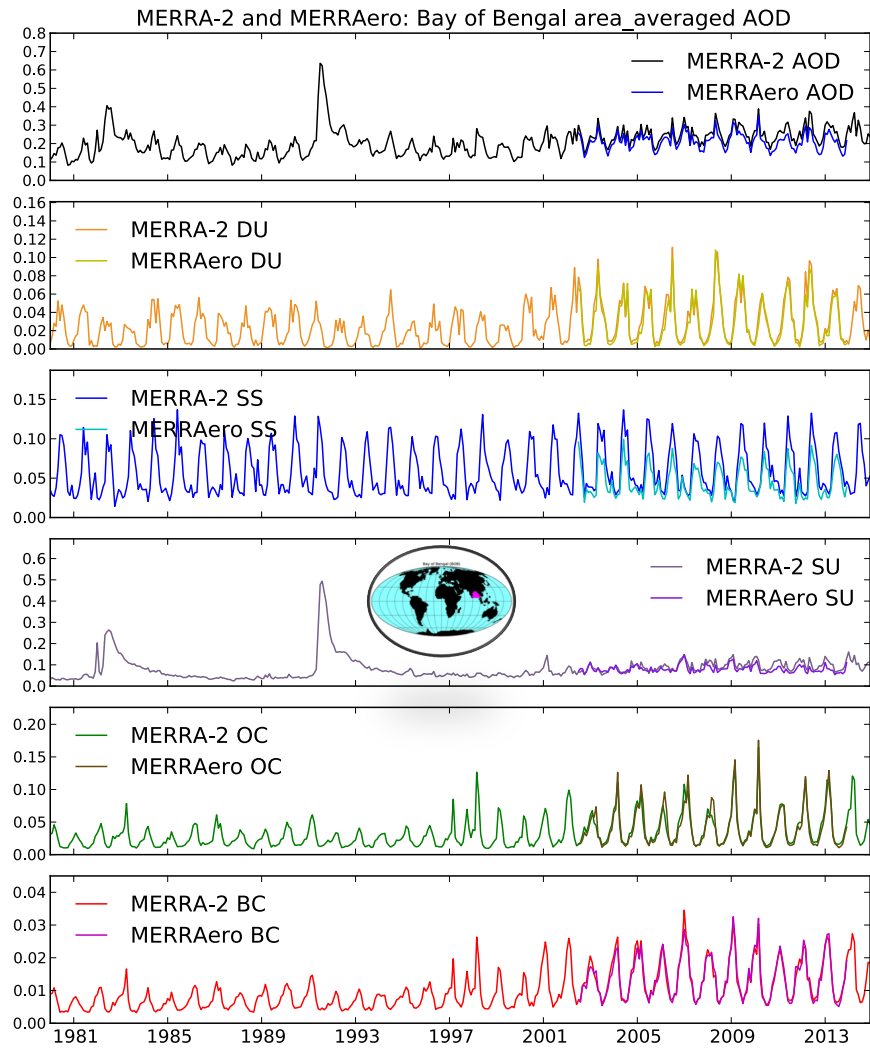
Figure B.30: Same as Fig. B.1 except over the Bay of Bengal (see magenta highlighted region in inset map).
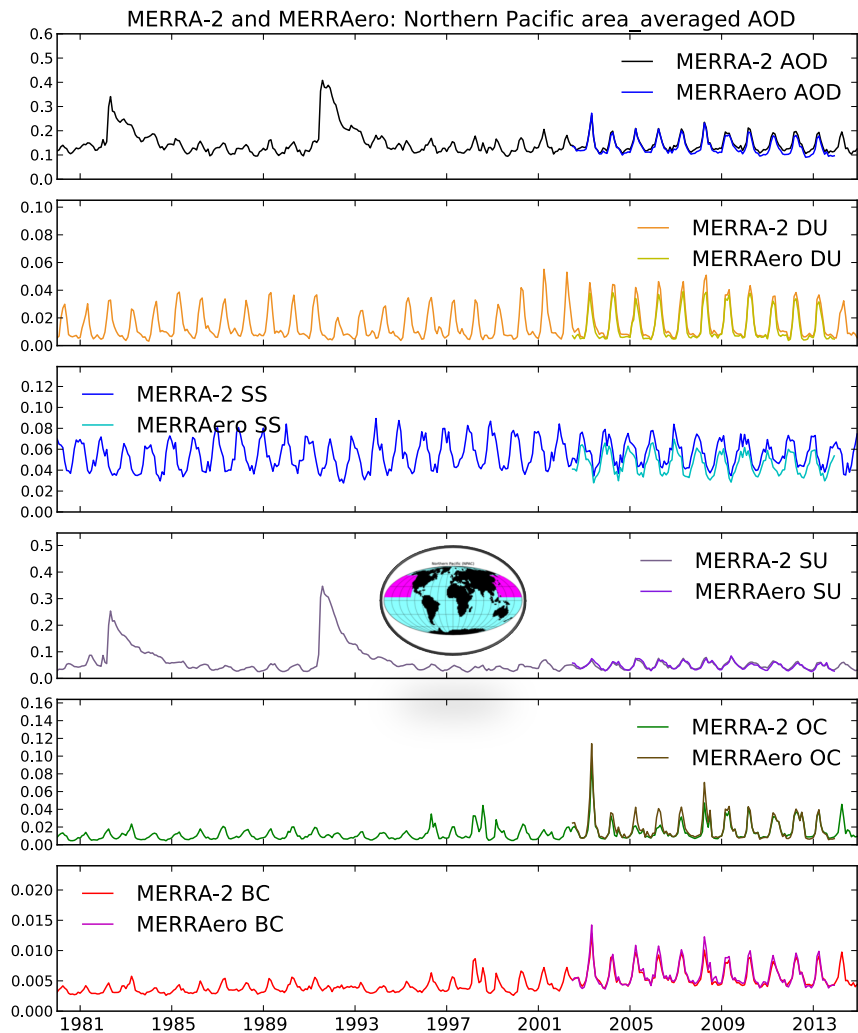
Figure B.31: Same as Fig. B.1 except over the northern Pacific Ocean (see magenta highlighted region in inset map).
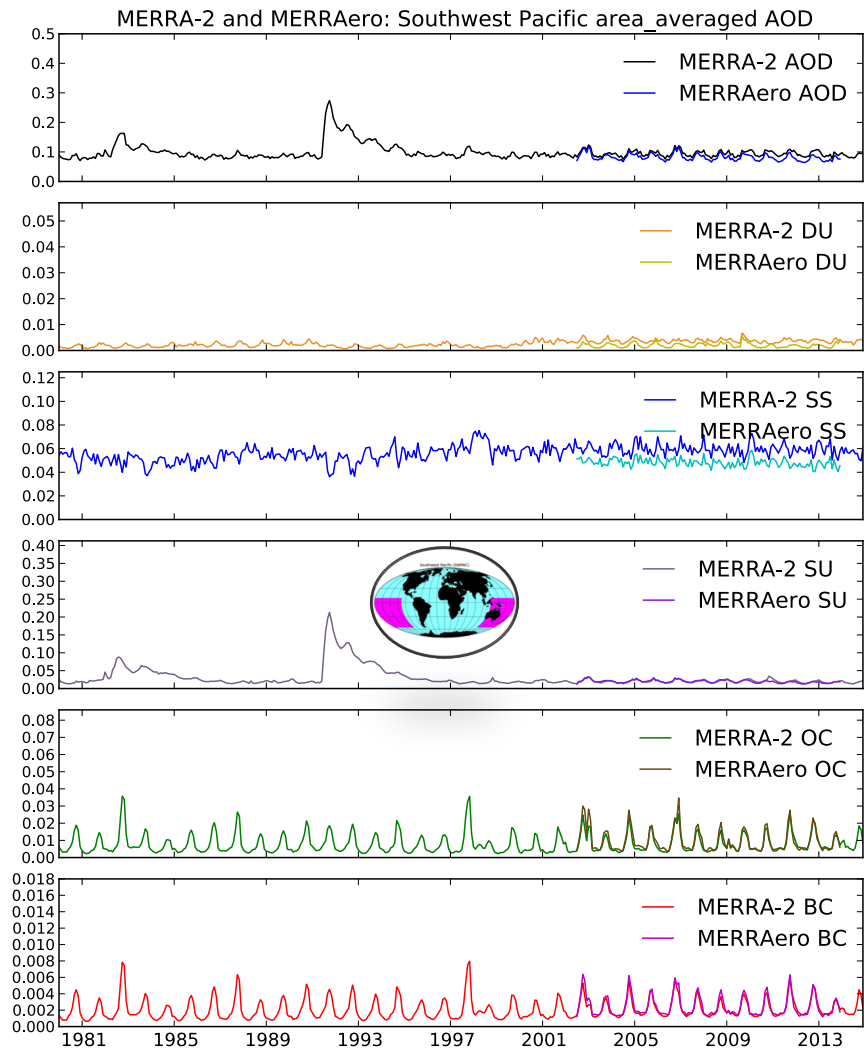
Figure B.32: Same as Fig. B.1 except over the southwestern Pacific Ocean (see magenta highlighted region in inset map).
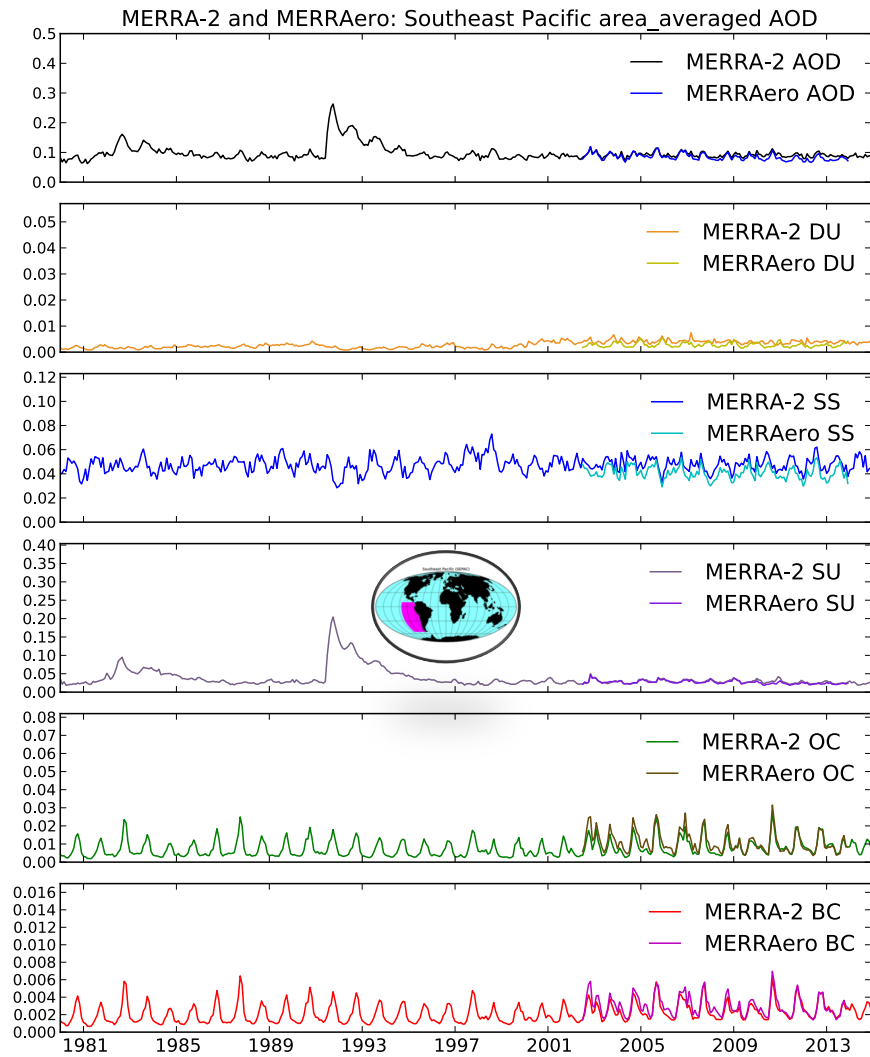
Figure B.33: Same as Fig. B.1 except over the southeastern Pacific Ocean (see magenta highlighted region in inset map).
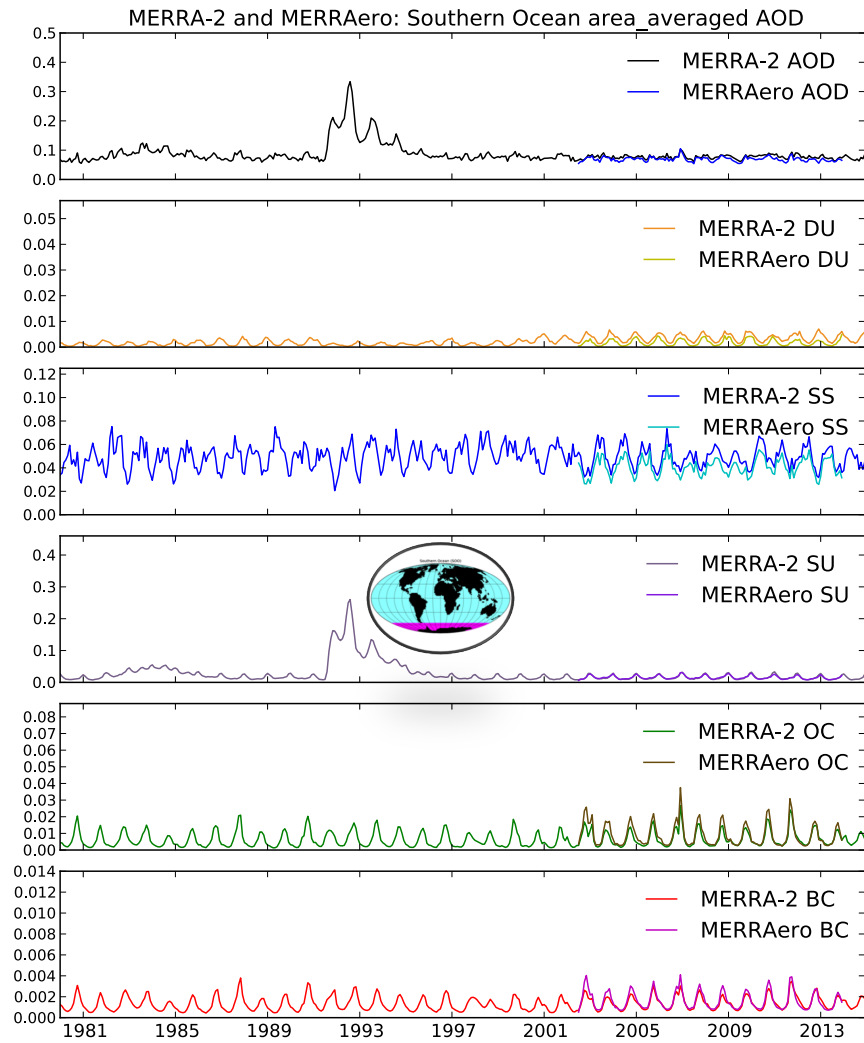
Figure B.34: Same as Fig. B.1 except over the Southern Ocean (see magenta highlighted region in inset map).

Appendix C

Seasonal Means
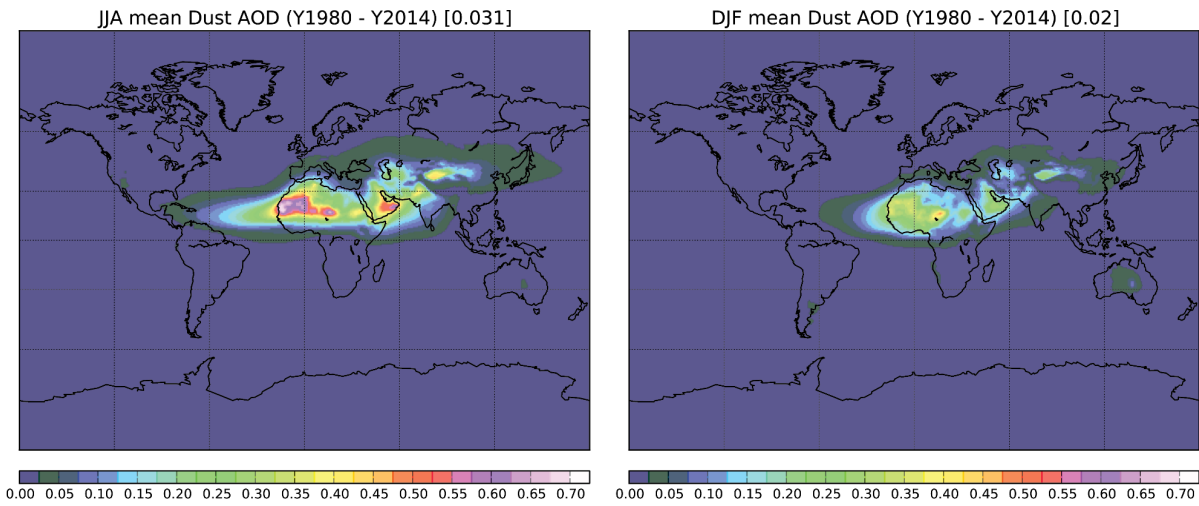
Figure C.1: AOD in boreal summer (left column) and winter (right column) for dust averaged over the period Y1980-Y2014.
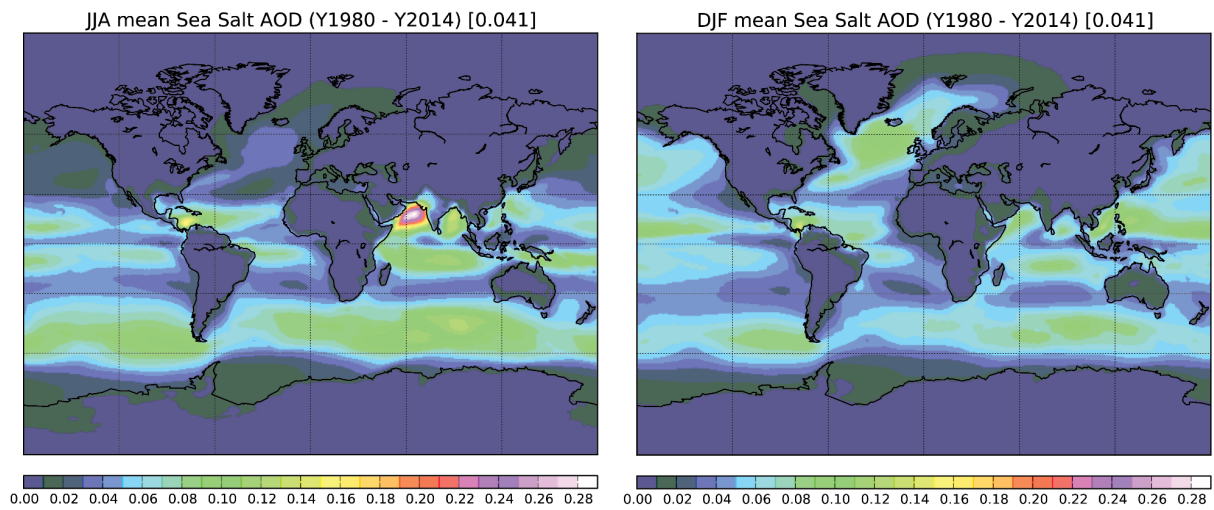
Figure C.2: AOD in boreal summer (left column) and winter (right column) for sea salt averaged over the period Y1980-Y2014.
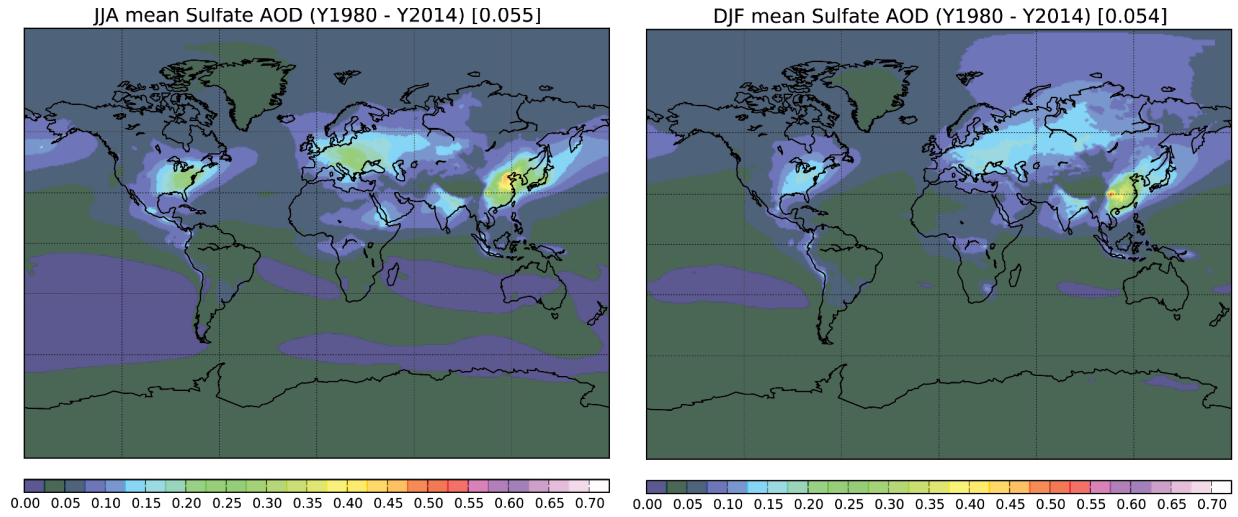
Figure C.3: AOD in boreal summer (left column) and winter (right column) for sulfate averaged over the period Y1980-Y2014.
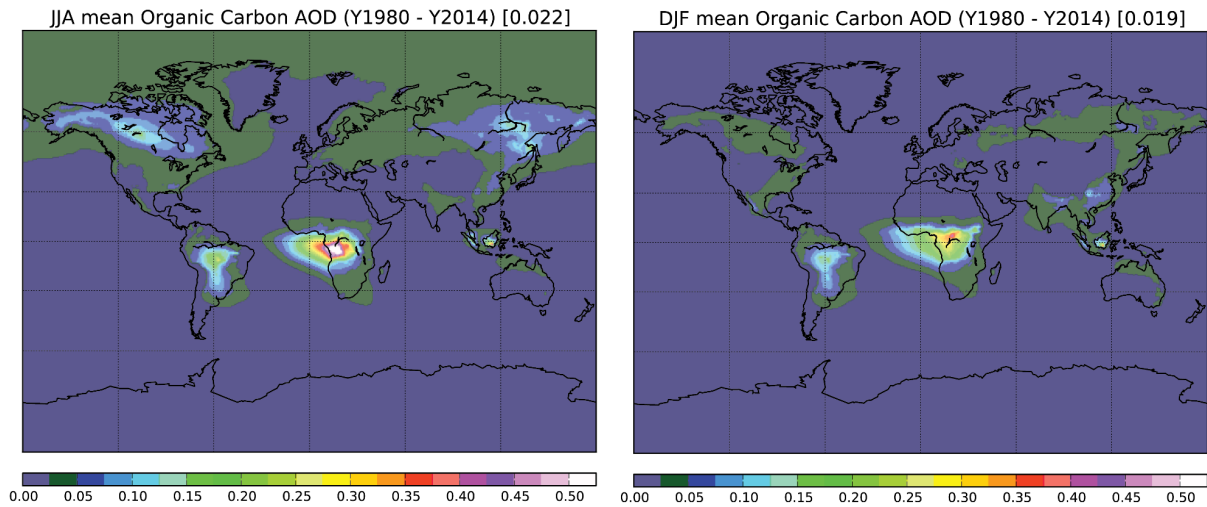
Figure C.4: AOD in boreal summer (left column) and winter (right column) for organic carbon averaged over the period Y1980-Y2014.
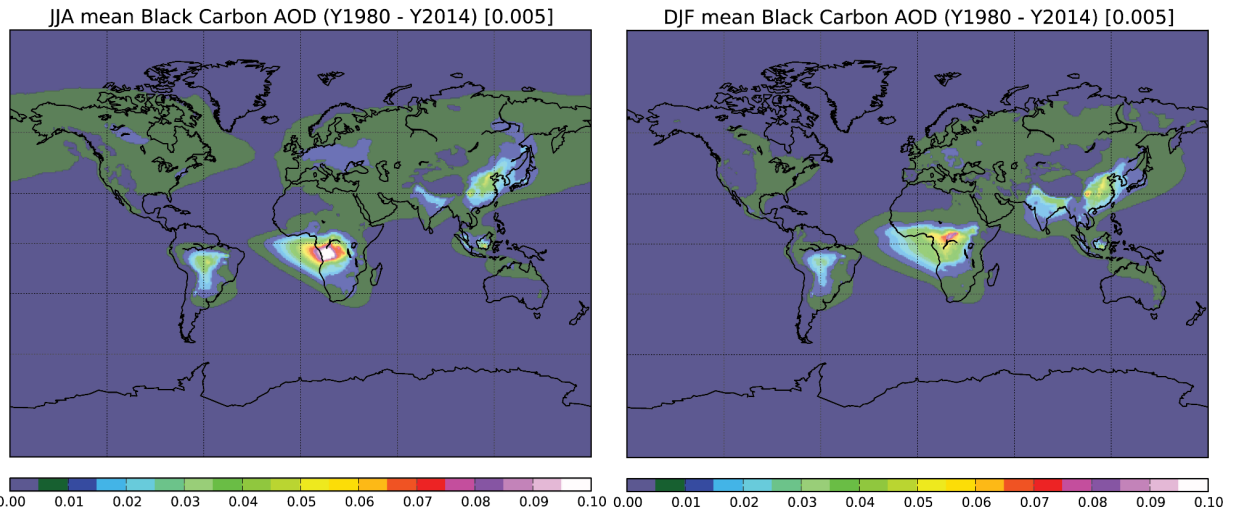
Figure C.5: AOD in boreal summer (left column) and winter (right column) for black carbon averaged over the period Y1980-Y2014.
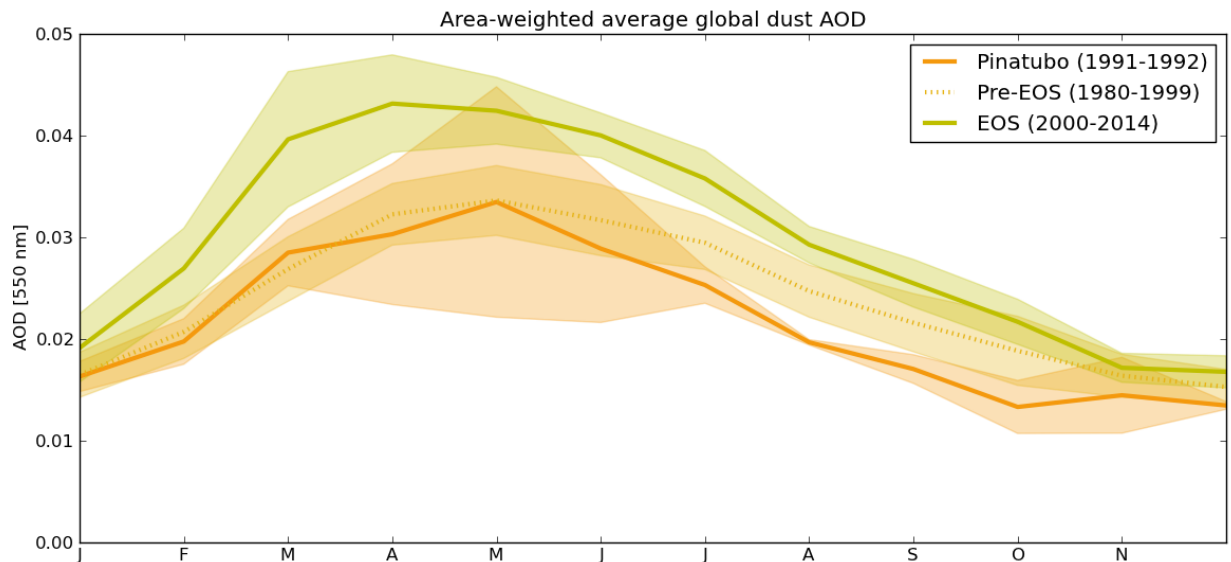
Figure C.6: Monthly mean area-weighted average dust AOD for the pre-EOS (1980-1999), EOS (2000-2014), and Pinatubo (1991-1992) time periods.
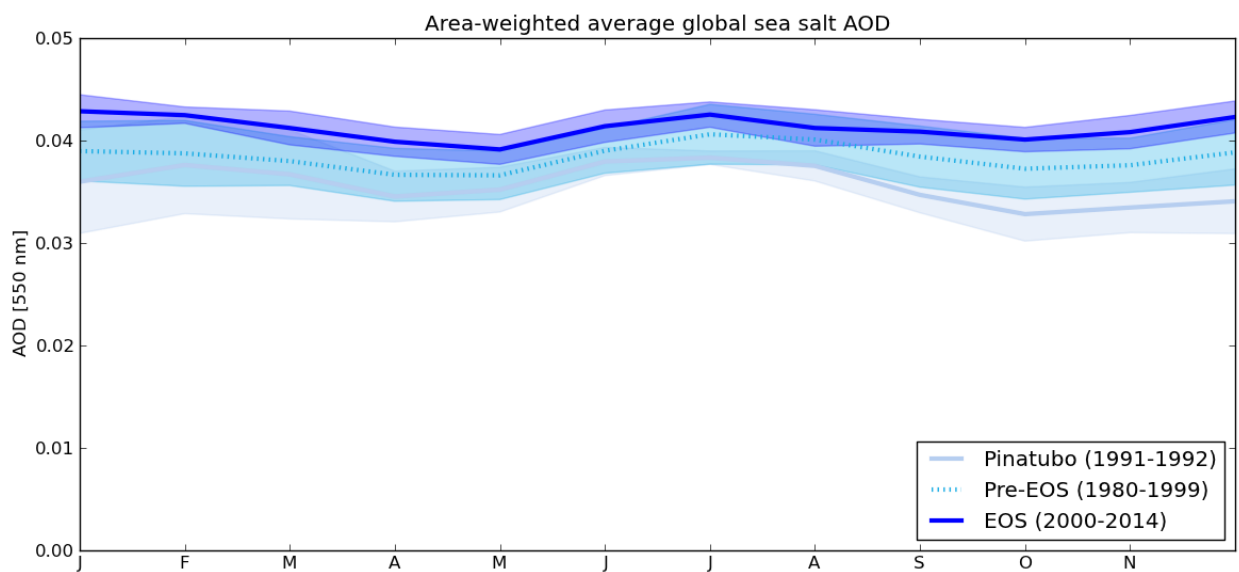
Figure C.7: Monthly mean area-weighted average sea salt AOD for the pre-EOS (1980-1999), EOS (2000-2014), and Pinatubo (1991-1992) time periods.
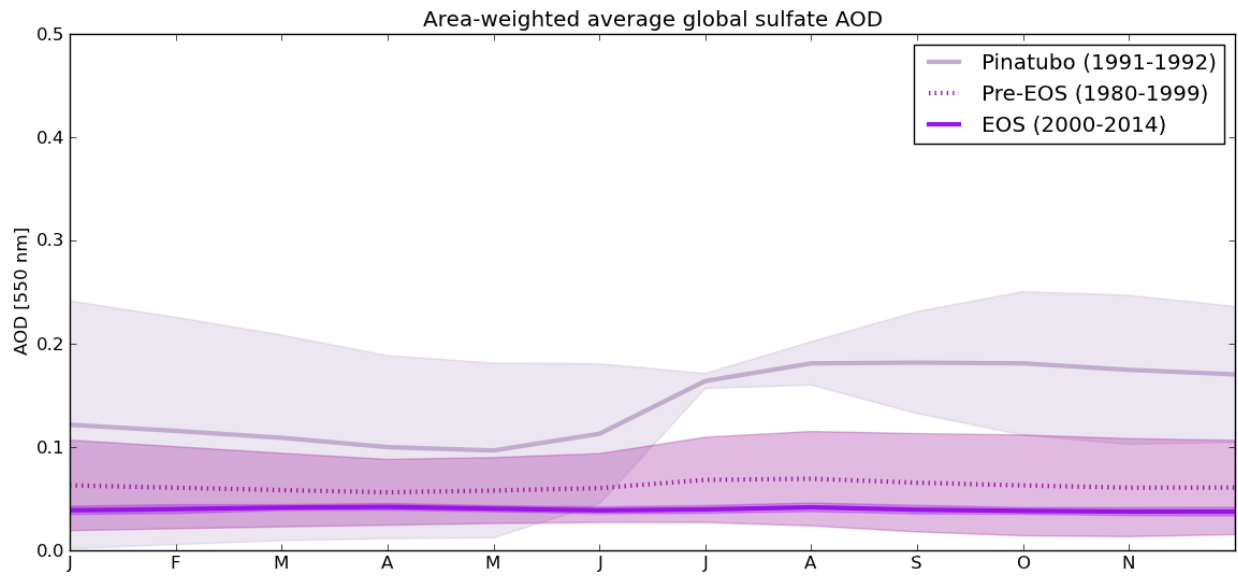
Figure C.8: Monthly mean area-weighted average sulfate AOD for the pre-EOS (1980-1999), EOS (2000-2014), and Pinatubo (1991-1992) time periods.
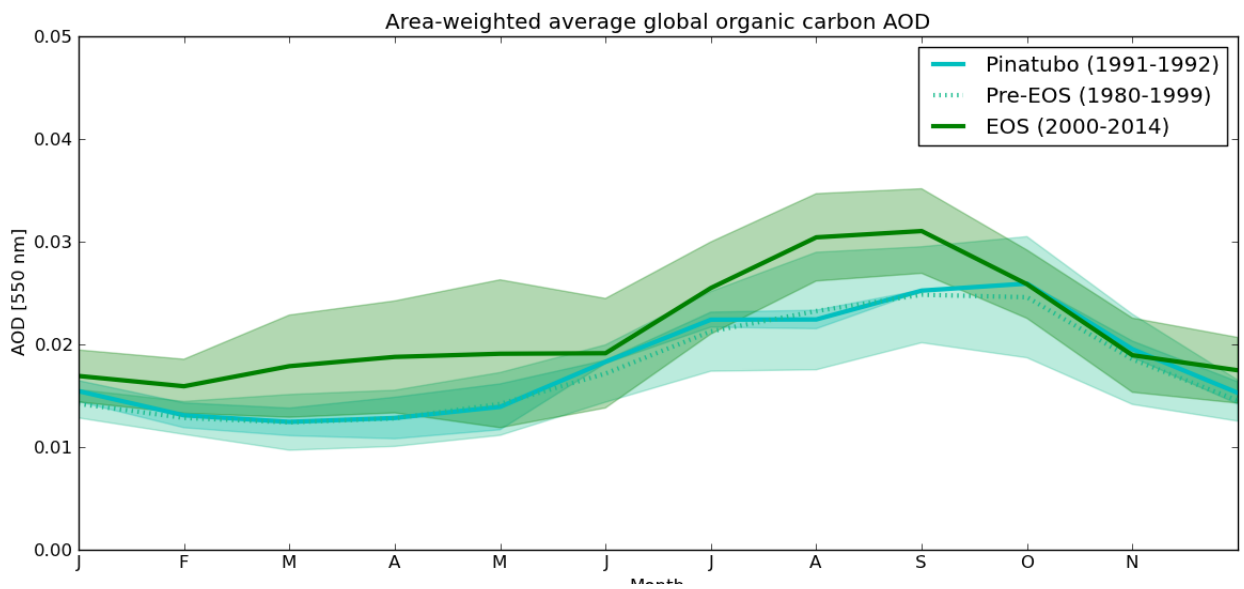
Figure C.9: Monthly mean area-weighted average organic carbon AOD for the pre-EOS (1980-1999), EOS (2000-2014), and Pinatubo (1991-1992) time periods.
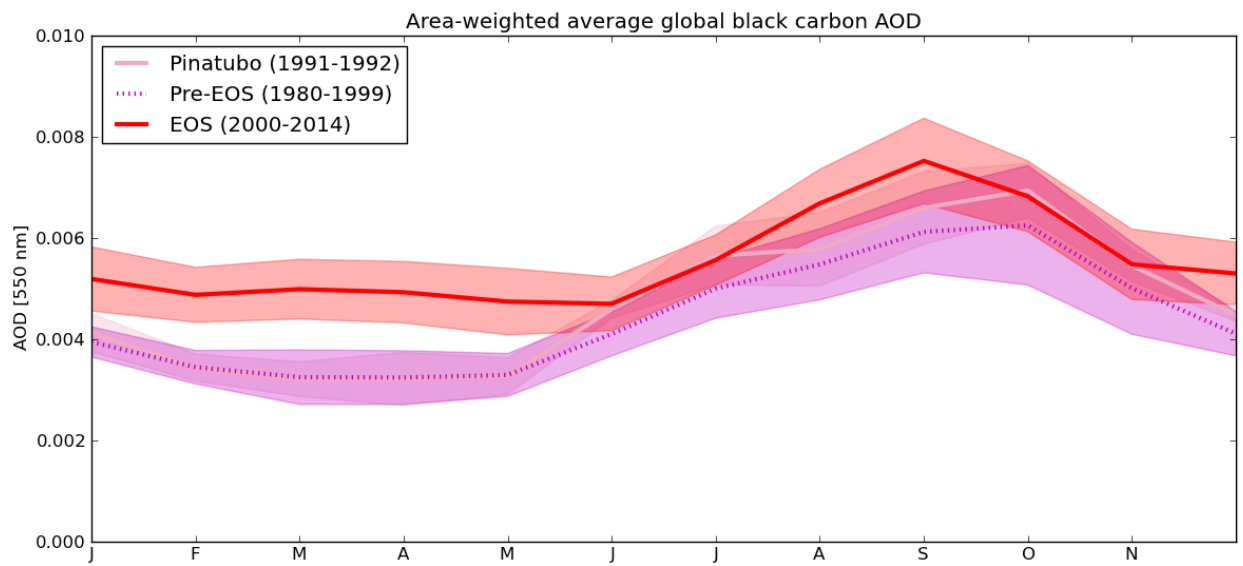
Figure C.10: Monthly mean area-weighted average black carbon AOD for the pre-EOS (1980-1999), EOS (2000-2014), and Pinatubo (1991-1992) time periods.

Previous Volumes in This Series

137

Achuthavarier, Michael Bosilovich, Virginie Buchard, Winston Chao, Lawrence Coy, Richard Cullather, Arlindo da Silva, Anton Darmenov, Ronald M. Errico, Marangelly Fuentes, Min-Jeong Kim, Randal Koster, Will McCarty, Jyothi Nattala, Gary Partyka, Siegfried Schubert, Guillaume Vernieres, Yuri Vikhliaev, and Krzysztof Wargan

Volume 37 *March 2015*	Maintaining Atmospheric Mass and Water Balance within Reanalysis **Lawrence L. Takacs, Max Suarez, and Ricardo Todling**
Volume 38 *September 2015*	The Quick Fire Emissions Dataset (QFED) – Documentation of versions 2.1, 2.2 and 2.4 **Anton S. Darmenov and Arlindo da Silva**
Volume 39 *September 2015*	Land Boundary Conditions for the Goddard Earth Observing System Model Version 5 (GEOS-5) Climate Modeling System - Recent Updates and Data File Descriptions **Sarith Mahanama, Randal Koster, Gregory Walker, Lawrence Takacs**, **Rolf Reichle, Gabrielle De Lannoy, Qing Liu, Bin Zhao, and** Max **Suarez**
Volume 40 *October 2015*	Soil Moisture Active Passive (SMAP) Project Assessment Report for the Beta-Release L4_SM Data Product **Rolf H. Reichle, Gabrielle J. M. De Lannoy, Qing Liu, Andreas Colliander**, **Austin Conaty, Thomas Jackson, John Kimball, and Randal D. Koster**
Volume 41 *October 2015*	GDIS Workshop Report **Siegfried Schubert, Will Pozzi, Kingtse Mo, Eric Wood, Kerstin Stahl, Mike Hayes, Juergen Vogt, Sonia Seneviratne, Ron Stewart, Roger Pulwarty, and Robert Stefanski**
Volume 42 *November 2015*	Soil Moisture Active Passive (SMAP) Project Calibration and Validation for the L4_C Beta-Release Data Product **John Kimball, Lucas Jones, Joseph Glassy, E. Natasha Stavros, Nima Madani, Rolf Reichle, Thomas Jackson, and Andreas Colliander**